Physik - Department

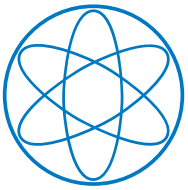

Background Suppression in TeO_2 Bolometers with Neganov-Luke Amplified Cryogenic Light Detectors

Dissertation
von

Michael Willers

Technische Universität
München

Technische Universität München
Physik-Department
Lehrstuhl für Experimentalphysik und Astroteilchenphysik

Background Suppression in TeO_2 Bolometers with Neganov-Luke Amplified Cryogenic Light Detectors

Michael Willers

Vollständiger Abdruck der von der Fakultät für Physik der Technischen Universität München zur Erlangung des akademischen Grades eines

Doktors der Naturwissenschaften (Dr. rer. nat.)

genehmigten Dissertation.

Vorsitzender:	Univ.-Prof. Dr. Alejandro Ibarra
Prüfer der Dissertation:	
	1. Univ.-Prof. Dr. Lothar Oberauer
	2. Univ.-Prof. Dr. Peter Fierlinger

Die Dissertation wurde am 08.12.2014 bei der Technischen Universität München eingereicht und durch die Fakultät für Physik am 26.01.2015 angenommen.

Abstract

The existence of the neutrinoless double beta decay ($0\nu\beta\beta$) is predicted by various extensions of the Standard Model of particle physics and an observation would unambiguously establish the Majorana character of neutrinos and the existence of a lepton number violating process. Experimental searches for the $0\nu\beta\beta$ decay are considered as one of the most important fields of research in neutrino and astroparticle physics. An important aspect for the next generation of experiments searching for the $0\nu\beta\beta$ decay is the development of active background suppression techniques which provide a highly efficient suppression of background-induced events from signal events.

Experiments employing cryogenic bolometers consisting of TeO_2 crystals are, due to their excellent energy resolution and the high natural abundance of ^{130}Te of $\sim 35\,\%$, among the most promising experimental approaches in the search for the $0\nu\beta\beta$ decay. A novel background suppression technique for these detectors is based on the detection of Cherenkov radiation emitted by high-energetic electrons within the crystals and allows a discrimination between α-induced background events and signal-like e^-/γ events. Due to the low amount of light ($\mathcal{O}(0-400\,\mathrm{eV})$) produced by electrons with energies close to the $Q_{\beta\beta}$ value of ^{130}Te at $\sim 2.5\,\mathrm{MeV}$, very sensitive cryogenic light detectors are required.

In this work the application of Neganov-Luke amplified cryogenic light detectors for the background suppression in TeO_2 crystals is investigated for the first time and highly promising results have been achieved. Using the Neganov-Luke effect, the heat signal induced by particle interactions in a semiconductor absorber is amplified by drifting the generated charge carriers in an applied electric field. Furthermore, the signal-to-noise ratio of the detector is increased, leading to an improvement of the sensitivity of the cryogenic light detector.

To determine the suppression efficiency between α- and e^-/γ-induced events, measurements with a cryogenic detector module consisting of a $\sim 24\,\mathrm{g}$ TeO_2 crystal ($20 \times 20 \times 10\,\mathrm{mm^3}$ in size) and a Neganov-Luke amplified light detector (a $20 \times 20 \times 0.5\,\mathrm{mm^3}$ silicon absorber equipped with four aluminum electrode strips deposited onto the side of the absorber facing the crystal) have been performed. For the measurements in the present work, a Neganov-Luke voltage of $V_{NL} = 70\,\mathrm{V}$ has been applied between the electrodes of the

Neganov-Luke light detector and a signal amplification by a factor of ~ 10.8 and an improvement in the signal-to-noise ratio by a factor of ~ 6.2 have been achieved. The 1σ energy threshold of the light detector when operated with applied Neganov-Luke voltage was determined to be $\sim 7.8\,\mathrm{eV}$. To determine the suppression efficiency of α-induced events at energies close to the $Q_{\beta\beta}$ value of ^{130}Te, the TeO_2 crystal was irradiated with α particles from a ^{147}Sm source and γ rays from a ^{228}Th source.

Due to the application of Neganov-Luke amplified cryogenic light detectors, a highly efficient discrimination between α- and e^-/γ-induced events in TeO_2 could be reached for the first time. During a $\sim 42\,\mathrm{h}$ measurement, a suppression efficiency of $\gtrsim 99\%$ for α-induced events has been achieved while maintaining a signal acceptance of 99.8% for e^-/γ-induced events. These results show that the level of α-induced background events in $0\nu\beta\beta$-decay experiments using cryogenic detectors based on TeO_2 crystals could be reduced by ~ 2 orders of magnitude with practically no reduction in the signal acceptance.

First simulations studying the production of Cherenkov radiation in TeO_2 crystals by $0\nu\beta\beta$- and γ-induced events as well as a simulation designed to investigate the light collection efficiency in a cryogenic detector module with TeO_2 crystals have been performed. It was found that the amount of Cherenkov radiation produced by γ-induced events with an deposited energy of $\sim 2.6\,\mathrm{MeV}$ is practically identical to the amount of Cherenkov radiation produced for ^{130}Te $0\nu\beta\beta$-decay events, thereby motivating the choice of using a ^{228}Th source to determine the suppression efficiency in TeO_2 crystals. The results furthermore indicate that the amount of detectable Cherenkov radiation could be significantly increased by using a light reflector with a higher reflectivity in the UV spectrum.

The results obtained for the first time in the present work are an important milestone for the application of Neganov-Luke amplified light detectors for the background suppression in future $0\nu\beta\beta$-decay experiments based on cryogenic TeO_2 bolometers.

Zusammenfassung

Der neutrinolose Doppelbetazerfall wird von vielen Erweiterungen des Standard-Models der Teilchenphysik vorhergesagt und eine Beobachtung dieses Zerfalls würde zweifelsfrei den Majorana-Charakter der Neutrinos, sowie die Existenz eines Prozesses bestätigen, der die Leptonenzahl verletzt. Experimente zur Suche nach dem neutrinolosen Doppelbetazerfall zählen gegenwärtig zu einem der bedeutendsten Forschungsfelder in der Neutrino- und Astroteilchenphysik. Ein wichtiger Aspekt für die nächste Generation von Experimenten zur Suche nach dem $0\nu\beta\beta$-Zerfall ist die Entwicklung von hocheffizienten Techniken zur aktiven Untergrundunterdrückung.

Experimente, die Tieftemperatur-Detektoren aus TeO_2-Kristallen einsetzen, zählen aufgrund ihrer sehr guten Energieauflösung und der hohen natürlichen Isotopen-Häufigkeit von ^{130}Te zu den vielversprechendsten Ansätzen für die Suche nach dem $0\nu\beta\beta$-Zerfall. Eine neuartige Technik zur Unterdrückung von Untergrundereignissen in diesen Detektoren basiert auf der Detektion der durch hochenergetische Elektronen emittierten Cherenkov-Strahlung und erlaubt somit eine Unterscheidung zwischen α-induzierten Untergrundereignissen und signalartigen e^-/γ Ereignissen. Aufgrund der geringen Menge Lichts, die von Elektronen mit einer Energie nahe am $Q_{\beta\beta}$-Wert von ^{130}Te bei $\sim 2.5\,\mathrm{MeV}$ produziert wird, werden sehr sensitive Tieftemperatur-Lichtdetektoren benötigt.

Im Rahmen dieser Arbeit wurde erstmalig die Anwendung von Neganov-Luke-verstärkten Tieftemperatur-Lichtdetektoren zur Untergrundunterdrückung in TeO_2-Kristallen untersucht und es konnten vielversprechende Ergebnisse erzielt werden. Über Neganov-Luke Effekt kann das durch Teilchenwechselwirkungen in einem Halbleiterabsorber erzeugte Wärmesignal verstärkt werden. Diese Verstärkung wird durch das Driften der durch die Teilchenwechselwirkung erzeugten Ladungsträger in einem elektrischen Feld erreicht. Zustätzlich zur Signalverstärkung wird das Signal-zu-Rausch-Verhältnis erhöht, was zu einer Verbesserung der Nachweisschwelle des Lichtdetektors führt.

Um die Unterdrückungseffizienz zwischen α- und e^-/γ-induzierten Ereignissen zu untersuchen, wurden Messungen mit einem Tieftemperatur-Detektormodul, bestehend aus einem $\sim 24\,\mathrm{g}$ schweren TeO_2 Kristall (Größe $20 \times 20 \times 10\,\mathrm{mm}^3$) und einem Neganov-Luke verstärktem Tieftemperatur-Lichtdetektor (ein $20 \times 20 \times 0.5\,\mathrm{mm}^3$ großer Siliziumabsorber auf welchen vier Elektrodenstreifen aus

Aluminium aufgebracht sind), durchgeführt. Für die Messungen in dieser Arbeit wurde der Neganov-Luke-Lichtdetektor mit einer Spannung von $V_{NL} = 70\,\mathrm{V}$ betrieben. Dabei wurde eine Signalverstärkung um einen Factor ~ 10.8 und eine Verbesserung des Signal-zu-Rausch-Verhältnisses um einen Faktor ~ 6.2 erreicht. Die 1σ-Energieschwelle des mit Neganov-Luke-Spannung betriebenen Lichtdetektors beträgt $\sim 7.8\,\mathrm{eV}$. Um die Unterdrückungseffizienz von α-induzierten Ereignissen bei Energien nahe dem $Q_{\beta\beta}$-Wert von ^{130}Te zu untersuchen, wurde der TeO_2-Kristall mit α-Teilchen aus einer ^{147}Sm α-Quelle und mit γ-Strahlung aus einer ^{228}Th-Quelle bestrahlt.

Durch den Einsatz von Neganov-Luke verstärkten Tieftemperatur-Lichtdetektoren konnte erstmalig eine hocheffiziente Trennung zwischen α- und e^-/γ-induzierten Ereignissen erreicht werden. In einer $\sim$ 42-stündigen Messung konnte eine Unterdrückung von $\gtrsim 99\%$ der α-induzierten Ereignisse erreicht werden bei gleichzeitiger Akzeptanz von 99.8% der e^-/γ-induzierten Ereignisse. Diese Ergebnisse zeigen, dass der α-induzierte Untergrund in $0\nu\beta\beta$-Zerfallsexperimenten mit Tieftemperatur-Detektoren aus TeO_2-Kristallen um ~ 2 Größenordnungen unterdrückt werden könnte, während die Signalakzeptanz praktisch nicht verringert wird.

Es wurden ebenfalls erste Simulationen zum Studium der durch $0\nu\beta\beta$- und γ-induzierte Ereignisse in TeO_2-Kristallen erzeugten Cherenkov-Strahlung und zur Lichtsammeleffizienz in Tieftemperatur-Detektormodulen mit TeO_2-Kristallen durchgeführt. Es konnte gezeigt werden, dass die Intensität der durch γ-induzierte Ereignisse mit einer deponierten Energie von $\sim 2.6\,\mathrm{MeV}$ erzeugten Cherenkov-Strahlung praktisch identisch ist zur Intensität, die durch $0\nu\beta\beta$ Ereignisse von ^{130}Te produziert wird. Die Ergebnisse zeigen weiterhin dass die Menge der detektierbaren Cherenkov-Strahlung durch den Einsatz von Lichtreflektoren mit einer höheren Reflektivität im UV-Spektrum signifikant erhöht werden könnte.

Die Ergebnisse, die in dieser Arbeit erzielt wurden, sind ein wichtiger Meilenstein zur Anwendung von Neganov-Luke verstärkten Lichtdetektoren für die Untergrundunterdrückung in zukünfigen Experimenten zur Suche nach dem $0\nu\beta\beta$-Zerfall mit TeO_2-Tieftemperaturdetektoren.

Contents

Chapter 1

Introduction

The observations of neutrino oscillations, which imply the existence of non-zero neutrino masses and neutrino flavor mixing, provided first indications for the existence of new physics beyond the Standard Model of particle physics [1]. Presently, the absolute neutrino mass scale, the nature of neutrino masses (i.e., the question about the Dirac or Majorana character of neutrinos), the neutrino mass hierarchy, and the existence of lepton number violating processes are unknown and are among the most investigated topics in neutrino and astroparticle physics.

The neutrinoless double beta decay ($0\nu\beta\beta$) decay is a well motivated, hypothetical, second-order weak nuclear decay which is forbidden within the Standard Model of particle physics. An observation would prove the Majorana character of neutrinos and the existence of a lepton number violating process. The search for the $0\nu\beta\beta$ decay can furthermore provide additional information about the neutrino mass hierarchy. Experiments searching for this decay are therefore considered to be one of the most important efforts in neutrino and astroparticle physics.

1.1 Neutrino Oscillations

The first experiment which found indications for the disappearence of solar neutrinos was the radio-chemical Homestake experiment [2] which measured only $\sim$ 1/3 of the expected solar ν_e flux (the so-called "solar neutrino deficit"). This observation was later confirmed by the Super-Kamiokande [3], GALLEX [4], SAGE [5], and GNO [6] experiments which all observed a lower than expected flux of solar neutrinos. The first experiment results which could

show that the total (i.e., $\nu_e + \nu_\mu + \nu_\tau$) solar neutrino flux is in agreement with the prediction of solar models was the Sudbury Neutrino Observatory (SNO) [7, 8] which measured the flux of ν_e was well as the total solar neutrino flux. These measurements provided strong indications that the solar neutrino deficit is in fact due to neutrino oscillations.

The first experiment which directly observed neutrino oscillations (via the disappearance of $\overline{\nu}_e$) was the reactor antineutrino experiment KamLAND [9]. Neutrino oscillations have furthermore been observed in atmospheric [10], accelerator [11], and reactor neutrino experiments [12, 13]. A detailed overview covering neutrino properties, neutrino oscillations and related experiments can be found in [1].

The observation of neutrino oscillations implies non-zero neutrino masses, the existence of neutrino flavor mixing (i.e., the flavor eigenstates are not identical to the neutrino mass eigenstates) and the non-conservation of the lepton family number. It therefore provides compelling evidence for new physics beyond the Standard Model.

The current experimental data is consistent with 3-neutrino mixing in vacuum[1]. The flavor eigenstates ν_α ($\alpha = e, \mu, \tau$) are described as a coherent superposition of mass eigenstates ν_i ($i = 1, 2, 3$) with mass eigenvalues m_i:

$$|\nu_\alpha\rangle = \sum_{i=1}^{3} U^*_{\alpha i} \, |\nu_i\rangle \tag{1.1}$$

Here, U_{ij} is the 3×3 unitary neutrino mixing matrix, the Pontecorvo-Maki-Nakagawa-Sakata (PMNS) matrix (see, e.g., [15]):

$$U = \begin{bmatrix} c_{12}c_{13} & s_{12}c_{13} & s_{13}e^{-i\delta} \\ -s_{12}c_{23} - c_{12}s_{23}s_{13}e^{i\delta} & c_{12}c_{23} - s_{12}s_{23}s_{13}e^{i\delta} & s_{23}c_{13} \\ s_{12}s_{23} - c_{12}c_{23}s_{13}e^{i\delta} & -c_{12}s_{23} - s_{12}c_{23}s_{13}e^{i\delta} & c_{23}c_{13} \end{bmatrix} \times \mathrm{diag}\left(e^{i\lambda_1}, \, e^{i\lambda_2}, \, 1\right)$$

where $s_{ij} = \sin(\theta_{ij})$ and $c_{ij} = \cos(\theta_{ij})$ are the sine and cosine of the mixing angles θ_{ij}. The mixing of three neutrino flavors can be fully parameterized using: two neutrino squared mass differences (e.g., Δm^2_{12} and Δm^2_{23}), three mixing angles θ_{12}, θ_{23}, θ_{13}, and three phases, the Dirac CP violating phase δ

[1] Presently, there are experimental results which could be explained by the existence of additional sterile neutrinos (see, e.g., [14])

and the Majorana CP violating phases λ_1 and λ_2.

The probability of observing a neutrino created with flavor α as a neutrino with flavor β (i.e., the probability of observing the transition $\nu_\alpha \to \nu_\beta$) in vacuum is given by (see, e.g., [15]):

$$P_{\nu_\alpha \to \nu_\beta} = \delta_{\alpha\beta} - 4 \sum_{i>j} \mathrm{Re}\Big[U^*_{\alpha i}\, U^*_{\beta j}\, U_{\beta i}\, U_{\alpha j}\Big] \sin^2 \frac{\Delta m^2_{ij} L}{4E} + 2 \sum_{i>j} \mathrm{Im}\Big[U^*_{\alpha i}\, U^*_{\beta j}\, U_{\beta i}\, U_{\alpha j}\Big] \sin \frac{\Delta m^2_{ij} L}{2E} \tag{1.2}$$

where E is the energy of the neutrino and L is the distance between the neutrino source and the detector. From equation (1.2) it can be seen that experiments investigating neutrino oscillation phenomena are only sensitive to the mass squared differences Δm^2_{ij}. Present results of a global analysis of neutrino oscillation data are given in table 1.1. The parameters Δm^2_{12} and $\sin^2\theta_{12}$ can be mainly measured via the oscillation of solar and atmospheric neutrinos[2] while $|\Delta m^2_{23}|$ and $\sin^2\theta_{23}$ can be determined using atmospheric and long baseline accelerator neutrino experiments [1].

Since the sign of Δm^2_{23} has not yet been measured, different orderings of the neutrino masses can be considered (this is referred to as "mass hierarchy"):

- *Normal hierarchy (NH)*: $m_1 < m_2 < m_3$
- *Inverted hierarchy (IH)*: $m_3 < m_1 < m_2$
- *Quasi-Degenerate (QD)*: $m_1 \simeq m_2 \simeq m_3$

Presently, several experiments using accelerator [18], atmospheric [19, 20], and reactor [21] neutrinos have been proposed in order to determine the sign of Δm^2_{23} and, therefore, determine the hierarchy of neutrino masses.

Experiments studying neutrino oscillations are only sensitive to the mass squared differences (Δm^2_{ij}) and cannot determine the absolute neutrino mass scale. However, these parameters are accessible by studying the so-called "neutrino absolute mass observables":

- The endpoint and shape of the β-spectrum depends directly (via the phase space of the β decay) on the rest mass of the emitted neutrino [22]

[2]The sign of Δm^2_{12} has been determined via the observation of the MSW effect with solar neutrinos (see, e.g., [16]).

Parameter	Spectrum	Best fit	1σ range
Δm^2_{12} $[10^{-5}\,\mathrm{eV}^2]$	NH or IH	7.54	$7.32 - 7.80$
$\sin^2\theta_{12}$ $[10^{-1}]$	NH or IH	3.08	$2.91 - 3.25$
$\lvert\Delta m^2_{23}\rvert$ $[10^{-3}\,\mathrm{eV}^2]$	NH	2.38	$2.32 - 2.44$
	IH	2.43	$2.37 - 2.49$
$\sin^2\theta_{23}$ $[10^{-1}]$	NH	4.37	$4.14 - 4.70$
	IH	4.55	$4.24 - 5.94$
$\sin^2\theta_{13}$ $[10^{-2}]$	NH	2.34	$2.15 - 2.54$
	IH	2.40	$2.18 - 2.59$

Table 1.1: Neutrino mixing parameters and 1σ ranges obtained from a global analysis of experimental oscillation data. Δm_{23} is defined as $m_3^2 - (m_1^2 + m_2^2)/2$. Values taken from [17].

which can be written as:

$$\langle m_\beta \rangle = \sqrt{\sum_i |U_{ei}|^2 m_i^2} \tag{1.3}$$

This parameter can be determined via precision measurements of the kinematics of the electron emitted in β decay. Currently, the best upper limits on $\langle m_\beta \rangle$ are provided by the Mainz [23] and Troitzk [24] experiments by measuring the kinematics at the endpoint of the Tritium (^{3}H) β decay:

$$\langle m_\beta \rangle < 2.1\,\mathrm{eV} \qquad (95\,\%\,\mathrm{CL.}) \tag{1.4}$$

In the future the KATRIN experiment, which has a projected sensitivity of $\langle m_\beta \rangle \sim 0.2\,\mathrm{eV}$, will start taking data [25, 26]. Additionally, there are further experimental approaches under investigation which aim to perform precision calorimetric measurements of the kinematics of the β endpoint in ^{187}Re and the electron capture in ^{163}Ho using cryogenic detectors (MaRe [27] and ECHo [28]).

- Upper bounds on the sum of the neutrino masses

$$\sum m_\nu \tag{1.5}$$

can be determined by precision measurements of the fluctuations in the Cosmic Microwave Background (CMB). Currently, the best upper limit on the sum of the neutrino masses is $\sum m_\nu < 0.66\,\mathrm{eV}$ (95 % CL., considering only CMB data) is obtained from measurements performed by ESA's Planck satellite [29, 30]. Furthermore, upper limits of $\sum m_\nu$ can be derived via the cosmological structure formation [31] and from time of flight measurements of neutrinos emitted in supernovae [32].

In addition to these parameters, the half life of the $0\nu\beta\beta$ decay depends on the effective neutrino Majorana mass which can be written as a function of the oscillation parameters (see eq. (1.9) in the next section) and an observation of this decay can therefore provide additional information about the hierarchy of neutrino masses.

An overview of the correlation between the different neutrino mass observables can be found in [33].

1.2 Neutrinoless Double Beta Decay

Within the Standard Model of particle physics, the so-called double beta decay is a second order weak nuclear decay which can be observed in certain even-even isotopes where the β^- decay is energetically forbidden [34]:

$$(A, Z) \rightarrow (A, Z+2) + 2\mathrm{e}^- + 2\overline{\nu}_\mathrm{e} \tag{1.6}$$

This decay, which is also refereed to as two-neutrino double beta decay ($2\nu\beta\beta$), is characterized by the simultaneous decay of two neutrons into two protons and the emission of two electrons and two electron-antineutrinos (a diagram of this decay is shown in the left panel of figure 1.1). This decay has been observed experimentally for several isotopes with half lifes of $\mathcal{O}(10^{19} - 10^{21}\,\mathrm{yr})$ [35].

Another possible realization of this process where no neutrinos are emitted in the final state is the so-called neutrinoless double beta decay ($0\nu\beta\beta$):

$$(A, Z) \rightarrow (A, Z+2) + 2\mathrm{e}^- \tag{1.7}$$

Since this process violates lepton-number conservation (the lepton number in the initial and final state differs by 2), it is forbidden within the Standard Model of particle physics and current experimental limits on the half life of this

process for different candidate isotopes are in the range of $\mathcal{O}(10^{21}-10^{25}$ yr [36].

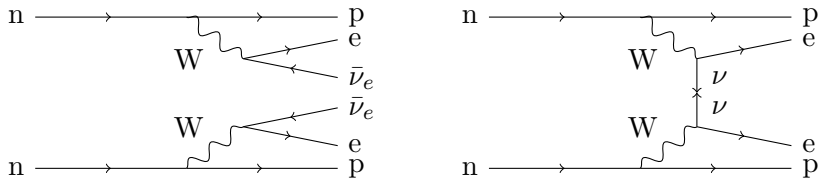

Figure 1.1: Feynman diagram for the two-neutrino double beta decay ($2\nu\beta\beta$, left panel) as well as the neutrinoless double beta decay ($0\nu\beta\beta$, right panel), mediated by light Majorana neutrinos.

Different mechanisms for the $0\nu\beta\beta$ decay can be considered (see, e.g., [37]). However, according to the Schechter-Valle theorem [38], all realizations of the $0\nu\beta\beta$ decay lead to a non-zero effective Majorana mass-term. The simplest mechanism for the $0\nu\beta\beta$ decay typically considered is the exchange of light Majorana neutrinos (right panel in figure 1.1). An observation of the $0\nu\beta\beta$ decay would therefore establish the Majorana character of neutrinos and the existence of a lepton number violating process.

Assuming the exchange of light Majorana neutrinos as the dominant process mediating the $0\nu\beta\beta$ decay, the half-life of the double beta decay can be written as [36]:

$$(T^{0\nu}_{1/2})^{-1} = G_{0\nu}(Q_{\beta\beta}, Z)|M_{0\nu}|^2 \langle m_{\beta\beta}\rangle^2 \tag{1.8}$$

where $G_{0\nu}(Q_{\beta\beta}, Z)$ is the phase space factor, $M_{0\nu}$ is the nuclear matrix element (NME), and $\langle m_{\beta\beta}\rangle$ is the effective Majorana mass. The phase space factor $G_{0\nu}(Q_{\beta\beta}, Z)$ can be calculated analytically (see, e.g., [39]) while the nuclear matrix element can only be calculated using approximative methods and its value depends strongly on the chosen approximation (for an overview covering various theoretical models used for the calculation of NMEs, see [15, 36]).

The effective Majorana mass of the electron neutrino can be written as a function of neutrino oscillation parameters [36]:

$$\begin{aligned}\langle m_{\beta\beta}\rangle &= \left|\sum U_{ei}^2 m_i\right| \\ &= \left|c_{13}^2 c_{12}^2 e^{2i(\lambda_1+\delta)} m_1 + c_{13}^2 s_{12}^2 e^{2i(\lambda_2+\delta)} m_2 + s_{13}^2 m_3\right|\end{aligned} \tag{1.9}$$

where m_i are the neutrino mass eigenvalues and U_{ei} are the entries of the

neutrino mixing matrix. Figure 1.2 shows a plot of the allowed regions of the effective Majorana mass as a function of the lightest neutrino mass ($m_{min} = m_1$ for the normal mass hierarchy and $m_{min} = m_3$ for the inverted mass hierarchy). The plot furthermore shows present experimental lower limits on the effective Majorana mass from $0\nu\beta\beta$ experiments and on the mass of the lightest neutrino, obtained from cosmological observations. It can be seen that the hierarchy of neutrino masses has influence on the effective neutrino Majorana mass and, therefore, the half life of the decay.

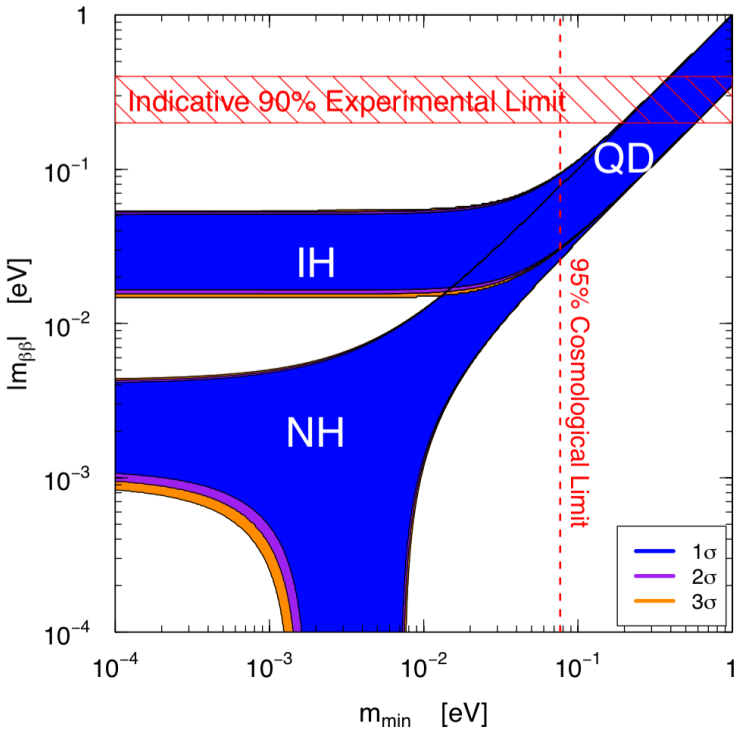

Figure 1.2: Allowed values for the effective Majorana mass as a function of lightest neutrino mass for the normal (NH), inverted (IH) and quasi-degenerate (QD) hierarchy. Figure taken from [15].

In the following, the experimental aspects influencing the sensitivity of $0\nu\beta\beta$-decay experiments on the half life $T^{0\nu}_{1/2}$ of the decay will be discussed.

1.3 Experimental Aspects of $0\nu\beta\beta$ Searches

The total amount of energy released in the $\beta\beta$-decay is given by the Q-value ($Q_{\beta\beta}$) of the decay:

$$Q_{\beta\beta} = M(Z, A) - M(Z + 2, A) - 2m_e \tag{1.10}$$

where $M(Z, A)$ is the mass of the parent nucleus, $M(Z + 2, A)$ is the mass of the daughter nucleus and $2m_e$ is the rest mass of the two electrons emitted in the process. In the $0\nu\beta\beta$ decay, the two electrons carry the total released energy while in the $2\nu\beta\beta$ decay, part of the energy is carried away undetected by the two neutrinos. Therefore, the experimental signature in experiments measuring the total energy carried by the two electrons is a peak at the $Q_{\beta\beta}$ value for the $0\nu\beta\beta$ decay and a a continuous energy spectrum for the $2\nu\beta\beta$ decay (see figure 1.3). The detection efficiency for the two electrons can be maximized when the detector material contains the $0\nu\beta\beta$-decaying isotope (also referred to as "source = detector" approach).

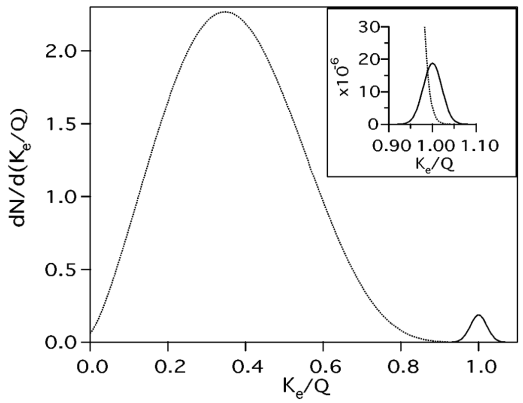

Figure 1.3: Spectra of the sum energy (K_e) of the two electrons emitted in the $2\nu\beta\beta$ (dotted line) and $0\nu\beta\beta$ (solid line) decays. An energy resolution of 5% is assumed. Figure taken from [40].

The energy interval around the endpoint $Q_{\beta\beta}$ is referred to as the region of interest (ROI) and its width is determined by the energy resolution of the detector and by potential background sources present in the experiment. By analyzing the observed number of events in the ROI compared to the expected number of background events, limits on the half-life of the $0\nu\beta\beta$ decay ($T^{0\nu}_{1/2}$) can be inferred.

The expected number of $0\nu\beta\beta$ events ($\lambda_{0\nu\beta\beta}$) in a certain measurement-time t can be calculated as:

$$\lambda_{0\nu\beta\beta}(t) = \epsilon \cdot N_{\beta\beta} \cdot \left(1 - e^{-t/\tau}\right) \overset{t \ll \tau}{\approx} \epsilon \cdot N_{\beta\beta} \cdot t/\tau = \epsilon \cdot N_{\beta\beta} \cdot \ln(2) \cdot \frac{t}{T^{0\nu}_{1/2}} \quad (1.11)$$

where ϵ is the detection efficiency, $N_{\beta\beta}$ is the number of $\beta\beta$-decaying atoms, and $T^{0\nu}_{1/2}$ is the half-life of the decay ($\tau = {}^{T^{0\nu}_{1/2}}/_{\ln 2}$). Assuming that the rate of background induced events scales with the detector mass, the expected number of background events in the ROI can be calculated as:

$$\lambda_{bkg}(t) = b \cdot M \cdot \Delta E \cdot t \quad (1.12)$$

where M is the active detector mass (in kg), ΔE is the width of the ROI (in keV), b is the background index (given in counts/keV/kg/year), and t is the measuring time in years.

In order to compare the potential of different experimental approaches, the half life corresponding to the number of signal events detectable at a given background index (referred to as "experimental sensitivity S") is typically given [15]:

$$S^{0\nu} = \ln(2) \cdot \epsilon \cdot i.a. \cdot \frac{N_A}{m_{mol}} \cdot \sqrt{\frac{M \cdot t}{b \cdot \Delta E}} \quad (1.13)$$

where ϵ is the detection efficiency, $i.a.$ is the isotopic abundance of the $0\nu\beta\beta$-decaying isotope, N_A is the Avogadro number, and m_{mol} is the molecular weight (of the molecule containing the $0\nu\beta\beta$-decaying isotope).

From equation (1.13) it can be seen that a $0\nu\beta\beta$-decay experiment should fulfill the following criteria in order to maximize the experimental sensitivity:

- The experiment should operate a large detector mass (of up to $\mathcal{O}(1\,\text{ton})$), ideally enriched in the $0\nu\beta\beta$-decaying isotope, for a long measurement time (of up to several years).
- The experiment should have a large detection efficiency (experiments using the "source = detector" approach can have a detection efficiency of up to $\mathcal{O}(90\,\%)$).
- The experiment should have a very good energy resolution ($\lesssim 1\,\%$ at $Q_{\beta\beta}$) in order to identify the expected peak in the energy spectrum.
- Operation of the experiment in a very low background environment with a background index of $\lesssim 0.1$counts/keV/kg/year.

Achieving a low background in the ROI is particularly important since the number of background induced events directly influences the achievable sensitivity. The main background in $0\nu\beta\beta$-decay experiments is typically due to natural radioactivity. In the energy range relevant for $0\nu\beta\beta$-decay experiments ($E \lesssim 5\,\mathrm{MeV}$), the main radioactive background is due to the isotopes occurring in the decay chains of ^{238}U and ^{232}Th, which include α, β, and γ emitting isotopes. The half lifes of these isotopes are much smaller than the present limits on the half lifes of $0\nu\beta\beta$-decaying isotopes and, therefore, even a contamination with traces of these isotopes can lead to a significant number of background events. From the isotopes of these decay chains, a contamination with the α-decaying isotopes ^{220}Rn and ^{222}Rn is particularly dangerous for experiments where the whole detector volume acts as an active detector (e.g., in cryogenic bolometers) and no discrimination of surface events is possible. Since these isotopes are gaseous, they can diffuse into the surface of the detector materials and the support structure surrounding them. α particles emitted within several μm of the surface of these materials can loose part of their energy before escaping the material and lead to a continuous, energy degraded, spectrum of α-particles. Apart from the natural radioactivity, cosmic rays can produce background events either via a direct interaction in the detector material or via the production of secondary particles (neutrons) and cosmogenic isotopes.

In order to reduce the exposure to cosmic rays, the experiments are typically located in underground facilities where the flux of atmospheric muons is educed by several orders of magnitude and muon veto systems are employed to identify events in coincidence with muons passing through the experimental setup. Additionally, the active detector material is surrounded by an "onion-like" shielding structure, gradually increasing the radiopurity of the employed materials towards the active detector. There, high-Z materials (typically copper and lead) are used to shield the experiments from external gamma radiation while hydrogen-rich materials (e.g., polyethylene) are used to moderate fast neutrons.

Apart from the afore mentioned criteria, the selection of the candidate isotope is an important aspect for $0\nu\beta\beta$-decay experiments. A large Q-value of the respective isotope is favorable due to several reasons: it ensures a "fast" decay rate ($\propto (Q_{\beta\beta})^5$ [41]) and reduces the background due to $2\nu\beta\beta$-decay events[3]. In order to achieve a large mass of the candidate isotope, its natural

[3]The fraction of $2\nu\beta\beta$ events within an energy window ΔE, centered around $Q_{\beta\beta}$, is proportional to ${}^{\Delta E^6}/_{Q^5_{\beta\beta}}$ [40]. Therefore, apart from a large Q-value, the background due to $2\nu\beta\beta$-decay events can be reduced by improving the energy resolution of the experiment.

abundance should be high and, furthermore, the detector material containing the candidate isotope should be available on a $\mathcal{O}(1\,\text{ton})$ scale and should provide the possibility for isotopic enrichment. An overview about candidate isotopes, their Q-values, and isotopic abundances can be found in [15].

A variety of different experimental approaches are currently being pursued in order to search for the $0\nu\beta\beta$ decay. These include for example high-purity germanium diodes (GERDA [42], MAJORANA [43]), cryogenic bolometers (CUORE0 & CUORE [44, 45], LUCIFER [46], LUMINEU [47, 48]), liquid scintillator detectors (KamLAND-Zen [49]), and liquid noble gas time projection chambers (EXO [50]). A review about the present status of $0\nu\beta\beta$-decay experiments can be found in [51].

The present generation of $0\nu\beta\beta$ experiments has a sensitivity on the $0\nu\beta\beta$ half life of $\mathcal{O}(10^{25}\,\text{yr})$ which corresponds to an effective Majorana mass of $\mathcal{O}(0.1 - 0.2\,\text{eV})$ (see, e.g., figure 1.3) and the next generation of experiments (e.g., CUORE [44, 45] and GERDA Phase II [42]) has a projected sensitivity of $\sim 10^{26}\,\text{yr}$ (corresponding to $\langle m_{\beta\beta}\rangle \approx 50\,\text{meV}$). In order to probe the inverted hierarchy region of the neutrino mass spectrum, experiments with a sensitivity on the half life $T^{0\nu}_{1/2}$ of $\mathcal{O}(10^{27} - 10^{28}\,\text{yr})$ (corresponding to $\langle m_{\beta\beta}\rangle \approx 10\,\text{meV}$) are required. The main efforts of future experiments striving to reach this ambitious goal are an increase in the mass of the candidate isotope via isotopic enrichment and a significant reduction of the radioactive background in the region of interest.

Active background suppression techniques, capable of efficiently discriminating background events while simultaneously maintaining a high signal acceptance, are expected to become increasingly important. For bolometric experiments, the active suppression of background events based on the simultaneous detection of the heat signal and the emitted scintillation light in a separate cryogenic light detector are presently being investigated [46, 47]. This technique is know as "phonon-light technique" and is currently successfully employed by the direct dark matter search experiment CRESST-II [52].

Experiments using cryogenic bolometers based on TeO_2 crystals (e.g. CUORE0 & CUORE [44, 45]) are, due to their excellent energy resolution ($\sim 6\,\text{keV}$ in the ROI [45]) and high natural abundance of ^{130}Te ($\sim 35\,\%$ [53]), among the most promising experimental approaches in the search for the $0\nu\beta\beta$ decay. Since TeO_2 crystals are non-scintillating, the phonon-light technique cannot be employed directly. However, a novel experimental approach [54] for the background suppression in non-scintillating crystals is based on the detection

of the Cherenkov radiation emitted by highly energetic electrons in the TeO_2 crystal to discriminate e^-/γ-induced events at $Q_{\beta\beta}(^{130}\mathrm{Te}) \approx 2.5\,\mathrm{MeV}$ from α-induced background events.

In the present work (see also [55]), the application of Neganov-Luke amplified cryogenic light detectors (read out using transition edge sensors) for the background suppression in TeO_2 bolometers is investigated for the first time. In chapter 2, the working principle of cryogenic detectors with transition edge sensor readout, of Neganov-Luke amplified cryogenic light detectors as well as the background suppression based on the detection of Cherenkov radiation emitted from TeO_2 crystals is introduced. Chapter 3 describes simulations performed to study the production of Cherenkov radiation by $0\nu\beta\beta$- and γ-induced events. The experimental setup used for the low-temperature measurements performed in the present work as well as the fabrication of transition edge sensors and of Neganov-Luke light detectors is described in chapter 4. The highly promising results of measurements performed with a new low-temperature detector module consisting of a TeO_2 crystal ($20 \times 20 \times 10\,\mathrm{mm}^3$ with a mass $\sim 24\,\mathrm{g}$) and a Neganov-Luke amplified cryogenic light detector (consisting of a $20 \times 20 \times 10\,\mathrm{mm}^3$ silicon substrate equipped with four aluminum electrode strips deposited onto the crystal facing side of the substrate) are discussed in chapter 5.

Chapter 2

Detector Physics

The Neganov-Luke (NL) effect [56, 57] provides a method to amplify the heat signals in a cryogenic light detector and therefore increase the sensitivity of the detector. Such detectors have previously been investigated in the framework of the dark matter experiments CRESST [52] and EURECA [58] by [59, 60, 61]. In the present work, the application of NL light detectors for the background suppression in $0\nu\beta\beta$-decay experiments using TeO_2 bolometers and the phonon-light technique is investigated [55].

Using the so-called phonon-light technique, different kinds of interactions in a (typically scintillating) target crystals can be actively discriminated by simultaneously measuring the heat signal in the target crystal and a corresponding (scintillation) light signal in a separate low-temperature light detector. This technique is presently used in the direct dark matter search experiment CRESST-II [52] and its application to new fields of physics, e.g., the search for the $0\nu\beta\beta$ decay with low-temperature detectors, is also being investigated by several groups (see, e.g., [46, 47, 62, 63]).

A novel application of the phonon-light technique is the discrimination between α- and e^-/γ-induced events in cryogenic bolometers which employ non- scintillating target crystals via the detection of Cherenkov radiation produced by highly energetic electrons within the crystal [54]. An application of this technique with high significance for the search for the $0\nu\beta\beta$ decay is the suppression of α-induced background events in non-scintillating TeO_2 bolometers which are currently being used in the search for the $0\nu\beta\beta$ decay of ^{130}Te (see, e.g., [64]). Due to the small amount of expected light (the expected amount of Cherenkov light is $\mathcal{O}(0 - 400\,\mathrm{eV})$ for electrons with energies close to the Q-value of ^{130}Te at $\sim 2.5\,\mathrm{MeV}$), very sensitive cryogenic light detectors are required.

In the following, the working principle of cryogenic detectors with transition edge sensor readout, of NL amplified light detectors and the phonon-light technique in general as well as its application for the background suppression via the detection of Cherenkov radiation are discussed in more detail.

2.1 Cryogenic Detectors with TES Readout

2.1.1 Basic Working Principle of Cryogenic Detectors

A cryogenic detector typically consists of an absorber (target) crystal equipped with a very sensitive thermometer used to measure the heat signal induced by particle interactions within the absorber. In the present work, superconducting transition edge sensors (TES) are used to readout the heat signal. Figure 2.1 shows a schematic representation of such a cryogenic detector.

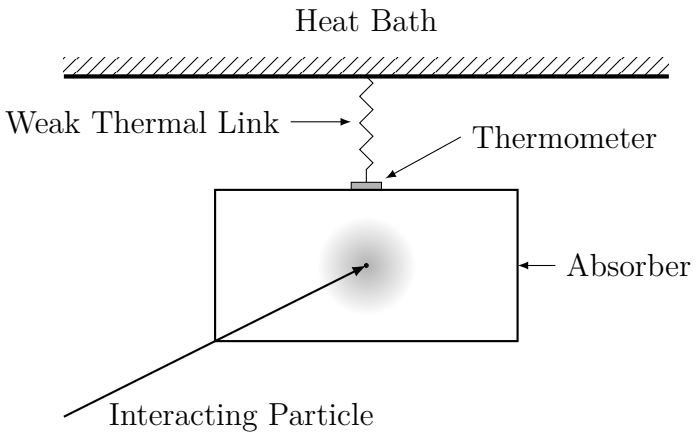

Figure 2.1: Schematic representation of a cryogenic particle detector consisting of an absorber equipped with a very sensitive thermometer. Particle interactions within the absorber lead to an energy deposition which increases the thermometers temperature. This temperature change is translated into an electrical signal using the temperature dependent electrical resistance of the thermometer. After the energy deposition, thermal equilibrium with the heat bath is reestablished via the weak thermal link.

Particle interactions with the absorber material lead to an energy deposition (ΔE) which, assuming full thermalization of the deposited energy, induces an increase in the absorber temperature (ΔT) via the excitation of lattice vibrations (i.e., phonons). The energy deposition and thermalization processes in

the absorber depend on the kind of interacting particle and are described, e.g., in [59]. This temperature rise is measured using the thermometer (here: TES) and thermal equilibrium conditions are reestablished via the weak thermal link between the thermometer and the heat bath.

Assuming the deposited energy is fully thermalized in an absorber with heat capacity C, the temperature rise is given by:

$$\Delta T = \frac{\Delta E}{C} \tag{2.1}$$

The heat capacity C of typical absorber materials exhibit a strong temperature dependence. Depending on the kind of absorber material (e.g., insulator, metal or semiconductor material), both the crystal lattice ($C_{lattice} \propto T^3$) and the electrons ($C_{electronic} \propto T$) in the solid can contribute to the total heat capacity [65]. In insulator and semiconductor absorbers at low temperatures, only the phonons contribute significantly to the heat capacity. In order to maximize the temperature rise ΔT, these kind of detectors are operated at cryogenic temperatures of ($\mathcal{O}(10 - 100\,\mathrm{mK})$) where the heat capacity is very small.

When operating a cryogenic detector, the temperature of the heat bath is held constant at a temperature T_{bath}. In an idealized detector, the temperature of the absorber increases almost instantaneously after the energy deposition and will return to thermal equilibrium conditions ($T = T_{bath}$) via an exponential decay with the time-constant

$$\tau = \frac{C}{G} \tag{2.2}$$

which is determined by the heat capacity of the absorber (C) and the thermal conductivity (G) of the weak thermal link.

In an actual cryogenic detector additional components apart from the absorber crystal, e.g., the heat capacity of the TES and the thermal couplings between the individual components, have to be considered in order to describe the time evolution of the heat signal within the absorber and the thermometer. A thermal model describing the characteristics of such detectors is discussed in [66]. In the following, the working principle of transition edge sensors will be discussed further:

2.1.2 Working Principle of Transition Edge Sensors

Transition edge sensors (TES) are superconducting thin films, temperature stabilized in the narrow transition region between the normal- and superconducting state. Such devices can be operated as very sensitive thermometers which, due to the strong relation between resistance and temperature within the transition region, translate small temperature variations into electrical signals. A detailed review about the physics of transition edge sensors can be found in [67].

The working principle of a TES is illustrated in figure 2.2. In the transition region, the superconducting film exhibits a strong temperature dependence of the film resistance. A small change in the TES temperature (ΔT_{TES}) corresponds to a significant change in resistance (ΔR_{TES}) which can be translated into an electrical signal. To achieve an optimal sensitivity of the sensor, the transition curve should be very steep and linear over a large part of the transition.

If the particle induced temperature changes ΔT_{TES} are much smaller than the width of the transition, the resistance change in the transition region can be approximated by a linearized relation:

$$\Delta R_{TES} = \frac{\delta R}{\delta T} \cdot \Delta T_{TES} \tag{2.3}$$

where $\delta R/\delta T$ is the slope of the transition.

During the operation of a cryogenic detector with TES readout, the temperature of the heat bath is actively stabilized at a temperature below the transition temperature of the TES film. By applying a bias current I_{Bias} to the TES, the superconducting film is additionally heated up to a working point T_{wp} within its transition region by the Joule power dissipated by the bias current within the film. A certain working point is therefore characterized by the temperature of the heat bath (T_{bath}) and the applied bias current (I_{Bias}).

The detectors developed in the present work are read out with transition edge sensors based on so-called proximity bi-layers which consist of a sandwich structure of a superconducting and a normalconducting metal. The transition temperature of such bi-layers is reduced with respect to the transition temperature of the superconductor due to the so-called proximity effect [68, 69]. The transition temperature of the TES can be varied by changing the relative

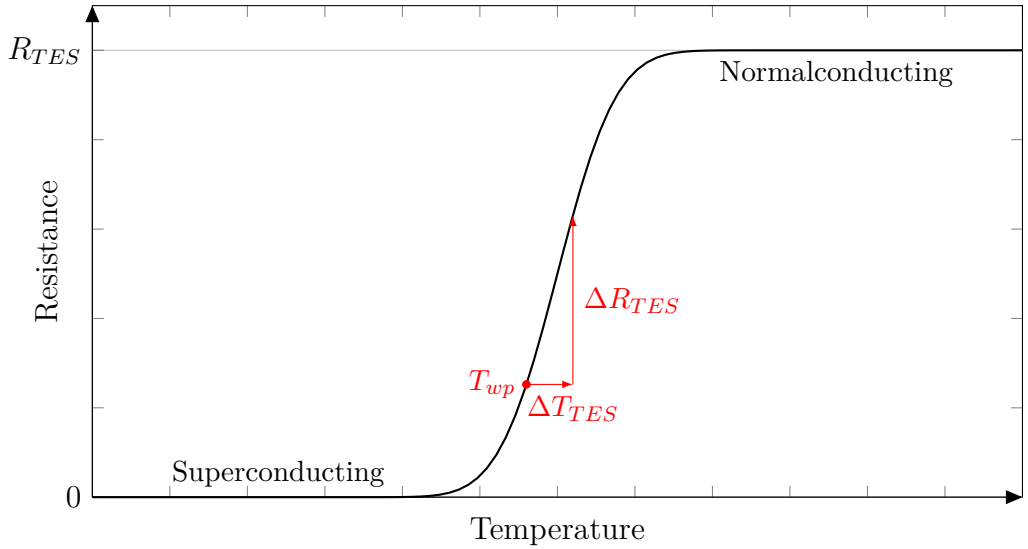

Figure 2.2: Illustration of the working principle of a transition edge sensor (TES): A superconducting thin-film is operated at a working point (T_{wp}) in the narrow transition region between the normal- and superconducting state (characterized by the resistance $R = R_{TES}$ and $R = 0$ respectively). An energy deposition increases the TES temperature (ΔT_{TES}) and, due to the strong temperature dependence of the film resistance, increases the film resistance (ΔR_{TES}). This resistance change can be translated into an electrical signal.

thicknesses of the individual layers.

In this work IrAu TESs [70, 71], which consist of thin iridium ($T_C(\mathrm{Ir}) = 112.5\,\mathrm{mK}$ [72]) and gold films, are used. The transition temperature can be varied between $\sim 20 - 80\,\mathrm{mK}$ by varying the thicknesses of the individual layers. The fabrication of such transition edge sensors is described in section 4.1.1.

The readout of cryogenic detectors with TES is described in section 4.3.2.

2.1.3 The Composite Detector Design

The cryogenic detectors used for the measurements in this work are manufactured according to the so-called composite detector design (CCD) [73]. The TES is first deposited onto a separate carrier substrate and then glued onto

the absorber using epoxy resin[1].

This technique has several advantages compared to the direct deposition of the TES film onto the absorber crystal:

- Since the carrier substrate can be chosen to be much smaller than the main absorber crystal, multiple TES carriers can be produced simultaneously. This is especially important for the mass production of TESs for future experiments searching for rare events (e.g., EURECA [58]).
- Furthermore, the TESs can be characterized separately from the target crystal and be preselected, especially with respect to the transition temperature and the linearity of the transition.
- The TES films are typically deposited at high temperatures ($\sim 300 - 500\,^{\circ}\mathrm{C}$) in an ultra-high vacuum chamber (at a pressure of $\mathcal{O}(10^{-9} - 10^{-11}\,\mathrm{mbar})$). This can lead to a loss of oxygen from crystals (e.g., $CaWO_4$) which can deteriorate the light yield of scintillating crystals (see, e.g., [74] and references therein).
- For cryogenic light detectors with Neganov-Luke amplification (which will be discussed in section 2.2), the CCD provides an electrical insulation between the TES and the absorber substrate [59].

The glue spot between the absorber and the TES adds an additional thermal coupling which has to be considered when describing the characteristics of such detectors. A theoretical model describing cryogenic detectors build according to the composite detector design is discussed in [61].

2.2 Neganov-Luke Amplified Cryogenic Light-Detectors

The so-called Neganov-Luke (NL) effect [56, 57] describes an amplification of the heat signal in cryogenic detectors with semiconductor absorbers. As has been shown in [61], cryogenic light detector with NL amplification have tremendous potential to improve the background suppression in cryogenic rare-event search experiments by improving the light detector's threshold and energy resolution, especially at low energies. The application of the NL effect

[1] In "classical" cryogenic detectors with TES readout, the TES is deposited directly onto the absorber.

in cryogenic calorimeters was first studied in [75] and first measurements with cryogenic light-detectors employing the NL effect were conducted in [76, 77]. The application of such light detectors to the phonon-light technique and the background suppression in experiments using $CaWO_4$-crystals have been studied in [59, 60] and [61].

In the present work, the application of the phonon-light technique with NL-amplified light detectors to the background suppression in experiments employing TeO_2 crystals for the search for $0\nu\beta\beta$ decay is investigated (see section 2.3.2). First measurements with a low-temperature detector module consisting of a TeO_2 phonon detector and a NL amplified light detector have been performed (see chapter 5).

2.2.1 The Neganov-Luke Effect

The NL amplification of the heat signal is observed in cryogenic detectors with semiconductor absorbers when electrons and holes, induced by particle interactions within the absorber, are drifted in an electric field applied to the absorber. The electrons and holes are accelerated and transfer their increased energy to the phonon system of the absorber via scattering off the crystal lattice and the production of high-frequency phonons [59]. The expected theoretical thermal gain G_{th} due to the Neganov-Luke effect depends on the applied voltage and can be described by the following equation:

$$G_{th} = 1 + \frac{e \cdot V_{NL}}{\epsilon} \tag{2.4}$$

where e is the elementary charge, V_{NL} is the applied Neganov-Luke voltage and ϵ is the average energy of the electron-hole pairs produced in the energy deposition process. This energy depends on the absorber material and the type of interacting particle. For X-rays in silicon, the mean energy of an electron-hole pair is $\epsilon = 3.76\,\text{eV}$ [78] while for light, ϵ is given by $\epsilon = E_{ph}/\eta$ [76] where E_{ph} is the mean energy of the detected photons and η is the quantum efficiency for electron-hole pair production. In the spectral range relevant for the detection of Cherenkov light emitted from TeO_2 crystals as well as for experiments searching for direct dark matter interactions in $CaWO_4$ crystals, η is close to unity [79]. Therefore, each absorbed photon leads to the generation of an electron-hole pair ($N_{eh} = N_{ph}$)[2].

[2] In the present work, the relevant spectral range stretches from $\sim 390\,\text{nm}$ to $\sim 1000\,\text{nm}$ (compare section 2.4). For wavelenghts below $\sim 390\,\text{nm}$, the probability of creating multiple electron hole pairs increases (see [79]) which can lead to an increased thermal gain G_{th}.

A schematic representation of a cryogenic light detector with NL amplification is depicted in figure 2.3. The electron-hole pairs, created, for example, by the absorption of light at the surface of the silicon substrate, are drifted in the electric field generated by the Neganov-Luke voltage applied between the aluminum electrodes.

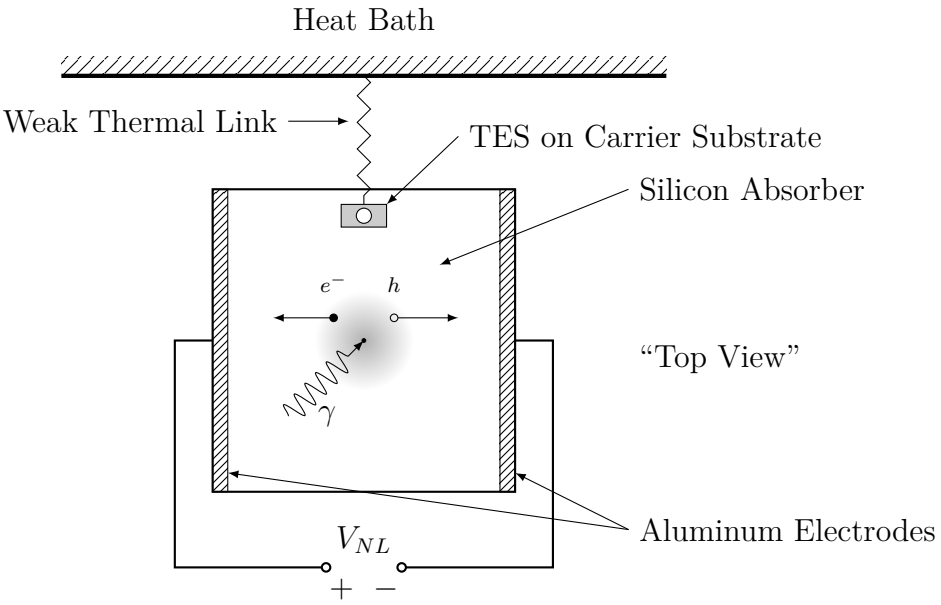

Figure 2.3: This figure illustrates the working principle of a cryogenic light detector with Neganov-Luke amplification. Electron-hole pairs, created for example by the absorption of light at the absorber surface, are drifted in the electric field generated by the voltage V_{NL} applied between the aluminum electrodes. The energy gained by the electrons while being drifted in the electric filed is transferred to the absorber crystal in the form of phonons which leads to an amplification of the heat signal in the absorber. An IrAu TES (deposited onto a TES carrier substrate, which is glued onto the silicon absorber) is used to measure the heat signal.

2.2.2 Problems of Realized NL Light Detectors

Equation (2.4) assumes that all charge carriers are collected at the electrodes and that the NL voltage is constant with time. In real detectors, however, several effects can lead to a reduction of the observed thermal gain [76]:

- Charge carriers can be trapped in defects or impurities within the semiconductor absorber before they reach the electrodes. This reduces the effective thermal gain by the average fraction of the electric field traversed by the electron and hole. If d is the distance between the electrodes and l is the average drift length of the charge carriers, the thermal gain is reduced by a factor of $^{l}/_{d}$.
- Charge carriers can accumulate in the vicinity of the electrodes. The deposition of the aluminum electrodes can produce additional trapping sites and defects below the electrodes. This accumulation leads to the generation of an electric field with reverse polarity and effectively reduces the NL voltage ($V_{NL,eff}(t)$) with time.

The effective thermal gain which takes these additional factors into account can be written as [76]:

$$G_{th,eff}(t) = 1 + \frac{e \cdot V_{NL,eff}(t)}{\epsilon} \cdot \frac{l}{d} \tag{2.5}$$

These effects can impose general limitations on the application of cryogenic light detectors with NL amplification:

The effect of an overall reduced drift length is especially relevant for the case of cryogenic light detectors since the photons are absorbed close to the absorber surface where the concentration of traps and defects is expected to be pronounced (see [59] and references therein). Furthermore, in the currently used field geometry, the charge carriers are drifted along the surface of the absorber.

The feasibility of using NL amplified light detectors to improve background suppression in rare event search experiments was first studied by [59, 60]. Therein, an improvement of the signal-to-noise (S/N) ratio of the light detectors signals by a factor of ~ 9 was achieved as well as an improvement in energy resolution of $\sim 10\%$ at $\sim 600\,\mathrm{eV}$. However, the reduction of the observed gain with time was identified as a limiting factor in the application of NL light detectors to rare event searches which require a stable detector response for extended periods of time. Typical measurement campaigns can last for several years. In principle, the detector can be regenerated to restore initial working conditions after a certain exposure [59, 60]. However, a device which does not show this behavior is preferable. In [61], a novel manufacturing technique for the electrodes was developed which mitigates the accumulation of charge carriers and therefore prevents a reduction of the thermal gain with time. The device investigated in [61] did not show a significant reduction of the gain during a measurement time of $\sim 2.5\,\mathrm{h}$.

2.3 Phonon-Light Technique

The so-called phonon-light technique describes an active background suppression technique in cryogenic rare event search experiments, e.g., searching for direct dark matter interactions or the $0\nu\beta\beta$ decay. This technique employs the simultaneous measurement of the heat signal in a main target crystal (operated as a cryogenic detector) as well as the detection of the corresponding scintillation light in a separate cryogenic light detector.

2.3.1 Phonon-Light Technique in Direct Dark Matter Search Experiments

The large scale application of this background suppression technique was pioneered by the direct dark matter search experiment CRESST-II [52] which employs several $CaWO_4$ crystals, each with a mass of $\sim 300\,\mathrm{g}$, operated at a temperature of $\sim 10\,\mathrm{mK}$, as target for elastic WIMP nucleon scatterings. The scintillation light signal is measured using cryogenic light detectors consisting of silicon-on-sapphire discs which are used as light absorbers.

In these $CaWO_4$ crystals, different kinds of interactions (e.g., e^-/γ-, α-, or nuclear recoil induced events) can be distinguished by the respective amount of light measured in a cryogenic light detector for each interaction. This is due to the fact that e^-/γ events interact with the electron shell of the atoms in the crystal lattice while nuclear recoils (e.g., neutron-induced events but also nuclear recoils induced by elastic WIMP scatterings) interact with the atomic nucleus. This leads to a reduced light yield of nuclear recoils compared to electronic recoils. Furthermore, the light yield of nuclear recoils in $CaWO_4$ depends on the specific nucleus of the recoil (i.e., Ca, O, or W).

In $CaWO_4$ crystals, the measured amount of light for e^-/γ induced events is $\sim \mathcal{O}(2\%)$[3] of the total amount of energy deposited within the crystal. For nuclear recoils on the individual nuclei, the amount of light is further reduced by the so-called quenching factor (QF) which is experimentally measured [81] and motivated by a theoretical description of the scintillation process in $CaWO_4$ [61]. Due to this light quenching, very sensitive cryogenic light detectors are necessary in order to measure the light signal of nuclear recoils (e.g., for a 10 keV nuclear recoil on tungsten ($QF_W \approx 0.02$), a light signal of

[3] This value is obtained using the scintillation efficiency ($\sim 6\%$) of the crystal and the light collection efficiency ($\sim 30\%$) [80].

$\sim 4\,\mathrm{eV}$ is expected). As shown in [61], cryogenic light detectors with Neganov-Luke amplification allow to further increase the sensitivity of cryogenic light detectors[4].

Figure 2.4 illustrates the setup of a detector module employing the phonon-light technique. Both the phonon and the light detector are placed inside a common detector and are housing surrounded by a highly light reflecting foil. This foil is used to increase the collection efficiency of the emitted scintillation light in the light detector. In [83, 74] is was shown that the light collection efficiency can be significantly increased by roughening the surface of the crystal as well as by optimizing the geometric shape of the crystal in order to minimize the probability for total internal reflection. Further important parameters are the scintillation efficiency and the absorption length of light in these crystals, parameters which can be optimized by annealing the crystal in an oxygen atmosphere [74]. The detector housing also acts as a heat bath for the cryogenic detectors.

2.3.2 Phonon-Light Technique in $0\nu\beta\beta$ Decay Experiments

Current generation cryogenic $0\nu\beta\beta$ experiments do not employ active background suppression techniques yet. However, the application of the phonon-light technique to this kind of experiments is planned for the next generation of experiments. Next generation $0\nu\beta\beta$ experiments using scintillating crystals in combination with the phonon-light technique are, for example, the LUCIFER experiment [46] which will operate cryogenic detectors consisting of scintillating ZnSe crystals or the LUMINEU experiment [47, 48] which is planned to operate cryogenic detectors consisting of $ZnMoO_4$ crystals.

Application of the Phonon-Light Technique to Non-Scintillating Crystals

An important challenge for next generation experiments searching for $0\nu\beta\beta$ decay with cryogenic TeO_2 bolomoters is the implementation of an active discrimination scheme in order to distinguish α-induced events (α-induced background is expected constitute the dominant background contribution

[4]For the last dark matter run of the CRESST-II, the 1σ threshold of the best cryogenic light detector can be calculated using values of [82] and [80] to be $\sim 10\,\mathrm{eV}$. The 1σ threshold of the NL light detector used within the present work amounts to $\sim 7.8\,\mathrm{eV}$ when operated with a NL voltage of $V_{NL} = 70V$(see section 5.3.1).

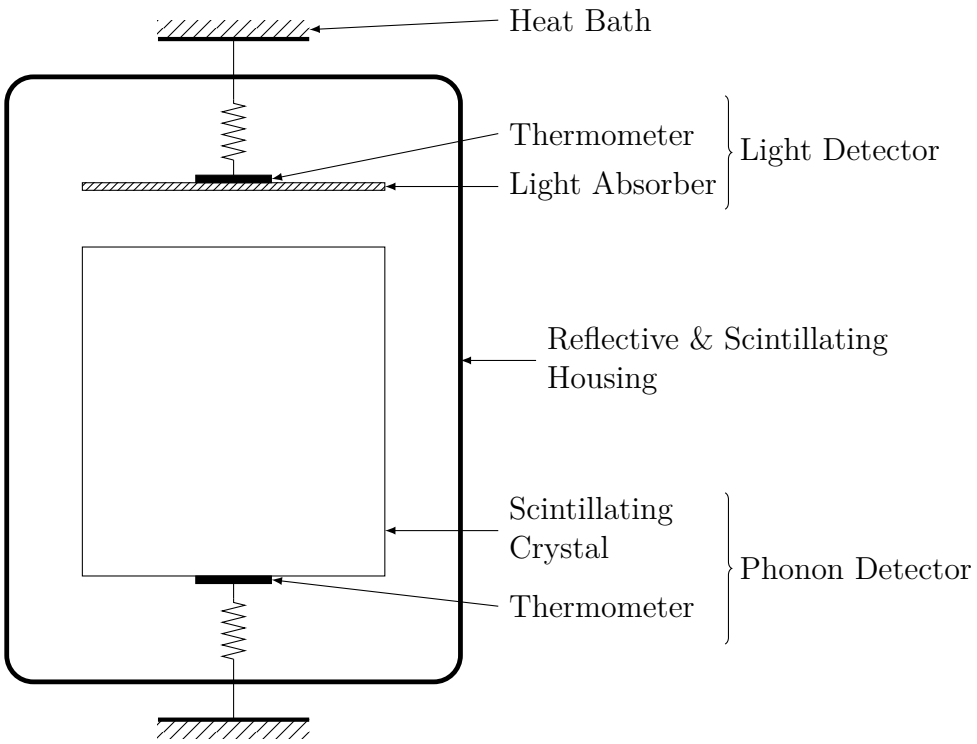

Figure 2.4: Schematic drawing of a cryogenic detector module employing the phonon-light technique. Two cryogenic detectors, a so-called "phonon detector" made out of the target material, and a light detector, are operated simultaneously to distinguish different kinds of interactions based on their respective light yield. The detectors are operated inside a reflective and, depending on the specific application, scintillating housing. The housing also acts as a support structure and thermal bath for the detectors and reflective foil is used to increase the collection efficiency of the emitted light in the light detector. The scintillating crystal confines the interaction volume for, e.g., dark matter particles or contains a $0\nu\beta\beta$-decaying isotope. The light detector typically consists of a semiconductor absorber, either silicon, germanium or silicon-on-sapphire.

in the next generation $0\nu\beta\beta$ experiment CUORE, (see, e.g., [84, 62])), from signal-like e^-/γ-events with high efficiency while at the same time retaining a high signal acceptance. Since TeO_2 crystals are non-scintillating (the entire light emission can be attributed to Cherenkov radiation [85]), the previously described approach of suppressing background events using the light yield distinct for the interaction of different particles within the scintillating crystals cannot be applied in this case.

A novel background suppression technique [54] for cryogenic detectors based on TeO_2 crystals encompasses the detection of Cherenkov radiation emitted by highly energetic electrons within the crystal using cryogenic light detectors. In this way, it is possible to distinguish the signal of the two electrons emitted in the $0\nu\beta\beta$ decay of ^{130}Te from α-induced background events. This is possible due to the fact that, in TeO_2 crystals, the energy threshold for the production of Cherenkov radiation is $E_{th}(e^-) \approx 50\,\text{keV}$ for electrons and $E_{th}(\alpha) \approx 400\,\text{MeV}$ for α particles [54]. Therefore, in the ROI around to the Q-value of ^{130}Te ($Q_{\beta\beta} = 2.53\,\text{MeV}$), no Cherenkov light is being produced for α events. This technique can, however, not be used to suppress γ-induced background events since their event signature is practically identical to the signal expected for the two electrons emitted in the $0\nu\beta\beta$ decay.

The principle viability of this technique has been demonstrated experimentally by recent measurements [86, 62]. However, an efficient event-by-event separation, which requires both, a high background suppression efficiency and a large signal acceptance simultaneously, of α- from e^-/γ-induced events could not be achieved. The measurements presented in the present work show for the first time that such an efficient event-by-event suppression is possible using Neganov-Luke amplified cryogenic light detectors to measure the Cherenkov radiation emitted from a TeO_2 crystal.

In the following, the experimental aspects relevant for the detection of Cherenkov radiation emitted from TeO_2 crystals with a cryogenic detector module based on the phonon-light technique, such as the optical properties of TeO_2 crystals as well as the optical properties of the light absorber and reflective foil, will be discussed.

2.4 Experimental Aspects of Detecting Cherenkov Radiation from TeO_2 Bolometers

When employing a background suppression scheme based on the detection of Cherenkov radiation from a TeO_2 crystal to discriminate α- from e^-/γ-induced events, the expected signal in the light channel is an important factor which determines the suppression efficiency between these events. The expected amount of light in the cryogenic light detector depends on two main factors: the amount of Cherenkov light produced by an interaction within the crystal and the light collection efficiency in the light detector (within the low-temperature detector module[5]).

In TeO_2 crystals, only electrons (induced by $\beta\beta$ events and the interaction of γ-rays within the crystal) and muons have sufficient energy to produce Cherenkov radiation. The amount of Cherenkov radiation produced in the crystal is determined by the refractive index of TeO_2 and the propagation (i.e., energy loss) of the electrons within the crystal. The collection efficiency in the light detector on the other hand is affected by the optical properties of all components which compose the optical detector module. This includes for example the TeO_2 crystal, the silicon light detector and the reflective foil used to cover the inner surface of the detector housing (see section 2.3 for a description of the phonon-light technique).

In the following, the production of Cherenkov radiation as well as the optical properties affecting the light collection efficiency will be discussed. Since the optical properties of the light absorber and light reflecting foil have yet to be measured at cryogenic temperatures, these parameters are only discussed qualitatively in order to define the relevant spectral range in which light can be detected in the cryogenic light detector.

2.4.1 Cherenkov Radiation

Charged particles, such as the two electrons emitted in the hypothetical $0\nu\beta\beta$ decay of ^{130}Te, passing through a medium with refractive index n emit Cherenkov radiation [87] if their velocity v is larger than the phase velocity of light in the medium. The light is emitted on a cone with an opening angle

[5] The light collection efficiency in the detector module can, e.g., be studied by means of a Monte-Carlo simulation (see appendix A).

θ_C relative to the particle's direction. The angle is given by [1]:

$$\cos\theta_C = \frac{1}{\beta \cdot n} \tag{2.6}$$

where $\beta = v/c$ and n is the refractive index of the medium. Cherenkov radiation is emitted if the criterium $v > c/n$ (this is equivalent to $\cos\theta_C > 0$ and $\beta > 1/n$) is fulfilled. The threshold velocity above which the emission of Cherenkov radiation is possible can be expressed as $\beta_{th} = 1/n$ and the corresponding threshold energy E_{th} for the production of Cherenkov radiation can be calculated as:

$$E_{th} = m_0(\gamma_{th} - 1)c^2 \tag{2.7}$$

where γ_{th} is the Lorentz factor corresponding to the threshold velocity ($\gamma_{th} = 1/\sqrt{1-\beta_{th}^2}$), $c = 299792\,\mathrm{km/s}$ is the vacuum speed of light [88] and m_0 is the rest mass of the charged particle passing through the medium.

The number of photons N_{ph} emitted per unit track length traveled by the particle and per unit wavelength λ of the emitted photons is given by [1]:

$$\frac{d^2N_{ph}}{dxd\lambda} = \frac{2\pi z^2\alpha}{\lambda^2} \cdot \left(1 - \frac{1}{n^2\beta^2}\right) = \frac{2\pi z^2\alpha}{\lambda^2} \cdot \sin^2\theta_C \tag{2.8}$$

where z is the particle charge and α is the electromagnetic fine-structure constant ($\alpha \approx 1/137$). Due to the $\sim 1/\lambda^2$ dependence, most of the Cherenkov radiation is emitted in the UV spectrum.

Equivalently to (2.8), the radiated energy E_{Ch} per unit track length travelled by the particle and per unit wavelength of the emitted Cherenkov photons can be expressed as as:

$$\frac{d^2E_{Ch}}{dxd\lambda} = \frac{2\pi z^2\alpha \cdot hc}{\lambda^3} \cdot \left(1 - \frac{1}{n^2\beta^2}\right) = \frac{2\pi z^2\alpha \cdot hc}{\lambda^3} \cdot \sin^2\theta_C \tag{2.9}$$

where h corresponds to Planck's constant and c corresponds to the speed of light in vacuum. If the charged particle is moving through a dispersive medium, i.e., $n = n(\lambda)$, equations (2.8) and (2.9) have to be integrated over all wavelengths for which the condition $(\beta n(\lambda)) > 1$ is fulfilled in order to obtain N_{ph} and E_{Ch}.

2.4.2 Optical Properties of TeO_2

The optical properties of TeO_2 affect the production of Cherenkov radiation (via n_{TeO_2}) as well as the light collection efficiency (via the transmittance and (internal) reflectance) in a detector module.

Transmittance of TeO_2 crystals

The transmittance of TeO_2 determines the spectral range of the emitted Cherenkov radiation which can escape the crystal and is therefore detectable in a cryogenic light detector.

Tellurium dioxide (TeO_2) crystals are transparent in the spectral range between $\sim 350\,\text{nm}$ and $\sim 5000\,\text{nm}$ [89] at room temperature. Measurements at cryogenic temperatures show that the absorption edge is shifted from $\sim 350\,\text{nm}$ to $\sim 300\,\text{nm}$ at $15\,\text{K}$ [90]. This can significantly improve the collection efficiency at cryogenic temperatures since, due to the increased transparency at cryogenic temperatures, a larger fraction of the produced Cherenkov radiation can escape the crystal.

Important parameters which have significant influence on the light collection efficiency (see also appendix A) are the absorption and scattering lengths in TeO_2 crystals. Presently, only two measurements of the absorption length in these crystals are available [85, 91] (no values for the scattering length are given) and the published values differ by a factor of ~ 2 ($\sim 38\,\text{cm}$ [85] and $\sim 80\,\text{cm}$ [91]), indicating a large uncertainty of this parameter. Unfortunately, the method used to determine the absorption length is not stated in [85, 91]. Furthermore, no measurements at cryogenic temperatures are available. Therefore it is essential to perform further systematic studies of the absorption and scattering lengths in TeO_2 crystals, both at room temperature and at cryogenic temperatures.

Refractive Index

TeO_2 crystals have a high refractive index of $n \gtrsim 2.2$, are highly birefringent ($\delta n \approx 0.1$) and show a strong dispersion. Measurements of the refractive index at room temperature have been performed between $\sim 350\,\text{nm}$ and $\sim 1000\,\text{nm}$ [92, 93]. Figure 2.5 shows the dispersion of the refractive indices of TeO_2, calculated using the parametrizations given in [92, 93].

Unfortunately, no measurements of the refractive index of TeO_2 crystals at low temperatures are available. In order to account for the increased trans-

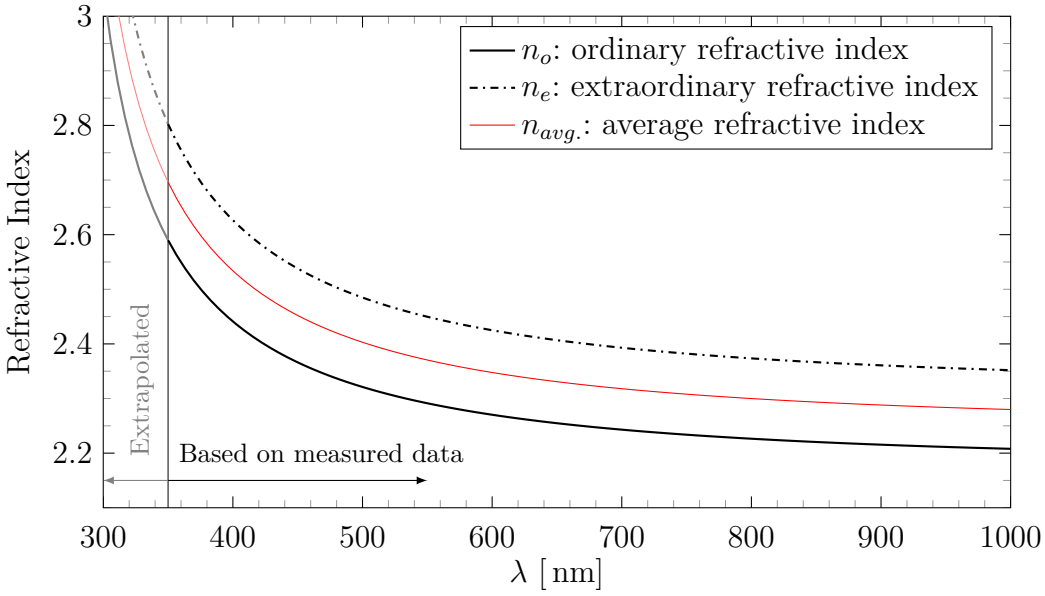

Figure 2.5: Dispersion of the ordinary and extraordinary refractive indices in TeO_2 at room temperature, calculated using the parametrization given in [92, 93]. For the simulations discussed in chapter 3, an average refractive index $n_{avg} = (n_o + n_e)/2$ is used. The values below 350 nm are extrapolated using the available parameterization to account for the increased transparence at low temperatures [90].

parency in the UV at low temperatures when determining the amount of the emitted Cherenkov radiation in the simulation described in chapter 3, the parametrization given in [92, 93] is used to extrapolate the refractive index in the spectral range between 300 nm and 350 nm.

To describe the production of Cherenkov radiation in anisotropic crystals in the simulations described in chapter 3, an average refractive index $(n_o + n_e)/2$ based on the values obtained from room temperature measurements [92, 93] is used.

2.4.3 Optical Properties of Light Reflecting Foils

As mentioned in section 2.3 the light collection efficiency in a low temperature detector module can be increased by covering the inner surface of the detector housing using a highly light-reflecting foil. An important experimental aspect is, therefore, the spectral response of this light reflector.

Figure 2.6 shows the spectral reflectivity of a 3M© VM2002 reflector foil, measured at room temperature. This reflector foil is commonly used in many particle physics experiments. Above $\sim 390\,\mathrm{nm}$, the foil shows an almost perfect specular reflectance which, however, drops to $\sim 10\%$ below 390 nm. In [74] measurements of the reflectivity at $\sim 20\,\mathrm{K}$ have been performed and while no absolute values of the reflectivity could be obtained, it was shown that the cutoff wavelength does not change at cryogenic temperatures. The reflectance at cryogenic temperatures is currently under investigation [94]. The plot furthermore shows the reflectance of one and four layers of PTFE foil (thickness $d = 0.08\,\mathrm{mm}$) as measured in [95]. Since, as mentioned previously, most of the Cherenkov radiation is emitted in the UV spectrum, a reflector with a higher reflectivity in this spectral range could significantly increase the light collection efficiency compared to the VM2002 foil.

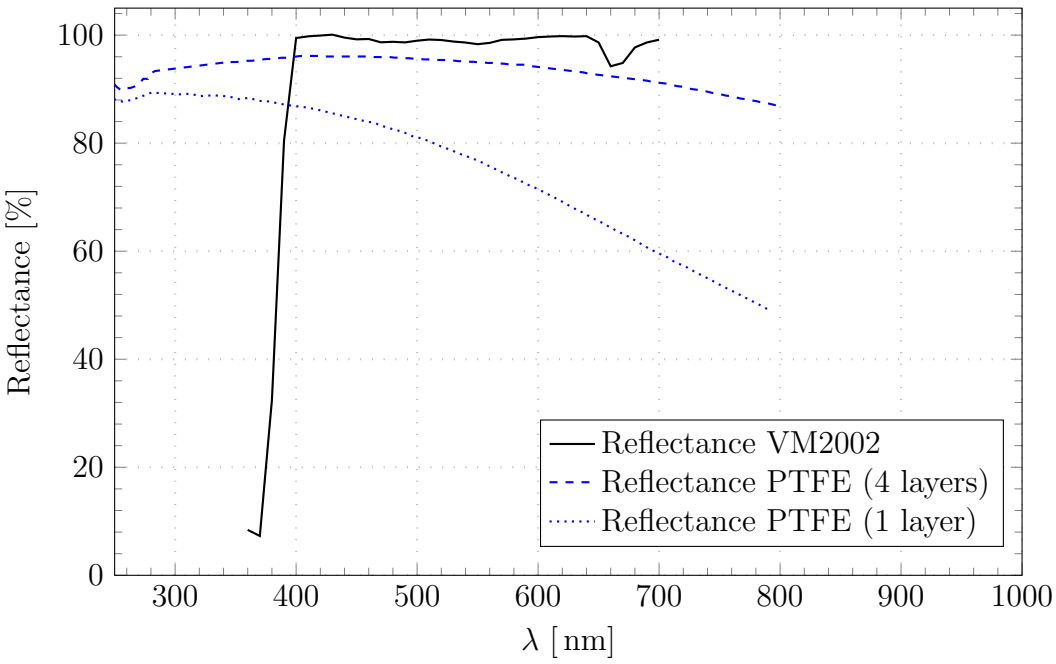

Figure 2.6: Room temperature measurements of the reflectance of the 3M© VM2002 foil (data taken from [96]) and of 1 and 4 layers of PTFE foil (data taken from [95]).

In the measurements presented in this work, the 3M© VM2002 reflector foil is used to cover the detector-facing surface of the copper detector holder (see section 5.1 for a description of the experimental setup). Future measurements

employing a reflective housing consisting of PTFE are being planned [97].

2.4.4 Absorption of Light in the Absorber Substate

The absorption probability of light in the semiconductor used as the absorber material of a cryogenic light detector also has significant influence on the light collection efficiency.

Figure 2.7 shows the optical absorption for commonly used absorber materials (value corresponds data obtained from room temperature measurements): silicon, germanium and silicon-on-sapphire. In the present work, a 0.5 mm thick silicon disc is used as light absorber. Germanium light absorbers are also commonly used in cryogenic experiments (see, e.g., [46] or [86, 62]). The absorbance of a 0.5 mm thick germanium disc is shown as a reference. In the CRESST-II experiment, silicon-on-sapphire light absorbers are used [52]. These values are included as reference.

For silicon and germanium, the absorbance can be calculated from the complex refractive index and the attenuation coefficient using data from [98] and [99] while for SOS, measured data taken from [100] is shown. The calculated values for silicon and germanium substrates show an absorption probability of $\mathcal{O}(50-70\%)$ in the spectral range from 400 nm to 1000 nm and a slightly reduced absorbance below 400 nm. In SOS substrates, due to the thin ($\sim 50\,\mu$m) silicon layer which is deposited onto the sapphire disc, the absorbance exhibits a steady cut-off above ~ 500 nm.

Silicon and germanium absorbers are especially suited for the detection of Cherenkov radiation with cryogenic light detectors since both materials show a high absorption probability in the whole spectral range relevant for this application.

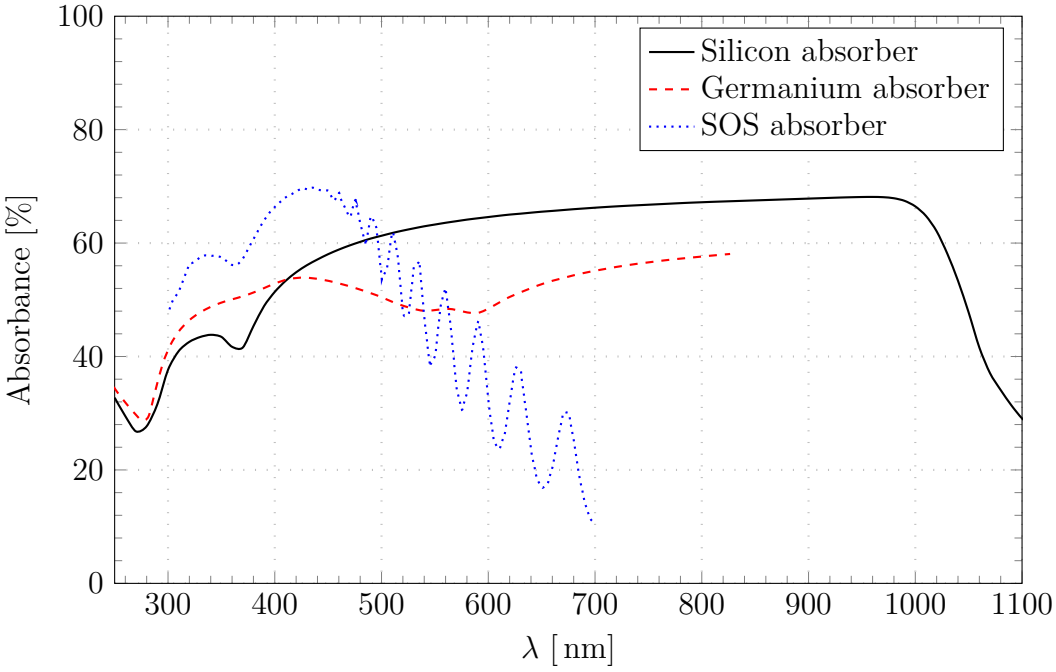

Figure 2.7: Optical absorption in a 0.5 mm thick silicon disc (calculated from [98]), a 0.5 mm thick germanium disc (calculated from [99]) and a CRESST-type silicon-on-sapphire (SOS) wafer (data taken from [100]) as a function of wavelength.

2.4.5 Calculation of the Cherenkov Yield in TeO_2

The Cherenkov yield, i.e., the total amount of emitted Cherenkov radiation (E_{Ch}) and the total number of emitted photons (N_{ph}) can be calculated using equations (2.8) and (2.9). For these calculations, the actual experimental conditions are taken into account by defining a relevant spectral range where the emitted Cherenkov radiation can actually be detected, i.e., between the high-energy cut-off of the transmittance of TeO_2 or the cut-off in reflectance of the VM2002 foil and the low-energy cut-off of the absorbance of silicon. In the following, three different setups are considered:

- $390 - 1000$ nm corresponding to the range defined by the absorbance of the silicon substrate and the reflectivity of a detector housing covered with VM2002 reflector foil.
- $350 - 1000$ nm (room temperature) & $300 - 1000$ nm (~ 15 K) corresponding to the ranges defined by the absorbance of the silicon substrate and the reflectivity of a detector housing covered with a wide-range reflector, e.g., PTFE.

For these spectral ranges, the number of produced Cherenkov photons as well as the total radiated energy is calculated using a constant refractive index $n_{TeO_2} = 2.4$. This approximation (also used in [54]) simplifies the calculation of N_{ph} and E_{ph} (eq. (2.8) and eq. (2.9)) since no dispersion and birefringence has to be considered. It is important to note that this estimate regards only the production of the Cherenkov radiation, detection and light collection efficiencies are not considered here.

Using this approximation, the threshold velocity for the production of Cherenkov radiation is given by $\beta_{th} = 0.42$ ($\gamma_{th} = 1.10$) and the corresponding threshold energy for electrons and α particles can be calculated from equation (2.7) by using the rest mass of electrons ($m_0 = 511\,\mathrm{keV}$) and α-particles ($m_0 = 3.73\,\mathrm{GeV}$), respectively:

$$\begin{aligned} E_{th} &\approx 50\,\mathrm{keV} \quad \text{for electrons} \\ E_{th} &\approx 375\,\mathrm{MeV} \quad \text{for } \alpha \text{ particles} \end{aligned}$$

As mentioned previously, given the threshold energy for α particles and the energy range relevant for $0\nu\beta\beta$-decay experiments of up to several MeV, α particles cannot emit Cherenkov radiation under these conditions.

Neglecting the energy loss of electrons, the number of emitted Cherenkov photons and the amount of Cherenkov radiation produced for electrons of energy E_{el} in a given spectral range $\lambda_{min} - \lambda_{max}$ can be calculated by integrating equations (2.8) and (2.9) (using $z = 1$ for electrons) over λ and x:

$$N_{photon}(E_{el}) = 2\pi\alpha hc \cdot \sin^2\theta_C(E_{el}) \cdot \left(\frac{1}{\lambda_{min}} - \frac{1}{\lambda_{max}}\right) \cdot d \tag{2.10}$$

and

$$E_{photon}(E_{el}) = \pi\alpha hc \cdot \sin^2\theta_C(E_{el}) \cdot \left(\frac{1}{\lambda^2_{min}} - \frac{1}{\lambda^2_{max}}\right) \cdot d \tag{2.11}$$

where d is the distance traveled by the particle.

However, since the electrons loose energy while being slowed down to rest in the crystal, the value of $\sin^2\theta_C$ changes along the track[6]. This has to be taken into account when performing the integration of (2.8) and eq. (2.9) along the

[6]The Cherenkov angle θ_C is actually a function of the distance travelled by the electron, i.e., $\theta_C(E_{el})$, where the energy loss of the electron is taken into account.

track of the electron.

Here, this calculation is performed numerically by using the stopping power of electrons in TeO_2 to calculate the energy loss along the track of the electron with an initial energy E_0 until the Cherenkov condition is no longer fulfilled. For this calculation, a step-length of $d_{step} = 10\,\mu$m is used and for each step, the Cherenkov angle $\theta_C(E_{el})$ and the corresponding amount of Cherenkov radiation produced in this step is calculated. The amount of Cherenkov radiation produced in all steps is then summed up to obtain the total amount of emitted light.

Energy Loss of Electrons in TeO_2

Electrons with kinetic energies smaller than the Q-value of ^{130}Te ($\mathcal{O}(2.5\,\text{MeV})$) loose energy primarily by ionization [1]. The stopping power for electrons in TeO_2 can be calculated using the NIST ESTAR database [101] and is shown in the top panel of figure 2.8. In the relevant energy range ($E_{el} < 2.53\,\text{MeV}$), the contribution due to radiative energy losses (Bremsstrahlung) is negligible.

The so-called CSDA range (continuous slowing down approximation range) is a close approximation of the average track length of a charged particle being slowed down to rest. It's value is obtained by integrating the reciprocal of the stopping power. The bottom panel of figure 2.8 shows the electron range in TeO_2 as a function of energy.

Cherenkov Yield

Using this method, the radiated energy in form of Cherenkov radiation can be estimated as a function of the electron's energy. The results for the spectral range from $390 - 1000\,$nm are depicted in figure 2.9 which shows the amount of Cherenkov radiation produced and the number of produced photons as a function of the electron's energy. The plot furthermore shows these parameters for a second electron with energy $Q_{\beta\beta}(^{130}\text{Te}) - E$ as well as the sum of these parameters for both electrons to illustrate the characteristics of Cherenkov radiation emitted in the $0\nu\beta\beta$ of ^{130}Te where both electrons share the energy $Q_{\beta\beta}$ released in the decay.

It can be seen from figure 2.9 that the resulting Cherenkov Yield has a non-linear energy relation, i.e., two electrons sharing an energy of $Q_{\beta\beta}$ produce less light than one electron carrying the full energy.

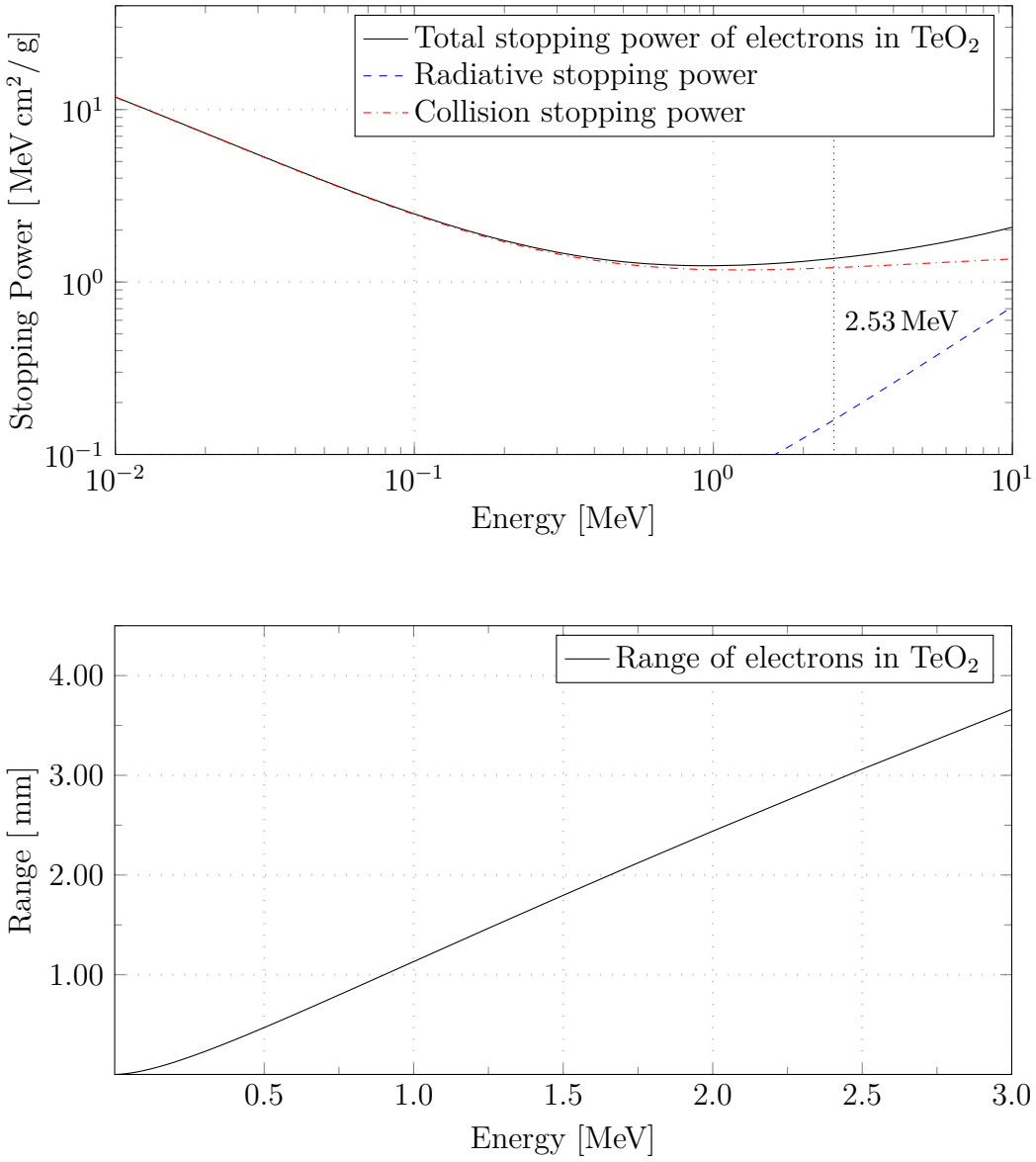

Figure 2.8: Top: Stopping power for electrons in TeO_2 (calculated using the NIST ESTAR database [101]). The vertical line marks the Q-value of ^{130}Te at 2.53 MeV. The $\beta\beta$ electrons in TeO_2 loose energy dominantly via ionization [1]. **Bottom:** Electron range (CSDA) in TeO_2 in the energy region relevant for the measurement of the $0\nu\beta\beta$ decay (Calculated using the NIST ESTAR database [101]).

Table 2.1 lists the Cherenkov Yield and number of emitted photons in dif-

ferent spectral ranges for the case that both electrons released in the $0\nu\beta\beta$ decay share the released energy ($Q_{\beta\beta}$) equally. It can be seen that by using a reflector optimized for the UV range in order to utilize the maximal possible spectral range (e.g., PTFE foil), the amount of Cherenkov radiation could be significantly increased. This could further improve the background suppression efficiency obtained in the measurements described in chapter 5.

$\lambda_{min} - \lambda_{max}$ [nm]	N_{ph}	ΣE_{Ch} [eV]
$390 - 1000$	170	375
$350 - 1000$	200	480
$300 - 1000$	255	680

Table 2.1: Overview of the number of Cherenkov photons produced by two electrons equally sharing an energy of 2.53 MeV as well as the total energy emitted in the form of Cherenkov radiation. The case $300-1000$ nm considers an increased transparency of TeO_2 at low temperatures as reported in [90]. The first line corresponds to the experimental conditions in the present work. (The calculated values have been rounded to the next multiple of 5.)

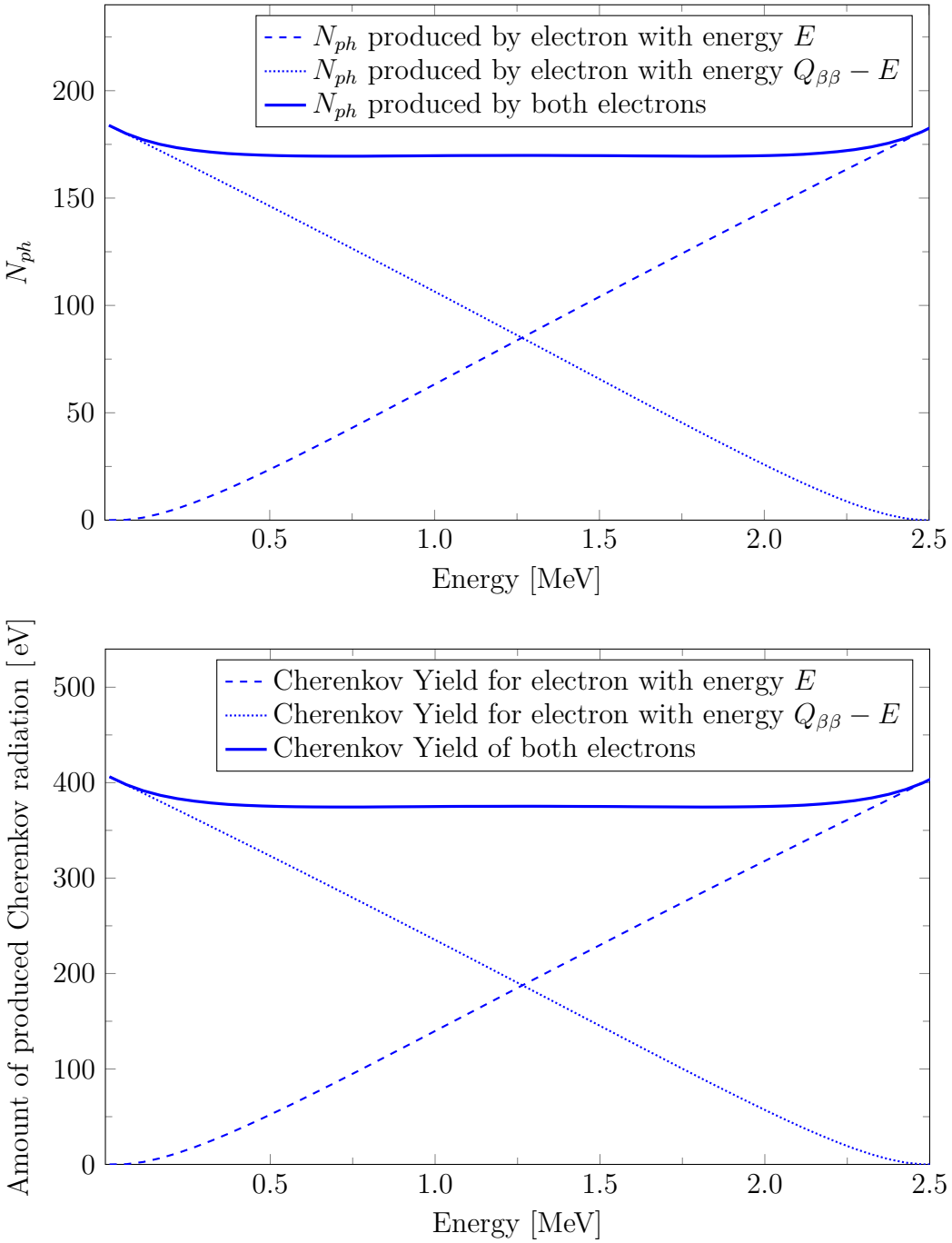

Figure 2.9: The number of Cherenkov photons produced (**top**) and the total energy emitted in Cherenkov radiation between $\lambda = 390 - 1000\,\text{nm}$. The two electrons share an energy of $E = Q_{\beta\beta}(^{130}\text{Te}) = 2.53\,\text{MeV}$ and the plots show the respective values for electrons with energy E (dashed line) and with an energy of $Q_{\beta\beta} - E$ (dotted line) as well the sum of these values (solid line).

Chapter 3

Simulation of Cherenkov Radiation in TeO_2

In the previous chapter, a novel background-suppression technique based on the detection of Cherenkov radiation emitted by high energetic electrons in non-scintillating crystals [54] was described. This technique can be used to discriminate α- from e^-/γ-induced events in experiments using TeO_2 bolometers to search for the $0\nu\beta\beta$ decay of ^{130}Te. The experimental aspects of detecting the Cherenkov radiation in a cryogenic light detector have been discussed qualitatively in section 2.4.

The amount of Cherenkov radiation produced by the two electrons emitted in this $0\nu\beta\beta$ decay was calculated via a numerical integration of the Cherenkov formula given in equation (2.9) to take the energy loss of the electrons in the crystal into account. In this calculation, however, several additional aspects are not considered. These aspects include, for example, the energy distribution of the two electrons emitted in the $0\nu\beta\beta$ decay of ^{130}Te, the dispersion of the refractive index of the TeO_2 crystal, the production of secondary electrons in the energy loss processes of the initially emitted electrons. Furthermore, the amount of Cherenkov radiation produced by electrons which are induced by γ-interactions within the crystal cannot be studied via the numerical integration of the Cherenkov equation.

In order to take these additional aspects into account, a Monte-Carlo simulation based on the GEANT4[1] simulation toolkit [102] has been performed. This simulation includes the statistical nature of the energy loss processes of the electrons in a TeO_2 crystal and the statistical nature of the production

[1] GEANT is the abbreviation for "GEometry And Tracking".

process of Cherenkov radiation.

The simulation is designed with the goal of determining the amount of Cherenkov radiation originating from the two electrons emitted in the $0\nu\beta\beta$ decay of ^{130}Te as well as the amount of Cherenkov radiation emitted by electrons which are produced in the interaction of γ rays with the TeO_2 crystal.

Studying the Cherenkov radiation produced by γ-induced events is relevant for this work since a ^{228}Th calibration source is used to investigate the detection of Cherenkov radiation in an actual low-temperature detector module consisting of a TeO_2 crystal and a cryogenic light detector. The experimental setup as well as the results of these measurements are described in chapter 5. Furthermore, this simulation is used to show that the amount of Cherenkov radiation emitted by the two electrons at the endpoint of the $\beta\beta$ decay of ^{130}Te at an energy of $Q_{\beta\beta} = 2.53\,\mathrm{MeV}$ is very similar to the amount of Cherenkov radiation emitted by γ-induced events in the full energy peak (FEP) of the $2.614\,\mathrm{MeV}$ γ line of ^{208}Tl. The results of this simulation show that the FEP to the $2.614\,\mathrm{MeV}$ γ line can be used as a proxy for the Cherenkov radiation expected for $0\nu\beta\beta$-decay events and that the background suppression efficiency at $Q_{\beta\beta}$ can be determined based on the amount of Cherenkov radiation detected for this γ line as well as for α-induced events, respectively.

An important parameter for cryogenic rare event search experiments employing the phonon-light technique is the light collection efficiency which describes the fraction of the produced Cherenkov (or scintillation) light being detected in a cryogenic light detector. In order to study the light collection efficiency, a full optical model of the detector module, which consists of the TeO_2 crystal, a silicon light absorber and the detector housing, has to be implemented in the simulation along with the optical properties of all components. Performing a reliable simulation requires knowledge of key optical parameters like the absorption length of TeO_2 crystals, which have not yet been systematically studied, the reflectivity of the reflective foil, and the reflectivity of silicon. Unfortunately, for most of these parameters only measurements at room temperature are available. Furthermore, a full tracking of all photons significantly increases the computational complexity of the simulation. However, the influence of certain parameters (crystal size, absorption length and surface roughness) on the light collection efficiency is studied in a separate simulation which is discussed in appendix A.

3.1 Introduction

The simulation is realized using version *4.9.6.p03* of the GEANT4 simulation toolkit [102]. In the following the working principle of the simulation will be discussed.

A representation of the actual experimental setup is modeled within the simulation using volumes made of the respective materials, both of which are defined in the so-called "Detector Construction". For each material basic physical parameters like the elementary composition and the density are defined. Furthermore, the optical properties (e.g., the refractive index, and absorption and scattering lengths) of the individual materials as well as the optical properties of the surfaces of the individual volumes (e.g., the reflectivity, absorption probability, and surface roughness) can be defined.

Each simulated event is initiated by randomly generating particle parameters, e.g., particle type, number of particles and their respective energy, direction and position. The particles propagate through the simulated setup until they are either absorbed in one of the simulated volumes or leave the simulated setup. The trajectory of an individual particle is referred to as "track" and while propagating through the setup the particles can undergo physical interactions like energy-loss, scattering or the creation of secondary particles which are then themselves tracked by the simulation. Each track consists of numerical intervals, referred to as "step", along which the dynamical properties of the particle (e.g., the momentum-vector and the energy-loss per unit path length) are constant. After each step, these parameters are reevaluated.

The particles as well as the physical processes considered by the simulation for each individual particle are defined within the so-called "Physics List". Using the physics list, energy thresholds for the production of secondary particles as well as parameters influencing the step-length which is used to evaluate the energy-loss of particles can be set.

Details of the simulation will be discussed in the following sections.

3.1.1 Simulated Setup

To simulate the amount of Cherenkov radiation produced by γ-induced electrons, the setup implemented in the simulation is modeled as a simplified representation of the experimental setup used for the low-temperature measurements performed in this work (refer to section 4.2 for a detailed description of the experimental setup and section 5.1 for a description of the low-temperature detector module). This allows to also simulate the interaction of γ-rays with the cryostat structure surrounding the TeO_2 crystal.

A schematic drawing of the simulated setup is shown in figure 3.1. The central component of the simulation is a TeO_2 crystal which is surrounded by a copper detector holder (compare figure 5.1), the copper cold plates, and copper heat shield of the cryostat. The simulation furthermore includes the inner vacuum chamber (IVC) and the liquid helium dewar of the cryostat, both consisting of stainless steel. The liquid helium dewar is surrounded by a $\sim 10\,\mathrm{cm}$ thick lead shielding. Due to the low expected interaction rate of γ radiation in the liquid helium surrounding the cryostat during the measurements, the liquid helium within the dewar is not implemented in this simulation.

The simulated setup is a simplified representation of the actual experimental setup. The level of detail of the simulated structures decreases with distance to the TeO_2 crystal. The most accurately modeled components are the copper detector holder and the cold plates of the cryostat. All parts apart from the TeO_2 crystal and the detector module are described by cylinders with the approximate dimensions (within several mm) of the actual components. Almost all other internal components of the cryostat are located above the copper cold plate (i.e., at a distance of at least 15 cm) and are not included in the simulated setup to reduce the computational complexity of the simulation. Figure 3.1 also indicates the position of the ^{228}Th calibration source within the setup.

The following dimensions of the TeO_2 crystal are implemented: $20 \times 20 \times 10\,\mathrm{mm}^3$, which corresponds to the crystal size used for the low-temperature measurements in this work, and $50 \times 50 \times 50\,\mathrm{mm}^3$ which is a crystal size typically used in $0\nu\beta\beta$ experiments (see, e.g., [64]).

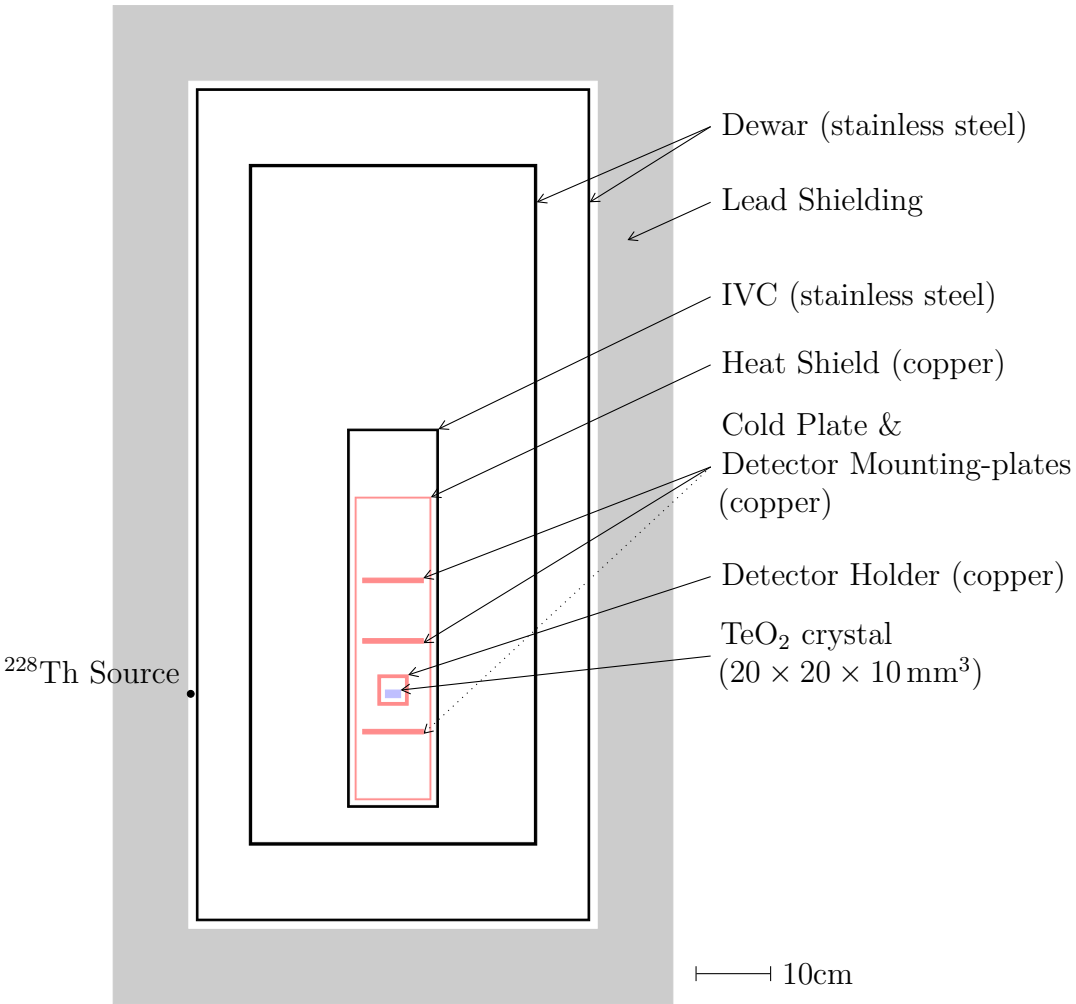

Figure 3.1: Schematic of the experimental setup implemented in the GEANT4 simulation [102]. See the main text for a detailed description.

3.1.2 Optical Properties of the TeO_2 Crystal

Within the GEANT4 toolkit, including the birefringence of materials is not possible when defining a refractive index. Therefore, an average refractive index (see section 2.4.2) is implemented for the TeO_2 crystal in the spectral range between $300 - 1000\,\text{nm}$. Since the parametrization of the refractive index is based on room-temperature measurements, the effect of a possible variation of the refractive index at cryogenic temperatures is studied by varying the refractive index[2] by $\pm 5\%$. Furthermore, the difference in the number of produced Cherenkov photons between the average refractive index and a constant refractive index $n_{const.} = 2.4$ was studied[3].

Figure 3.2 shows the spectral distribution of the number of Cherenkov photons produced per nm wavelength by the two electrons emitted in the $0\nu\beta\beta$ decay of ^{130}Te within the TeO_2 crystal (see section 3.2 for details on this simulation) for different refractive indices (i.e., the average refractive index introduced in section 2.4.2 as well as a wavelength independent, constant, refractive index).

The top panel shows the difference between the constant refractive index ($n_{const.} = 2.4$) and the average refractive index $n_{avg.}$. In the simulation performed with the constant refractive index, $\sim 2\%$ less light is emitted with respect to the average refractive index. The bottom panel shows the differences between the average refractive index and the average refractive index varied by $\pm 5\%$. In this case the integrals of the distributions differ by $\sim \pm 3\%$ with respect to the average refractive index. This leads to the conclusion that using an average refractive index is suitable to describe the amount of Cherenkov radiation emitted from the TeO_2 crystal, especially since the exact values of the refractive indices at low temperatures are not known.

[2]The ordinary and extraordinary refractive index vary by $\lesssim 5\%$ with respect to the average refractive index.

[3]The constant refractive index was used for the calculations performed in section 2.4.5.

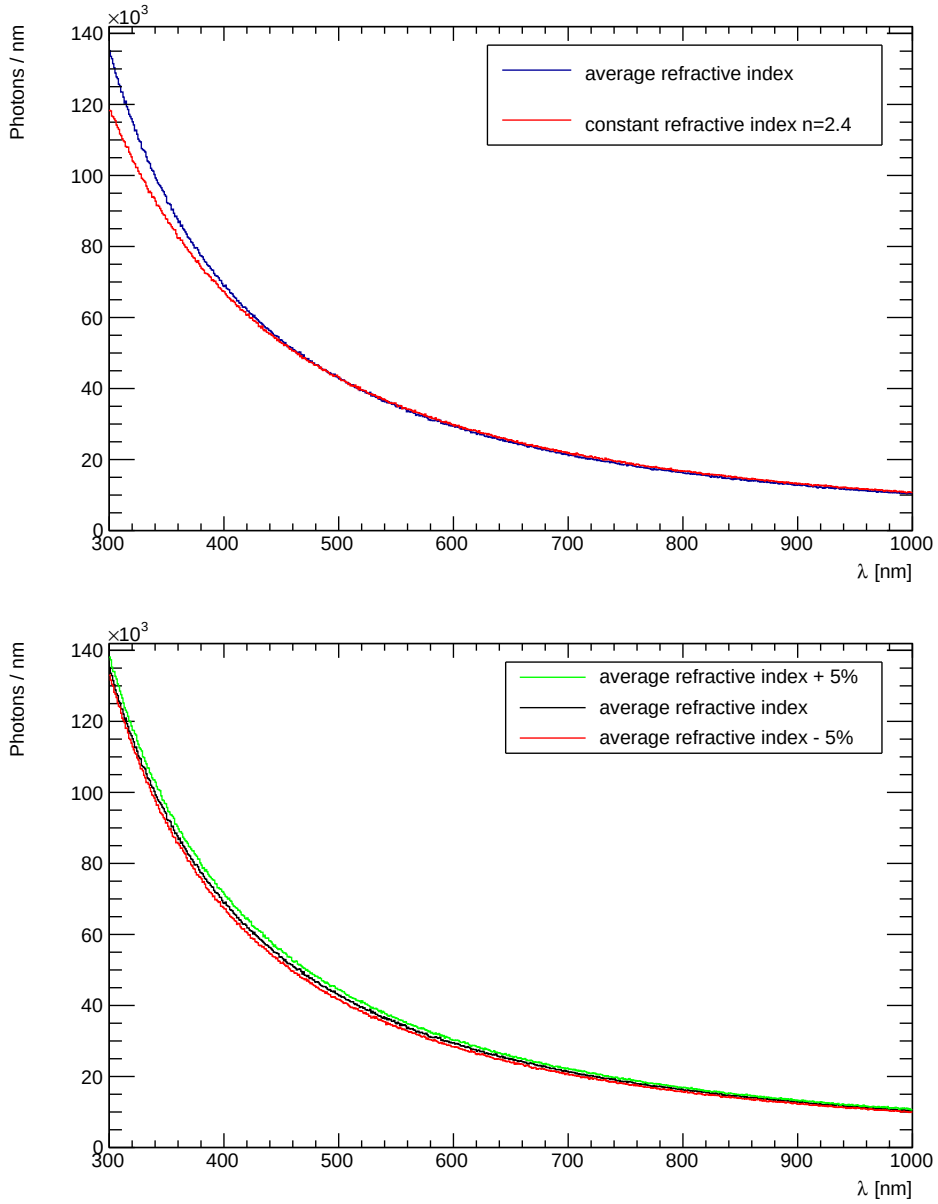

Figure 3.2: Both panels show the spectral distribution of the Cherenkov radiation produced by 10^5 $0\nu\beta\beta$ events in a TeO_2 crystal (see section 2.4.2). **Top Panel:** This plot shows the distribution for a constant ($n_{const.} = 2.4$) and average refractive index, respectively. It can be seen that the two distributions differ especially at low wavelengths where the deviation of n from the constant refractive index is pronounced. The integral of both histograms differs by $\sim$ 2%. **Bottom Panel:** In this plot, the average refractive index has been varied by $\pm$5% and the difference in the integral is $\sim \pm$3% in both cases.

3.1.3 Physics List

In the present simulation, the electromagnetic interaction of γ, e^-, and e^+ is implemented via the following physical processes:

e^-: Ionization, Bremsstrahlung, scattering, and emission of Cherenkov radiation[4].

e^+: Ionization, bremsstrahlung, scattering, e^-/e^+ annihilation, and emission of Cherenkov radiation.

γ: Photoelectric effect, Compton scattering, and pair production.

Optical photons[5] are also implemented in the present simulation. However, the propagation of optical photons is terminated after the initial step to reduce the complexity of the simulation.

Several parameters are used to adjust the characteristics of the propagation of particles and the generation of secondary particles in the tracking process of the simulation:

- The number of Cherenkov photons generated per unit step length in each numerical "step" of the simulation is calculated using the particle's properties (i.e., energy and momentum) at the beginning of the step. This number of photons is emitted continuously along the step, even if the particle is slowed down significantly during the step. In the present simulation, the maximal number of photons which can be created along the length of the step is set to one. Therefore, after the emission of one Cherenkov photon, the dynamical parameters of the particle (momentum vector and energy loss) are recalculated. This parameter therefore limits the effective step-length of electrons and positrons within the TeO_2 crystal .
- The generation of secondary particles can be limited by setting an energy threshold E_{th} below which no secondary particles are being created and tracked[6]. In GEANT4, this cut is implemented as a so-called "cut-off"

[4]Within GEANT4, emission of Cherenkov radiation is only possible in materials where a refractive index is defined.

[5]In the framework of GEANT4, a photon is called optical when its wavelength is much greater than the typical atomic spacing [102]. The handling of optical photons is detached from the handling of γ particles.

[6]In the simulation, no secondary particle are being created below this threshold. However, the corresponding energy is registered as an energy deposition within the specific volume.

length which is internally converted into the corresponding energy E_{th}. In the present work, a value of $10\,\mu$m was used for electrons, positrons and gammas. This cut corresponds to a threshold of $\sim 44\,$keV for the production of secondary electrons in TeO_2. This value is below the energy threshold for the production of Cherenkov radiation within TeO_2.

- The step length (i.e., the length of a numerical interval) of a particle is controlled by setting a "nominal" and minimal step length. The nominal step length is defined as the fraction f_{step} of the stopping length of the particle. The minimal step length is defined as an absolute step length l_{min}. In this simulation, a fraction of $f_{step} = 0.2$ and a minimal step length of $l_{min} = 100\,\mu$m is used. If the remaining track-length is smaller than the minimal step length, the particle is absorbed within the volume and the remaining energy of the particle is registered as an energy deposition within the volume.

3.1.4 Event Generation and Detection

At the beginning of each event, primary particles are injected into the simulation by one of the following event generators which have been implemented in the simulation:

- A ^{228}Th γ calibration source which is located between the lead shielding and the liquid helium dewar (see figure 3.1) is used to simulate the experimental conditions of the low-temperature measurements performed in the present work (see chapter 5). The γ rays are emitted isotropically from the source position. From the ^{228}Th decay chain, the γ-emitting isotopes ^{212}Pb, ^{212}Bi and ^{208}Tl with their respective branching ratios and line intensities are simulated. The calculation of the normalized emission probabilities is based on a simulation toolkit described in [103]. Furthermore, this event generator can be used to start the emitted γ's randomly distributed within the volume of the TeO_2 crystal.

- ^{130}Te $0\nu\beta\beta$-decay events in the TeO_2 crystal are generated by using initial conditions for the two emitted electrons (i.e., their energy and angular distributions) which are generated independently of this simulation using the DECAY4 [104] event generator[7]. A set of initial conditions ($\mathcal{O}(10^5 - 10^6)$ events) is generated with DECAY4 and then loaded into the simulation. For each event, a random entry of this set is sampled

[7] In principle, initial conditions for all other isotopes which are implemented in DECAY4 could be used as well.

and the two electrons start propagating from a random position within the crystal (the same position is used for both electrons).

In addition to these event generators, the default generators already implemented in the GEANT4 simulation toolkit can be used for the generation of events.

The initial particles then start to propagate through the simulated setup and may undergo any physical process defined in the physics list. The initial and any secondary particles which are created are tracked until they leave the setup or are absorbed[8].

For each event, the total energy deposited within the TeO_2 crystal as well as the total amount of Cherenkov radiation emitted by electrons or positrons within the TeO_2 crystal are stored[9].

The influence of different experimental conditions (like the influence of different absorber materials and reflective foils as discussed in section 2.4) is studied by defining a sensitive spectral range. This spectral range is defined by the lower (λ_{min}) and upper (λ_{max}) boundary wavelength and only photons which have a wavelength in this spectral range are registered. These parameters are chosen to reflect limitations of the spectral range which are given by the experimental conditions, i.e., the absorption cut-off of TeO_2, the cut-off in reflectivity of VM2002 or the wavelength at which silicon becomes almost transparent for the emitted Cherenkov radiation. The different spectral ranges considered in this simulation are listed in table 3.1. The spectral range between 390 nm and 1000 nm is used by default since it reflects the experimental conditions for the low-temperature measurements performed in the present work.

[8]Particles are absorbed if their remaining track length is smaller than the minimal step-length which is defined in the simulation. The particle's energy is registered as an energy deposition within the respective volume.

[9]In GEANT4, no energy conservation for optical photons is implemented. That is to say, the energy emitted via Cherenkov radiation is not subtracted from the particle's energy. However, the energy loss via Cherenkov radiation is included in the model describing energy loss of electrons and positrons.

$\lambda_{min} - \lambda_{max}$	Description
$390 - 1000$	VM2002 reflector foil and silicon light-absorber
$350 - 1000$	PTFE reflector and silicon light-absorber (The transmission cut-off of TeO_2 at room temperature is used)
$300 - 1000$	PTFE reflector and silicon light-absorber (The transmission cut-off of TeO_2 at cryogenic temperatures is used [90])

Table 3.1: Different spectral ranges used for the simulation of Cherenkov radiation in TeO_2 crystals and the corresponding experimental setups.

3.2 Cherenkov Radiation from $0\nu\beta\beta$-Events

In this section, the Cherenkov radiation produced in TeO_2 by the two electrons emitted in the $0\nu\beta\beta$ of ^{130}Te will be discussed. For this part of the simulation, a $50 \times 50 \times 50\,\mathrm{mm}^3$ TeO_2 crystal is used since a larger fraction of events deposit the full energy within crystals of this size compared to the $20 \times 20 \times 10\,\mathrm{mm}^3$ crystal which is used in the low temperature measurements in this work[10].

In a first step, the initial conditions of the two electrons emitted in the $0\nu\beta\beta$ decay of ^{130}Te (i.e., the energy and angular distributions of the electrons) are generated using DECAY4 [104], a software written to simulate the energy and angular distribution of particles emitted in radioactive decays[11]. Figure 3.3 shows the energy and angular distributions of 10^6 simulated events of the $0\nu\beta\beta$ decay of ^{130}Te.

These primary events which describe the two electrons emitted in the $0\nu\beta\beta$ decay in the GEANT4 simulation (section 3.1) are generated by:

1. Selecting a random starting point within the TeO_2 crystal.

2. Randomly selecting a sample containing the energy and directional information of the two electrons from the set of events pre-generated using DECAY4.

Figure 3.4 shows a scatter plot of the energy deposited within the TeO_2 crystal versus the amount of Cherenkov radiation emitted in each event. A total of 10^5 events have been simulated. The spectrum features a mono-energetic line at the Q-value ($Q_{\beta\beta}(^{130}\mathrm{Te}) = 2.53\,\mathrm{MeV}$) of the decay, a characteristic feature of the $0\nu\beta\beta$ decay. Furthermore, a tail towards low energies is visible. This tail consists of events where part of the energy is carried away (i.e., by electrons or bremsstrahlung photons escaping the crystal). In the simulation, $\sim 88\%$ of all events are fully contained within the TeO_2 crystal, i.e., these events fully deposit the energy released in the decay within the crystal. This corresponds to the physical detection efficiency for $0\nu\beta\beta$ events in the crystal and the value obtained here is in good agreement with the value ($87.4 \pm 1.1\,\%$)

[10] The distribution of the emitted Cherenkov radiation is identical for both crystal sizes. However, the fraction of events which fully deposit the released energy within the crystal depends on the dimensions of the crystal (see figure 3.4).

[11] For the simulation of the initial parameters used in this work, process **1** ($0\nu\beta\beta$ with neutrino mass , $0^+ - 0^+$ transition, $2n$-mechanism) implemented in [104] is used.

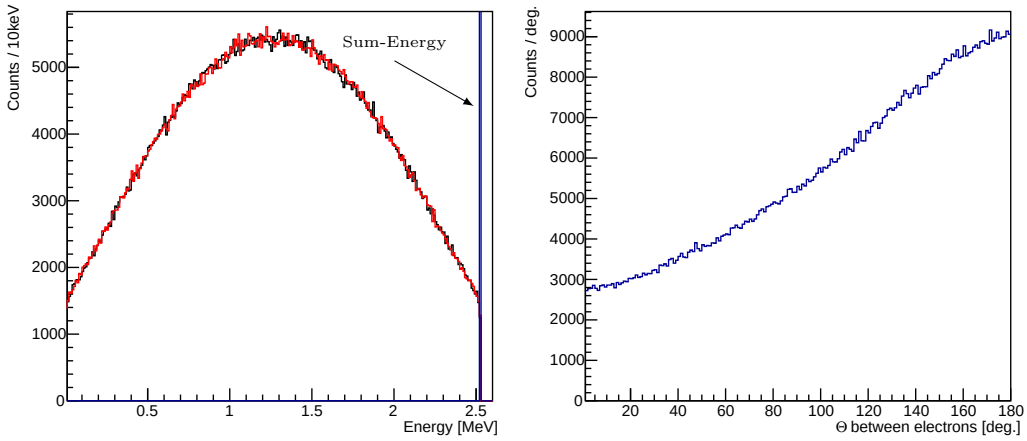

Figure 3.3: These plots show the energy (**left panel**) and angular (**right panel**) distribution of ^{130}Te $0\nu\beta\beta$ decay events simulated using DECAY4 [104]. In the left panel, the black and red curves show the individual energy distributions of the two electrons emitted in the decay and the blue curve (indicated by the arrow in the left panel) shows the sum-energy of both electrons. The sum spectrum is truncated in order to allow a better visualization of the energy distribution of the individual electrons. In the right panel, the angle between the two emitted electrons is shown.

reported by the CUORICINO collaboration for crystals with the same dimensions [105].

The histogram in figure 3.5 shows the distribution of the total amount of energy emitted as Cherenkov radiation by the events at the Q-value of the decay. The distribution is well described by a normal distribution. The width of the distribution is caused by the statistical nature of the energy-loss processes and of the production process of Cherenkov radiation. From the fit, the average amount of energy released as Cherenkov radiation is determined to be $\sim 384\,\mathrm{eV}$. The variance of the distribution is $\sigma \approx 47\,\mathrm{eV}$.

Similar simulations are performed for the other spectral ranges which are given in table 3.1. These simulations are performed for the average refractive index and for constant refractive index. The results of these simulations, summarized in table 3.2, show that the calculated values (see section 2.4.5) and the values simulated with the constant refractive index are in good agreement. A small difference between the values obtained in the simulations performed

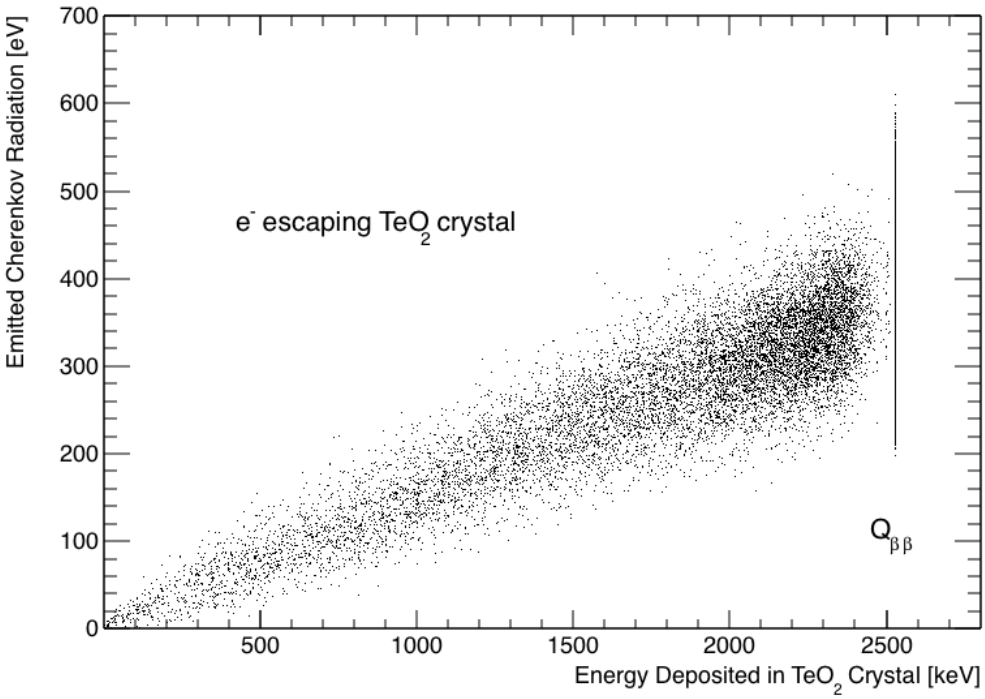

Figure 3.4: Plot of the total amount of Cherenkov radiation produced by the two electrons emitted in the $0\nu\beta\beta$ decay of ^{130}Te as a function of the energy deposited in the TeO_2 crystal. A sensitive spectral range from 390 nm to 1000 nm was used. A total of 10^5 $0\nu\beta\beta$ events have been simulated. The tail of events below the peak corresponding to the deposition of the full energy ($Q_{\beta\beta}$) is caused by part of the energy being carried away undetected, i.e., by electrons or bremsstrahlung photons escaping the crystal. In the simulation, $\sim 88\,\%$ of all events deposit the full energy within the crystal.

with the constant and the average refractive index (see section 2.4.2) is present. This difference can be explained by the slightly different spectral shapes of the emitted Cherenkov radiation (compare figure 3.2).

The values presented in table 3.2 clearly show that in order to achieve an optimal light collection efficiency for the $0\nu\beta\beta$ events, the "sensitive" spectral range has to be maximized. The experimental conditions in the low-temperature measurements performed in this work correspond to a sensitive spectral range from $390 - 1000$ nm (compare table 3.1). The sensitive spectral range could be extended into the UV spectrum by using a reflector foil with a higher reflectivity in the UV range (e.g., by using PTFE foil). If the full spectral range from 300 to 1000 nm can be utilized[12], the detectable amount of Cherenkov radiation can be increased by $\sim 85\%$.

$\lambda_{min} - \lambda_{max}$ [nm]	$E_{ph,calc}$ [eV]	$E_{ph,const.}$ [eV]	$E_{ph,avg.}$ [eV]
n	2.4	2.4	$2.3 - 3.0$
$390 - 1000$	375	384	384
$350 - 1000$	480	494	499
$300 - 1000$	680	697	721

Table 3.2: The amount of Cherenkov radiation produced in the spectral ranges given in table 3.1. The calculated values ($E_{ph,calc}$) are taken from table 2.1. The simulated values ($E_{ph,const.}$ and $E_{ph,avg.}$) are obtained by fitting a gaussian function to the histogram of the amount of Cherenkov radiation produced at $Q_{\beta\beta}$ (see figure 3.5). For the simulated values both a constant refractive index of $n_{const.} = 2.4$ and an average refractive index $n_{avg.}$ (see section 2.4.2) is used. The calculated values and the values simulated with the constant refractive index are in good agreement. The difference between the simulated values $E_{ph,const.}$ and $E_{ph,avg.}$ can be explained by the slightly different spectral shape of the emitted Cherenkov radiation (compare figure 3.2).

[12]The full spectral range can be utilized if the amount of Cherenkov radiation which can be detected in a cryogenic light detector is only limited by the absorption cut-off of TeO_2 and the cut-off of silicon at ~ 1000 nm (compare section 2.4).

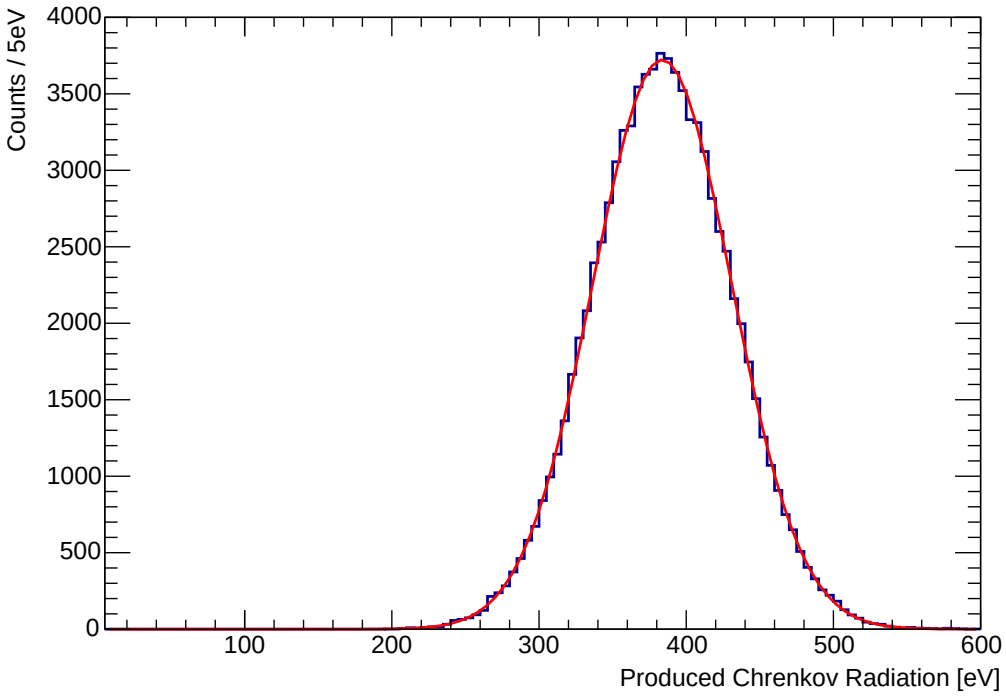

Figure 3.5: Histogram of the amount of Cherenkov radiation produced by $0\nu\beta\beta$ events which are fully contained within the crystal. The red line shows the gaussian function fitted to the histogram. The width of the distribution is due to the statistical nature of the energy-loss processes and of the production process of Cherenkov radiation.

3.3 Cherenkov Radiation from γ-Induced Events

In order to evaluate whether the suppression efficiency between α and e^- events at $Q_{\beta\beta}(^{130}\mathrm{Te})$ can be deduced from a γ calibration measurement performed with a ^{228}Th source, Monte-Carlo simulations studying the characteristics of Cherenkov radiation produced by the electrons induced by γ interactions have been performed.

Such a calibration measurement is motivated by the relatively small energy difference between the full energy peak of the 2614 keV γ line of ^{208}Tl and the energy released in the $0\nu\beta\beta$ decay of ^{130}Te ($Q_{\beta\beta}(^{130}\mathrm{Te}) = 2.53\,\mathrm{MeV}$). Therefore, both kinds of interactions are expected to result in similar amounts of produced Cherenkov radiation. This indicates that the amount of Cherenkov radiation produced by γ induced events could be used as a proxy for the amount of Cherenkov radiation expected to be produced by $0\nu\beta\beta$ events in a low-background measurement.

In the following, simulations performed for both, a relatively small $20 \times 20 \times 10\,\mathrm{mm}^3$ TeO_2 crystal, which is used for the low temperature measurements performed in this work, and for a larger $50 \times 50 \times 50\,\mathrm{mm}^3$ crystal, a size commonly used in $0\nu\beta\beta$ experiments, are discussed. The initial γs are generated using the ^{228}Th event generator described in section 3.1.4.

Figure 3.6 shows a 2 dimensional histogram of the energy emitted as Cherenkov radiation versus the total amount of energy deposited in the TeO_2 crystal for the simulated events. The most prominent features are the various γ lines which are induced by the ^{228}Th γ-source. The energies of the individual lines is given in section 5.3.2. This 2D histogram qualitatively resembles the actual measured data shown in figure 5.19 (for the simulation, energy resolution is taken into account).

In the Compton continuum corresponding to the 2.614 MeV γ line, the events are mainly induced by single Compton scattering. Events where multiple Compton scatters occur or where an additional electron is produced by the Compton-scattered electron, lead to a reduced light yield due to the non-linear energy relation of the emitted Cherenkov radiation (compare section 2.4.5).

Events involving pair production in the TeO_2 crystal lead to the generation of at least two charge carriers and therefore, the amount of Cherenkov radiation produced for these events is reduced due to the non-linear energy relation of the emitted Cherenkov radiation (compare section 2.4.5). In the

bottom panel of figure 3.6, all events produced due to pair production in the crystal are highlighted in red. The single- and double escape peak are caused by one or both of the 511 keV γ's from the e^+ annihilation escaping the crystal undetected. These events give rise to a band of events with reduced light yield. The intensity ratio between the single escape peak, the double escape peak and the full energy peak depends on the size of the crystal, i.e., a full energy deposition is more likely in a larger $50 \times 50 \times 10\,\mathrm{mm}^3$ compared to a smaller $20 \times 20 \times 10\,\mathrm{mm}^3$ crystal, due to the increased interaction volume.

The bottom panel of figure 3.7 shows a histogram of the amount of Cherenkov radiation produced by events in the full energy peak of ^{208}Tl. The shape can be explained by the top panel of this figure which shows a 2D histogram of number of the electrons produced in the crystal for each event against the amount of Cherenkov radiation emitted. It can be seen that the full energy peak is produced by events where several electrons are produced in each event. The reduction of the average amount of emitted Cherenkov radiation with increasing number of electrons produced in an event can clearly be seen.

To study the production of Cherenkov radiation by γ-induced electrons in larger crystals (such as the crystals currently employed by experiments searching $0\nu\beta\beta$ decay with TeO_2 bolometers), the simulation has also been performed with a $50 \times 50 \times 50\,\mathrm{mm}^3$ TeO_2 crystal.

Since the distribution of the amount of Cherenkov radiation produced by γ induced events in the full energy peak is independent on whether the γ's originate from outside or from inside of the crystal, this simulation was performed with ^{228}Th γ's started randomly distributed inside the crystal. This significantly reduces the computational complexity of the simulation.

The bottom panel of figure 3.8 shows a histogram of the amount of Cherenkov radiation produced by events in the full energy peak of the 2.614 MeV γ line for ^{208}Tl in this crystal size. Since the probability of multiple Compton scatters is increased due to the larger interaction volume, the average number of electrons is also increased (see top panel of 3.8). This leads to a reduction of the average amount of Cherenkov radiation emitted by the electrons. The overall characteristics of the energy distribution of the emitted Cherenkov radiation is, however, compatible with the smaller crystal (see figure 3.7).

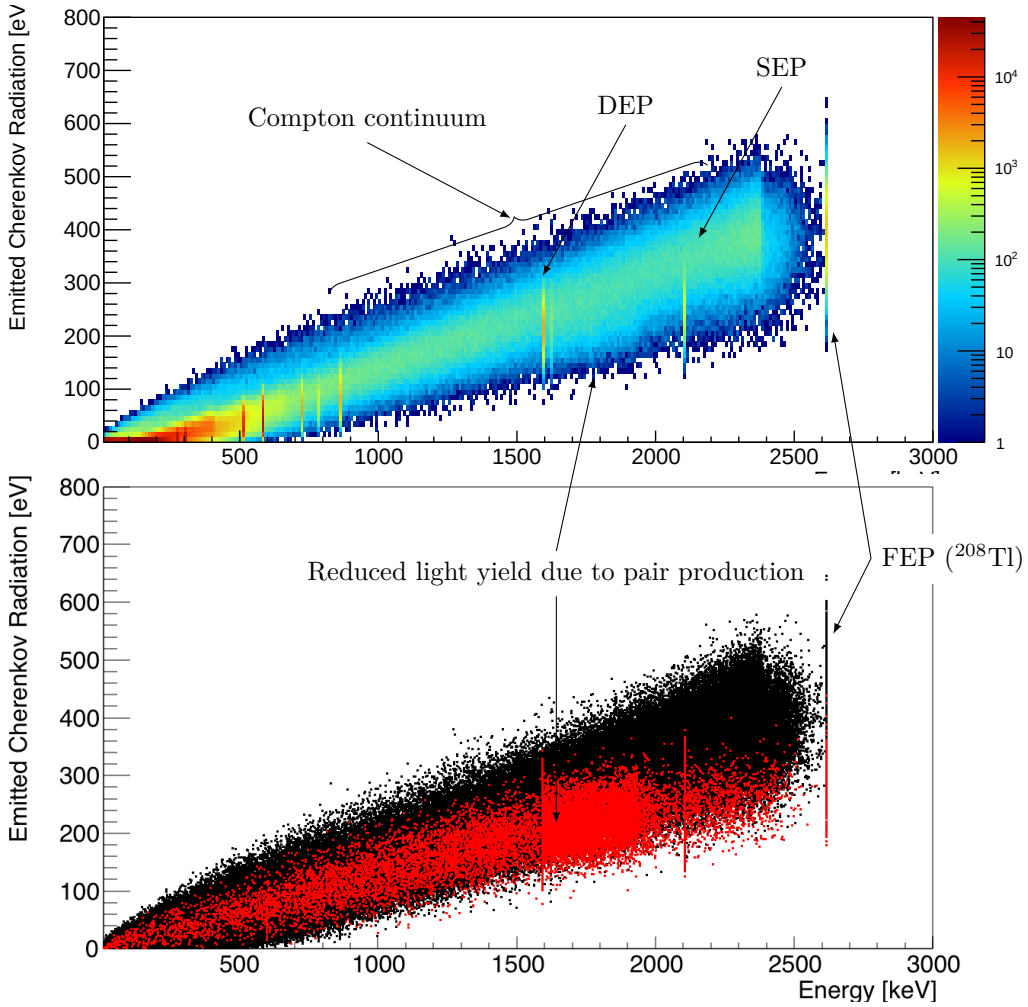

Figure 3.6: Top Panel: Density plot showing the amount of Cherenkov radiation produced vs. the energy deposited in the TeO_2 crystal with dimensions $20 \times 20 \times 10\,\mathrm{mm}^3$. For the single and double escape peak (SEP and DEP, respectively) of the 2.614 MeV γ line of ^{208}Tl (full energy peak, FEP), the amount of Cherenkov radiation is reduced compared to the Compton continuum. This is due to the fact that these lines can be attributed to events involving pair production in the TeO_2 crystal and therefore the Cherenkov radiation is generated by at least two electrons. **Bottom Panel:** A scatter plot of the simulated events. The red dots mark all events which involve pair production.

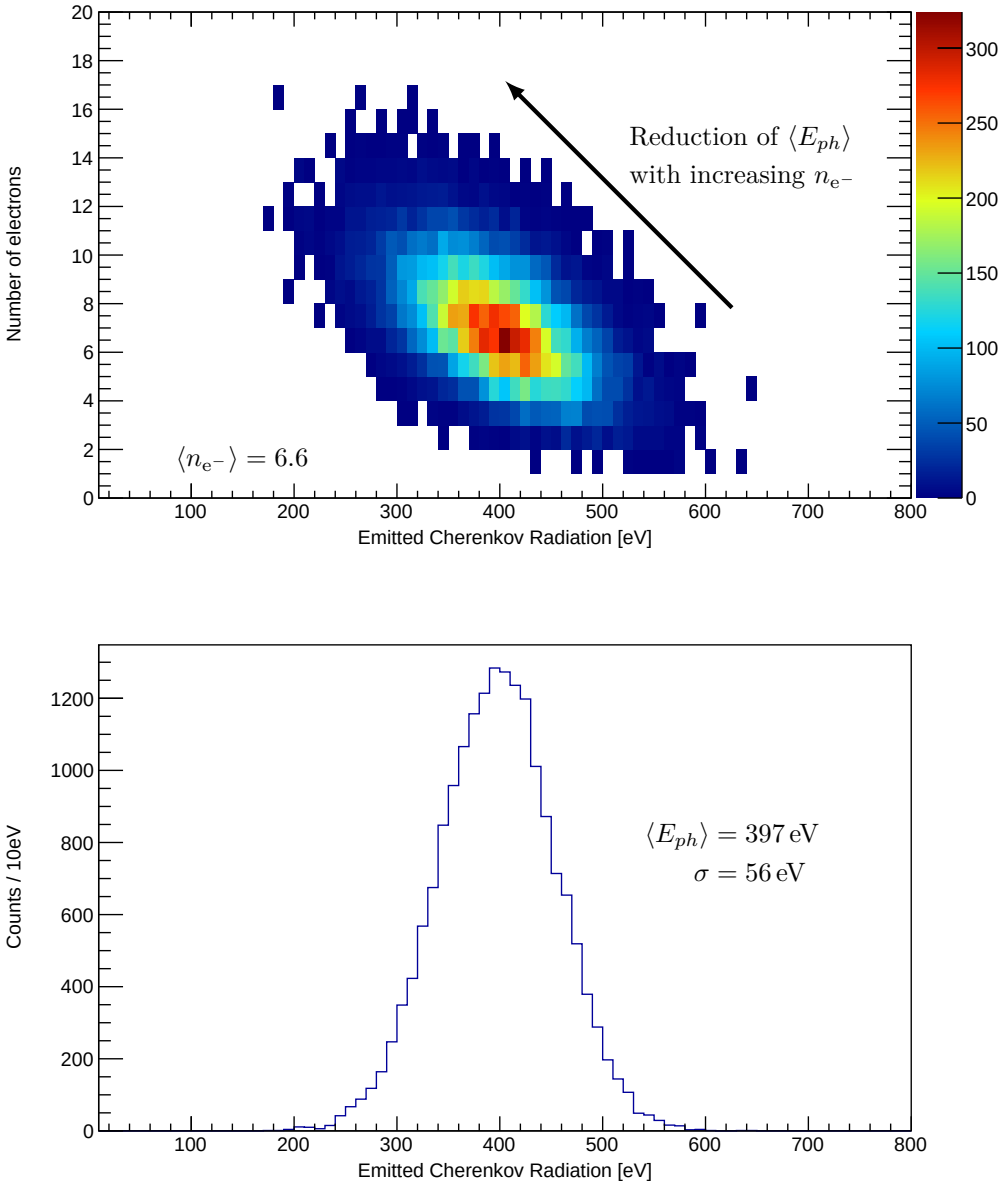

Figure 3.7: Bottom panel: Distribution of the produced Cherenkov radiation for events in the full energy peak (FEP) of the 2.614 keV γ line of ^{208}Tl for a TeO_2 crystal with dimensions $20 \times 20 \times 10\,\text{mm}^3$. An average energy of $\langle E_{ph} \rangle \approx 397\,\text{eV}$ is emitted by the electrons as Cherenkov radiation. The variance of the distribution is $\sim 56\,\text{eV}$. **Top panel:** 2D histogram of the number of electrons produced by an event in the full energy peak against the amount of emitted Cherenkov radiation. The reduction of the average amount of emitted radiation with increasing number of electrons can clearly be seen. On average, ~ 6.6 electrons above the GEANT4 production threshold ($E_{th}(TeO_2) \approx 44\,\text{keV}$ in this work) are produced per event.

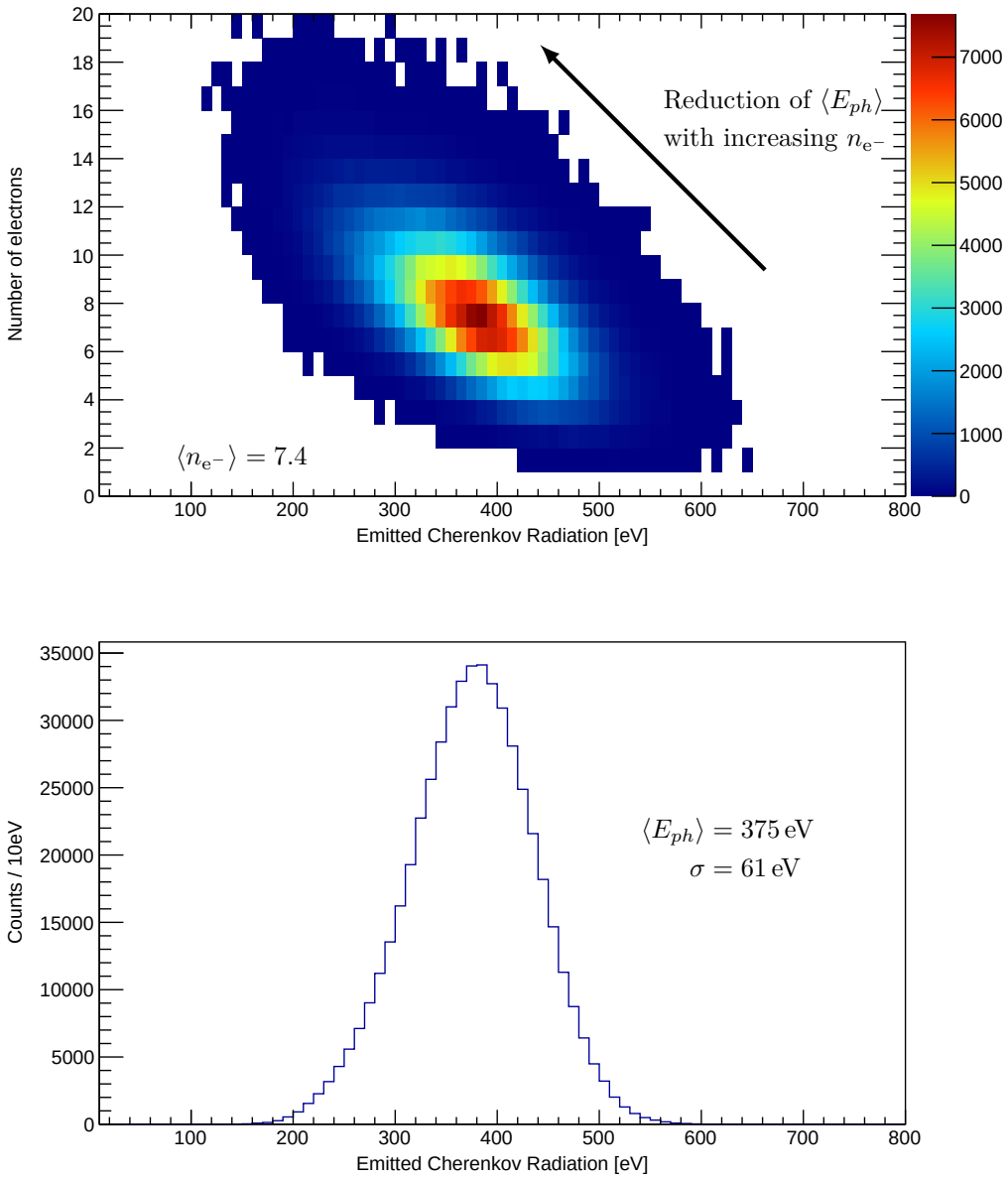

Figure 3.8: Bottom panel: Distribution of the produced Cherenkov radiation for events in the full energy peak of ^{208}Tl for a TeO_2 crystal with dimensions $50 \times 50 \times 50\,\text{mm}^3$. An average energy of $\langle E_{ph} \rangle = 375\,\text{eV}$ is emitted by the electrons via Cherenkov radiation. The variance of the distribution is $\sim 61\,\text{eV}$. **Top panel:** 2D histogram of the number of electrons produced by an event in the full energy peak against the amount of emitted Cherenkov radiation. The reduction of the average amount of emitted radiation with increasing number of electrons can be clearly seen. On average, ~ 7.4 electrons above the GEANT4 production threshold ($E_{th}(TeO_2) \approx 44\,\text{keV}$ in this work) are produced per event.

3.4 Summary

The simulations performed in the present work provides a method for determining the amount of Cherenkov radiation emitted by the electrons produced in different kinds of interactions. The amount of Cherenkov radiation can be determined within a given spectral range which is chosen based on experimental conditions, e.g., the transmission cut-off of TeO_2, the absorption cut-off of silicon, or the cut-off in reflectivity of the light-reflecting foil (*VM2002*). The values obtained from the simulation can be used to qualitatively study different experimental conditions with respect to the detectable signal. The results clearly show that by using a reflective foil with a higher reflectivity in the UV range, the amount of detectable Cherenkov radiation can be increased by a factor of ~ 2.

Figure 3.9 shows the distribution of the Cherenkov radiation produced in the full energy peak of the 2.614 MeV γ line of ^{208}Tl for the two investigated crystal sizes ($20 \times 20 \times 10\,\mathrm{mm}^3$ and $50 \times 50 \times 50\,\mathrm{mm}^3$) as well as the Cherenkov radiation produced at the Q-value of the $0\nu\beta\beta$ decay of ^{130}Te. It can be seen that the individual distributions have a very similar shape. However, due to the increased interaction volume in the larger crystal[13], a tail at lower energies is observed in this case. These results show that this full energy peak can indeed be used as an indicator for the Cherenkov radiation expected for $0\nu\beta\beta$ induced events.

In an actual experiment, the average amount of Cherenkov radiation detected with a cryogenic light detector is related to the produced amount of Cherenkov radiation via the collection efficiency[14] $\epsilon_{coll.} < 1$. The measured spectrum is therefore expected to be similar to the plot shown in figure 3.9, however, with a reduced mean of the distribution[15].

[13] This leads to an increased probability of creating secondary electrons, which, due to the non-linear energy relation of the emitted Cherenkov radiation, lower the amount of Cherenkov radiation produced.

[14] The collection efficiency can be estimated by dedicated simulations such as the simulation described in appendix A.

[15] Since α-induced events are not expected to produce Cherenkov radiation within the TeO_2 crystal, a distribution of events centered around zero is expected. The width of this distribution is given by the statistical fluctuations of the noise present in the light detector used to measure the Cherenkov radiation.

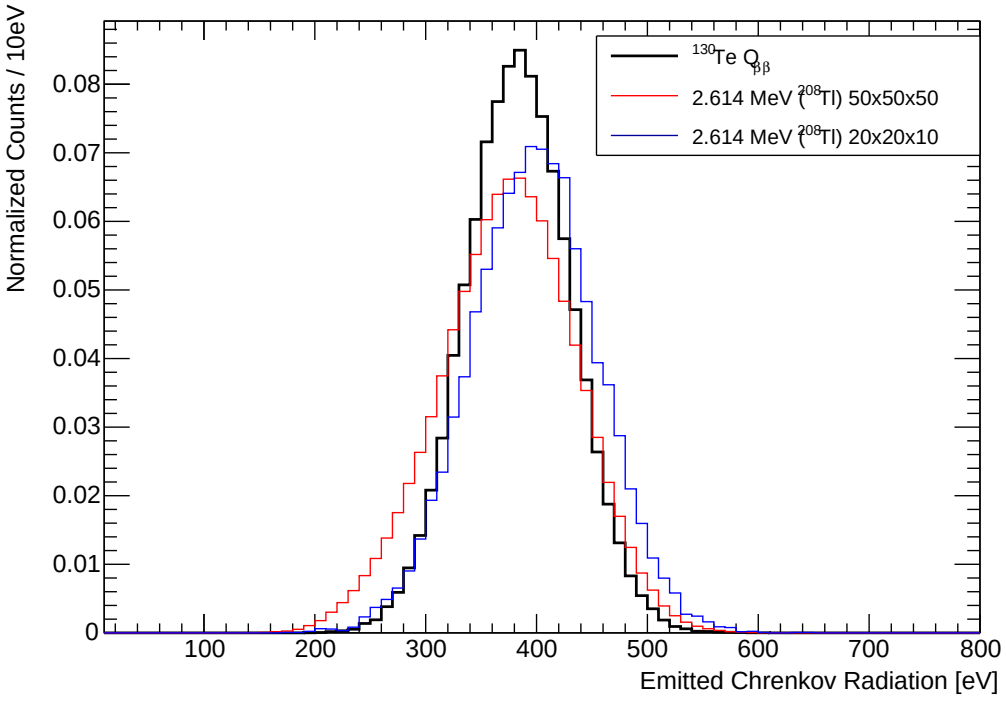

Figure 3.9: Normalized spectra of the amount of Cherenkov radiation emitted for $0\nu\beta\beta$ induced events fully contained within the crystal (black line) as well as γ induced events in the full energy peak of the 2.614 MeV γ line of ^{208}Tl for a $20 \times 20 \times 10\,\mathrm{mm}^3$ TeO_2 crystal (blue line) and a $50 \times 50 \times 50\,\mathrm{mm}^3$ TeO_2 crystal (red line). All histograms are normalized to unity. It can be seen that in the larger crystal, e^-/γ induced events produce a tail towards lower energies which is due to the increased average number of electrons produced by γ interactions in the larger interaction volume compared to the smaller crystal.

Chapter 4

Experimental Techniques

4.1 Detector Fabrication

4.1.1 Production of IrAu Transition Edge Sensors

For the transition edge sensors used in this work, superconducting IrAu thin-films were produced using a dedicated ultra high vacuum (UHV) system by means of electron beam evaporation [106, 107]. The system consists of two separate vacuum chambers, a main chamber which is used for the deposition of Ir and Au thin-films and a load-lock which is used to insert substrates into the main chamber. An overview of the system is depicted in figure 4.1. The two vacuum chambers are separated by a gate-valve and are evacuated by a turbo-molecular pump and a roughening pump each. The residual pressure in the main chamber is $\mathcal{O}(10^{-9}\,\mathrm{mbar})$ and $\mathcal{O}(10^{-6}\,\mathrm{mbar})$ in the load lock.

The main chamber is equipped with an LN_2 shield, cooled to a temperature of 77 K, which acts as an additional adsorption pump. Residual gas molecules are gettered on the cold surface, thereby reducing the pressure in the main chamber to $\mathcal{O}(10^{-10}\,\mathrm{mbar})$. The composition of the residual gas in the main chamber can be monitored using a quadrupole mass-spectrometer (Quadrex 200, Leybold). The recipient of the main chamber is equipped with heating bands on the outside which can be heated up to 180 °C. After venting the main chamber for maintenance, the recipient evacuated again and then baked-out in order to remove residual gas and water molecules adsorbed on the recipient walls. Using this procedure, a pressure of 10^{-9} mbar can be reached within ~ 24 h.

In order to keep the main chamber evacuated over the course of multiple deposition cycles, the substrates are inserted into the main chamber via the

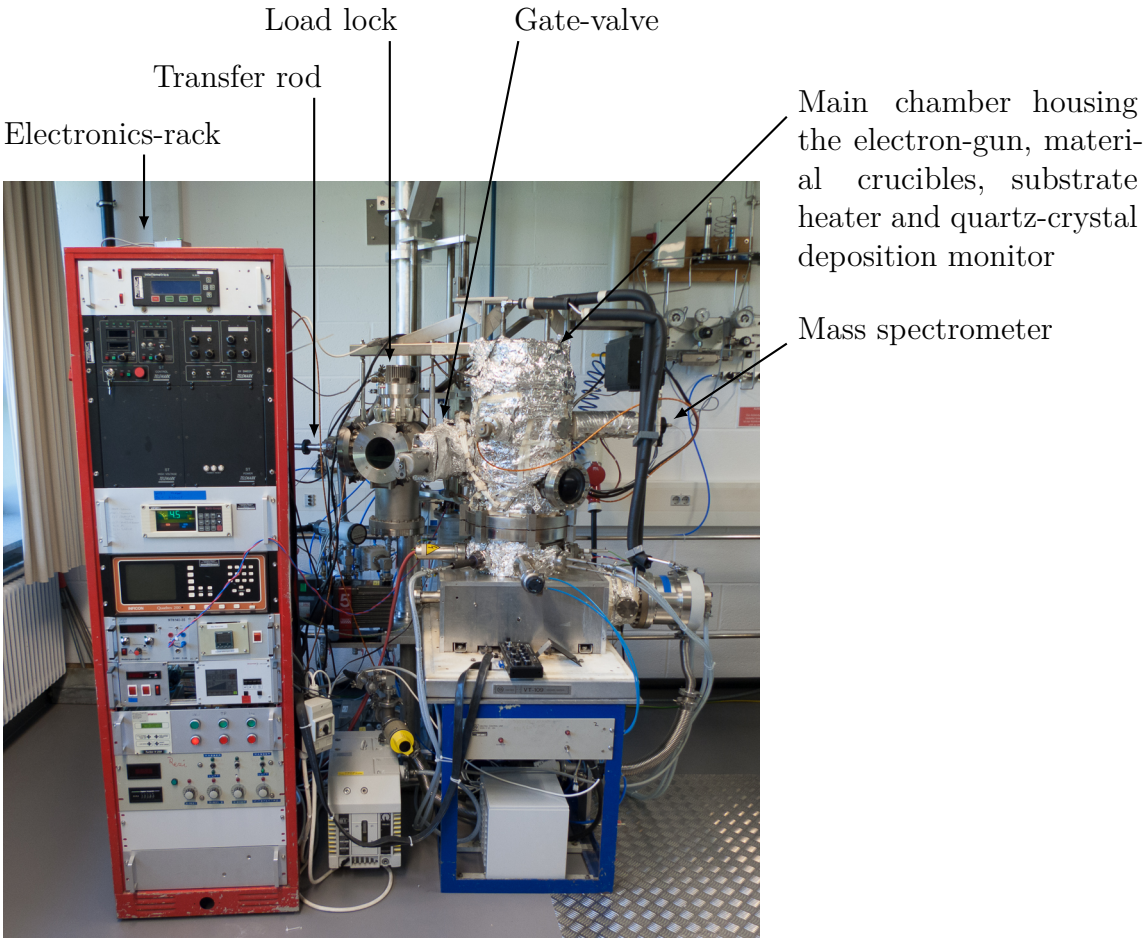

Figure 4.1: Overview of the ultra high vacuum (UHV) system dedicated to the deposition of iridium and gold thin-films. The system consists of a main chamber housing the electron-beam gun and the material crucibles and a load-lock which is used to transfer substrates into the main chamber. The load-lock and the main chamber are separated by a UHV tight gate-valve. After evacuating the load-lock, the substrates can be transferred to (and extracted from) the main chamber using a transfer-rod. Inside the main chamber, the substrates can be heated using a boron-nitride contact heater and the thickness of the deposited metal films can be monitored using a quartz-crystal deposition monitor.

load lock using a magnetic transfer rod.

For the deposition of Ir and Au thin-films, a dual-crucible electron beam gun (model 528, *Telemark*, USA) is used. The iridium is placed directly into the built-in copper crucible, while the gold is placed into a graphite crucible liner. The raw evaporation materials used are 99.999% Au (*MaTecK GmbH*, Germany) and 99.99% Ir (*Equipment Support Company*, USA,).

The thickness of the deposited thin-films is monitored using a quartz-crystal deposition monitor (model IL820, *Intellemetrics Global Ltd*, United Kingdom). The deposition monitor controls a tantalum shutter between the crucible and the substrate holder and is used to automatically terminate the deposition process once the desired film thickness is reached.

The temperature of the substrates which are being using metallized with the IrAu thin film can heated using a Boron-Nitride contact heater. The temperature of the heater is measured using a type K thermocouple and can be actively stabilized between $\sim 30\,^{\circ}\mathrm{C}$ and $500\,^{\circ}\mathrm{C}$. Stabilization is realized using a programmable process controller (model Eurotherm 3504, *Invensys Systems GmbH*, Germany) which measures the heater temperature via the thermo couple and controls the power dissipated in the heater.

The IrAu thin films used in this work consist of three layers which are produced in the following order [108]:

- A 5 nm iridium "sticking" layer is deposited onto the carrier substrate at a temperature of $300\,^{\circ}\mathrm{C}$ and a rate of $0.03\,\mathrm{nm/\,sec}$.
- A 70 nm gold layer is deposited onto the sticking layer at a temperature of $150\,^{\circ}\mathrm{C}$ using a deposition rate of $0.14\,\mathrm{nm/\,sec}$.
- A 40 nm iridium layer is deposited onto the gold layer at room-temperature ($\sim 30\,^{\circ}\mathrm{C}$) at a rate of $0.03\,\mathrm{nm/\,sec}$.
- After the deposition process is finished, the substrates are annealed at a temperature of $210\,^{\circ}\mathrm{C}$ for 2 h. This step is required to improve the steepness of the superconducting phase transition [76].

In this work, all IrAu thin films are deposited onto $5 \times 3 \times 0.5\,\mathrm{mm}^3$ silicon carrier substrates using the tantalum shadow mask [59] depicted in figure 4.2. In this way, 8 substrates can be prodced at the same time. The carrier substrates are high-purity n-type silicon substrates with a resistiviy $\rho >$

9 kΩ cm and are orientated in the <100> direction (all carrier substrates are obtained from *Crystec GmbH*, Germany).

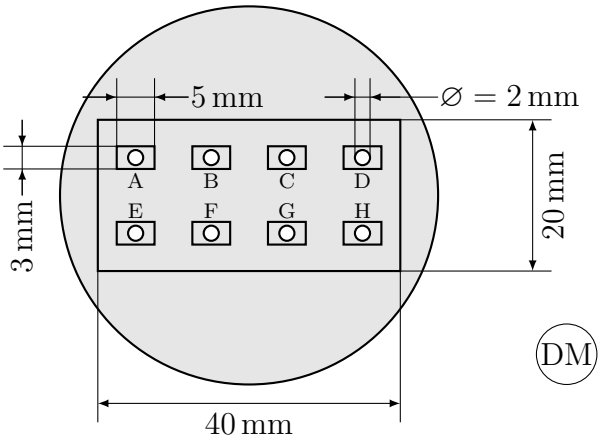

Figure 4.2: Schematic drawing of the rectangular tantalum shadow mask ($20 \times 40\,\mathrm{mm}^2$) within a round ($\varnothing = 2''$) tantalum holder [59]. This shadow mask is used for the deposition of IrAu thin-films onto $5 \times 3 \times 0.5\,\mathrm{mm}^3$ silicon carrier substrates. The letters (A to H) correspond to the relative positions of the substrates within the shadow mask. The position of the substrates relative to the quartz-crystal deposition monitor ("DM") within the main chamber is also depicted.

4.1.2 Fabrication of Aluminum Contacts

The aluminum contact electrodes necessary to apply the NL voltage to Neganov-Luke amplified cryogenic light-detectors are fabricated using a photolithographic lift-off process consisting of the following principle steps:

- Production of a photolithographic lift-off mask on top of the silicon substrate.
- Removal of the natural silicon oxide layer on the surface of the substrate and deposition of a thin aluminum film onto the silicon substrate and the lift-off mask by means of argon ion sputtering.
- Removal of the lift-off mask.
- Annealing of the aluminum contacts and the substrate.

In the following these steps are described in more detail.

Photolithographic Lift-Off Process

For the deposition of the aluminum electrodes, a photolithographic lift-off mask is used. Therefore, the silicon substrate is almost completely covered with a thin film of photoresist, only the areas where the aluminum will be deposited directly onto the substrate remain uncovered.

The production of a photolithographic lift-off mask involves the following steps:

- Cleaning of the substrate in an ultrasonic bath using (analytical grade) acetone and isopropyl alcohol.
- Application of the negative photoresist and the substrate and spinning it at 3000 rpm for 30 sec to produce a thin layer of photoresist with homogenous thickness. The photoresist used is *maN 440* (*micro resist technology GmbH*, Germany).
- Baking of the photoresist at 95°C for 6 minutes on a hot plate.
- Alignment of the photomask[1] on the substrate using a mask-aligner MA1002 (*SÜSS MicroTec AG*, Germany) and exposing the photoresist to UV light from a mercury-vapor lamp for 120 sec.
- Developing the photoresist for 50 to 60 seconds. This etches the esist everywhere it was not exposed to UV light. The developer used is *MA-D 332S* (*micro resist technology GmbH*, Germany).
- Removing any remaining developer by rinsing the substrate in ultrapure water.

Sputtered Aluminium Films

The aluminum electrodes are deposited onto the substrates using a multipurpose argon ion sputtering system (manufactured by *Veeco Instruments*, USA). A schematic representation of the system is depicted in figure 4.3. The main component of the system is the deposition chamber housing the plasma source (a DC-Kaufman plasma source [109]), a rotatable target holder (capable of holding three different sputtering targets simultaneously), the substrate holder and the deposition monitor.

[1] The photomask contains the pattern of the electrode structure which will be deposited onto the substrate. The photomask used within the present work was obtained from *ML&C GmbH* Jena, Germany.

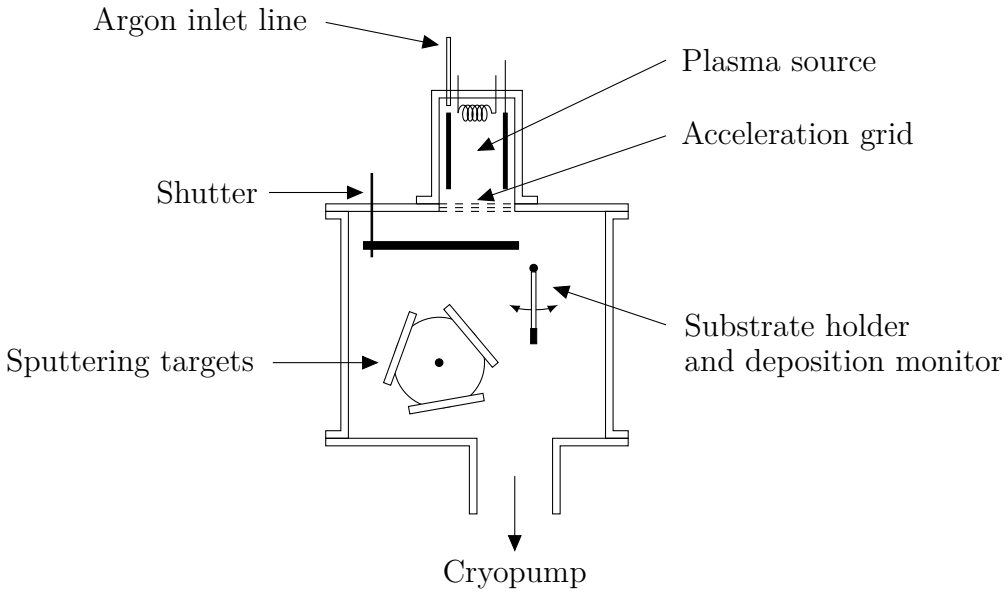

Figure 4.3: Schematic representation of the argon sputtering system used for the production of aluminum electrodes on the silicon substrates of cryogenic light-detectors with Neganov-Luke amplification. The main part of the system is the deposition chamber housing the plasma source (a DC-Kaufman plasma source [109]), the sputtering targets and the substrate holder with an attached deposition monitor. The substrate holder can be moved into the ion beam in order to expose the surface of the substrate to the Ar-ion beam. This is used to clean the substrates' surface and to remove the natural silicon oxide layer (e.g., SiO_2) at the surface of the substrate. The shutter is used to initiate and terminate the sputtering process.

The deposition chamber is evacuated using a cryo-pump and the residual pressure in the system is $\mathcal{O}(10^{-5}\,\mathrm{mbar})$. The argon plasma is produced in the Kaufman type plasma source and the argon ions are accelerated onto the sputtering target by a DC voltage applied between the source and the acceleration grid.

The sputtering process can be initiated and terminated using a shutter between the acceleration grid and the target. The thickness of the deposited thin films with a quartz crystal deposition monitor (comparable to the system installed in the IrAu deposition facility 4.1.1).

Prior to the deposition of a aluminum thin-film, the substrate is turned into the Ar-ion beam for $\sim 30\,\mathrm{sec}$. This step is performed to remove the natural silicon oxide layer and is necessary to produce a well defined metal-semiconductor interface (see [61]). Within this thesis, aluminum thin-films with a thickness of 500 nm are produced at a deposition-rate of $0.2-0.3\,\mathrm{nm/\,sec}$.

Removal of the Photolithographic Lift-Off Mask

After the aluminum deposition, the photoresist is removed in an ultrasonic bath using acetone and the substrate is again cleaned in an ultrasonic bath using acetone, isopropyl alcohol and ultra-pure water.

Annealing of Aluminum Contacts

Annealing of the silicon substrates and the deposited aluminum electrodes is performed in a high-temperature annealing furnace in a dedicated silica glass tube [61].

The annealing process consists of the following steps:

- Evacuating the glass tube using a membrane pump and flushing the glass tube with forming-gas 95/5 (a gas mixture containing 95% N_2 and 5% H_2) or ultra-pure nitrogen gas (purity 6.0). Throughout the annealing process, the glass tube is constantly flushed with the gas.
- Heating the furnace from room temperature to 400 °C with 300 °C/ h.
- Annealing the substrate at 400 °C for 30 minutes.
- Cooling the furnace back to room temperature with 300 °C/ h.

4.2 Cryostat

The cryostat used to perform the measurements with cryogenic detectors discussed in the present work is operated in the shallow underground laboratory (UGL) of the Physics Department at Technical University Munich – located in Garching, Germany – which provides a shielding of ~ 15 meter water-equivalent (m.w.e.) against cosmic ray particles. The shielding consists of at least 6 m of gravel and soil in each direction, reducing the flux of the hadronic component by $\sim 100\%$ and the flux of atmospheric muons by a factor of ~ 3 [110].

The cryostat has been used previously for low-background measurements in the framework of the solar neutrino experiment GNO [111, 112] and is therefore surrounded by a $\sim 10-15$ cm low-activity lead shielding against ambient radioactivity and an active muon veto system to identify muon induced events in cryogenic particle detectors. The cryostat, together with the shielding and the muon veto is situated in a ~ 2 m deep pit within the laboratory. Calibration sources can be inserted into the setup using an access tube located between the liquid helium dewar and the lead shielding. A schematic drawing of the setup is shown in figure 4.4. For the measurements presented in this work, the active muon veto system is not used. Details about the muon veto can be found in [111]. For the development of novel cryogenic light detectors and for the characterization of new target materials in the framework of current and future rare-event search experiments (CRESST-II [52], EURECA [58] and future experiments searching for the neutrinoless double beta decay), within the present work several new components have been installed in the setup:

- A 4-channel SQUID system (see section 4.3.2).
- Optical fibers to calibrate cryogenic light detectors using the LED calibration technique (see section 4.3.3).
- Additional wiring required for the operation of Neganov-Luke amplified light detectors (see section 4.3.3) and for a potential future operation of cryogenic detectors with NTD (Neutron Transmutation Doped germanium thermistors) readout.
- A new VME based data acquisition system (see section 4.3.4).

In the following, the operation of the ^{3}He/^{4}He refrigerator as well as the operation of cryogenic detectors will be discussed.

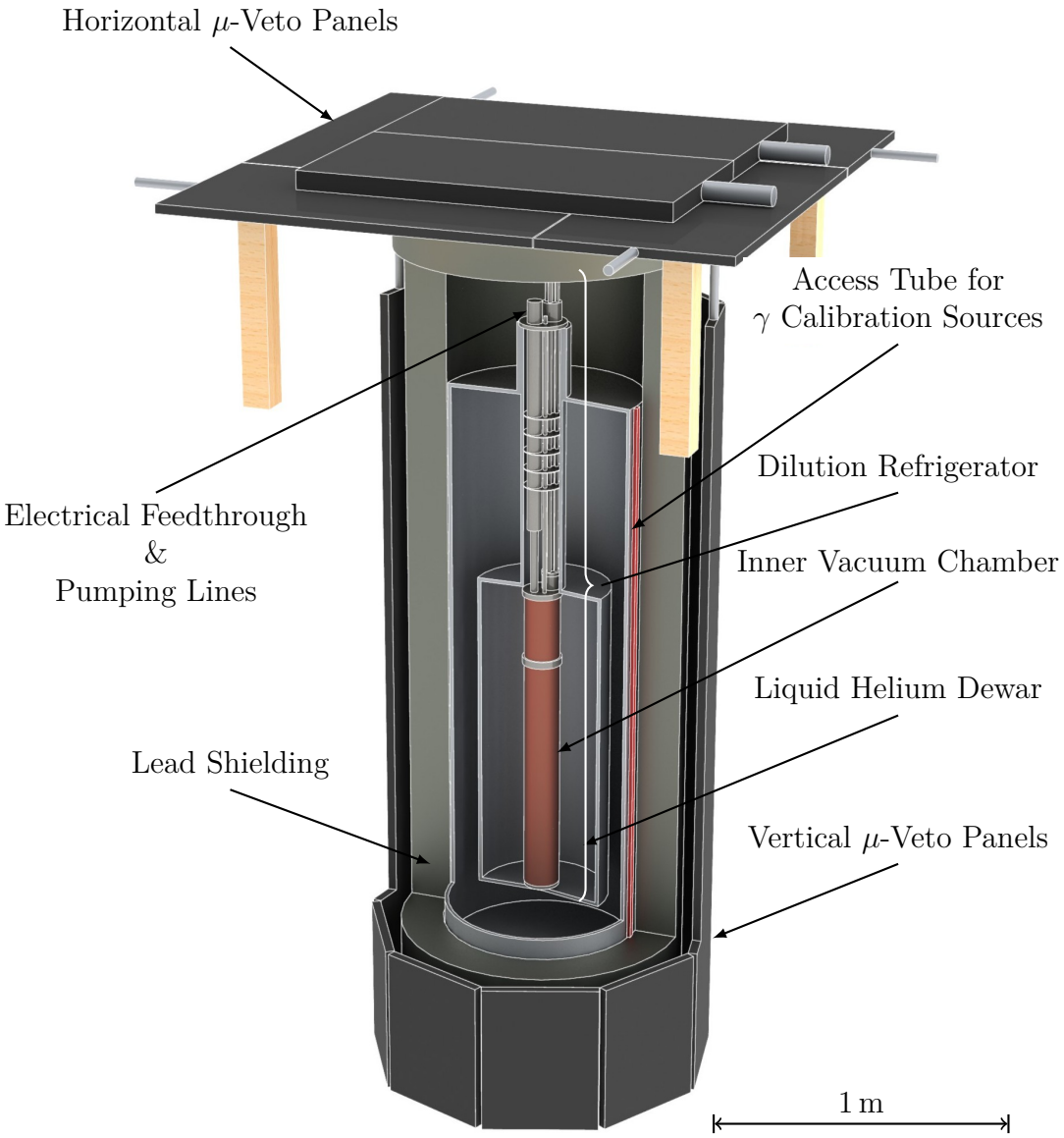

Figure 4.4: Schematic representation of the low-temperature setup operated in the shallow underground laboratory in Garching, Germany. The main component of the system is a ^{3}He/^{4}He dilution refrigerator with a base temperature of $\sim$ 12 mK. The system is also equipped with an external lead shield and an active muon veto which surrounds the sides and the top of the lead shield. The low-temperature detectors are mounted inside the inner vacuum chamber of the dilution refrigerator.

^{3}He/^{4}He Dilution Refrigerator

The low temperatures of down to $\sim 15\,\mathrm{mK}$ required for the operation of cryogenic detectors equipped with IrAu TES readout are generated by a ^{3}He/^{4}He dilution refrigerator (model *Kelvinox 100*, *Oxford Instruments plc*, UK). The refrigerator has a cooling power of $\sim 140\,\mu\mathrm{W}$ at 100 mK and with detectors installed, a base temperature of $\sim 12 - 14\,\mathrm{mK}$ is achieved on a regular basis. A detailed description of the working principle of a ^{3}He/^{4}He dilution refrigerator can be found, e.g., in [113, 114].

The system can be cooled from room temperature to the base temperature in $\sim 30\,\mathrm{h}$. The main steps of a typical cool down are:

- Evacuation of the inner vacuum chamber (IVC) to $\sim 1 \cdot 10^{-5}\,\mathrm{mbar}$.
- Filling the IVC with $\sim 1\,\mathrm{cm}^3$ of ^{4}He exchange gas and pre-cooling the cryostat to 77 K using liquid nitrogen (LN_2) filled into the dewar (see figure 4.4).
- Removal of LN_2 from the dewar.
- Filling the dewar with liquid helium (LHe) and cooling the cryostat to $\sim 4.2\,\mathrm{K}$.
- Removal of the ^{4}He exchange gas via evacuation of the IVC and a built-in adsorption pump.
- Cooling to $\sim 1.8\,\mathrm{K}$ using a ^{4}He evaporation cooler (1K pot).
- "Condensing in" of the ^{3}He/^{4}He mixture into the mixing chamber.
- Gradually initiating the circulation of the condensed-in mixture within the mixing circuit and performing the cool-down to mK temperatures.

The LHe dewar has a capacity of $\sim 60\,\mathrm{L}$ and operation of the cryostat consumes $\sim 10\,\mathrm{L}$ of liquid helium per day due to evaporation from the dewar and the 1K pot. Therefore, the LHe dewar has to be refilled every 4-5 days. In the present work, the cryostat was continuously operated for up to ~ 4 weeks.

Below the mixing chamber, the cryostat is equipped with a cylindrical experimental chamber ($\varnothing = 98\,\mathrm{mm}$, $h = 300\,\mathrm{mm}$). Detectors are thermally coupled to a copper cold-plate at the top of the experimental chamber.

Mounting of Cryogenic Detectors

A typical Neganov-Luke light detector is shown mounted inside an annealed copper holder in figure 4.5. The detector is held by Sintimid clamps which act as both thermal and electrical insulation. The holder is equipped with several copper bond pads for the electrical connection of the detector to the SQUID readout circuit and to apply the Neganov-Luke voltage. The detector is connected to the bond pads by means of ultrasonic wedge bonding using 25 μm aluminum bond wires and an additional thermal link between the TES and the copper holder is established using a 25 μm gold bond wire.

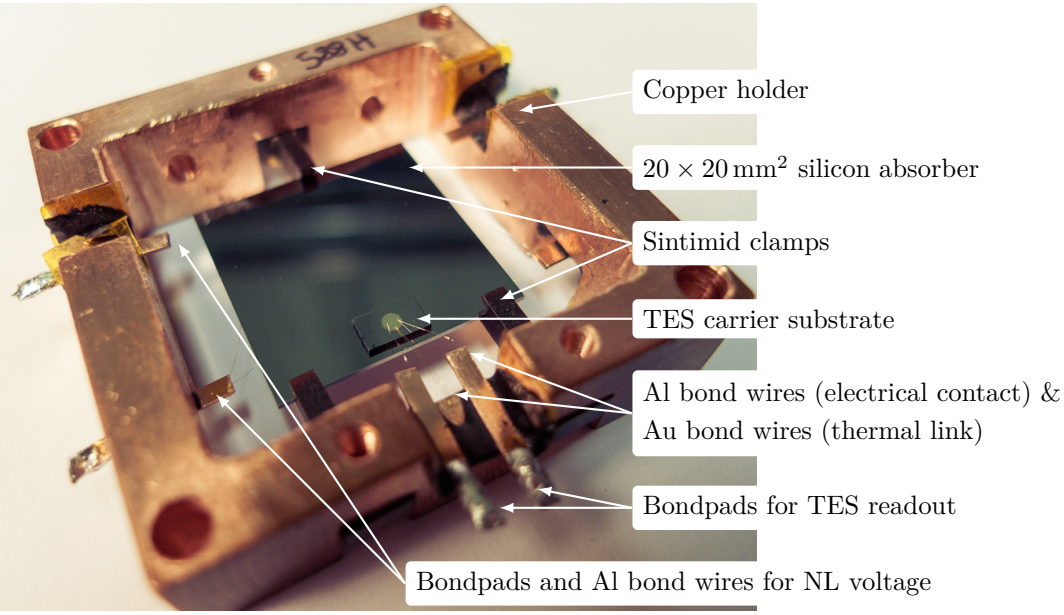

Figure 4.5: Neganov-Luke light detector mounted inside an annealed copper holder. A silicon TES carrier ($5 \times 3 \times 0.5\,\mathrm{mm}^3$) is glued onto the $20 \times 20 \times 0.5\,\mathrm{mm}^3$ silicon light absorber. The detector is held by three Sintimid clamps which act as a thermal and electrical insulation. The electrical connections for the TES readout and to apply the NL voltage are realized by 25 μm Al bond wires. The TES is thermally coupled to the copper holder via a 25 μm Au bond wire. (The aluminum electrodes on the backside of the silicon absorber are not visible).

The holder is fixed onto the cold plate using a Sintimid rod and a thermal link is provided by a copper wire of $\sim 1\,\mathrm{mm}$ diameter. To stabilize the holder at temperatures above the mixing-chamber temperature, the holder is equipped with a thermometer (typically a calibrated Speer resistance thermometer)

and a heater resistor.

The details of the temperature stabilization and the detector readout will be described in the following sections.

4.3 Measurement Electronics

4.3.1 Temperature Stabilization of Cryogenic Detectors

The temperature of the detector holder is measured using a calibrated Speer-type resistance thermometer[2]. The resistance of the thermometer is measured using a four-point resistance bridge (model AVS-47, *Picowatt*, Finnland) and the thermometers show typical resistance values in the range of $15 - 35\,\mathrm{k}\Omega$ at the base temperature of the cryostat ($T_{base} \approx 12 - 14\,\mathrm{mK}$).

The temperature can be actively stabilized at a temperature $T_{holder} > T_{base}$ by applying a dissipating heating power to a resistive heater also mounted on the detector holder. This power is regulated by a PID controller (model TS-530, *Picowatt*, Finnland) which is connected to the resistance bridge. The resistive heaters are fabricated from strain gauges with a room temperature resistance of $\sim 120\,\Omega$ (obtained from *Vishay Micro-Measurements*, USA) which are glued onto an annealed copper block using Stycast 2850FT epoxy resin. The temperature of a stabilized detector holder during $\sim$ 2 days of measurement time is shown in figure 4.6.

The cryostat is equipped with wiring for the installation of four individual thermometer/heater pairs of which two pairs can be operated simultaneously. Wiring supplied by the cryostats manufacturer is used above the 4.2 K stage of the cryostat while below this stage, the wiring is provided by superconducting NbTi twisted-pair wires in CuNi matrix (obtained from *GVL Cryoengineering GmbH*, Germany) to reduce the thermal load on the mixing chamber. At the 4.2 K stage, the thermometer signals are filtered using RC low-pass filters with a cutoff-frequency of $f_{3dB} = 80\,\mathrm{kHz}$ to prevent the pickup of high frequency electronic noise which can influence the resistance measurement. A schematic drawing of the temperature control circuit is shown in figure 4.7.

[2] All thermometers used in this work were obtained from Dr. K. Neumaier (*Walter-Meissner-Institut für Tieftemperaturforschung, Garching*).

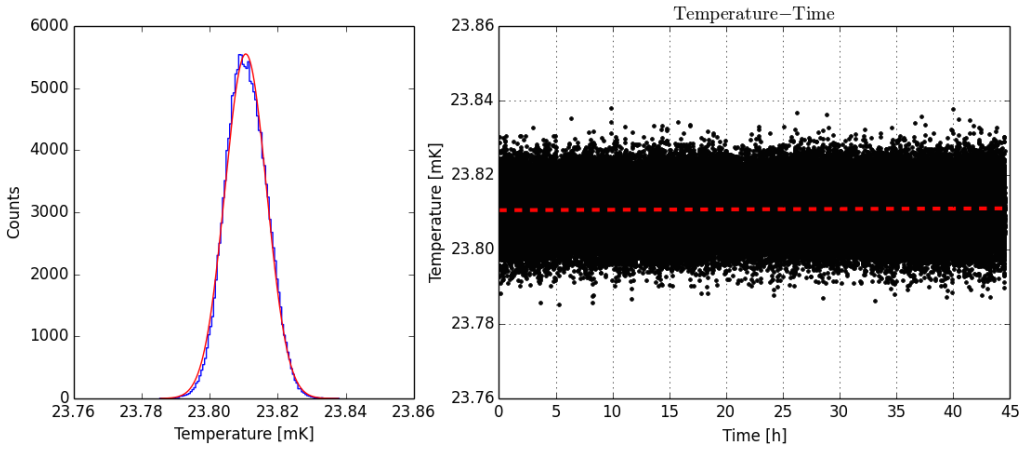

Figure 4.6: This plot shows the temperature of a low-temperature detector holder, stabilized at $\sim 23.8\,\mathrm{mK}$ over the course of $\sim 45\,\mathrm{h}$. Temperature values were sampled once every second. The left plot shows a gaussian fit to a histogram of the recorded temperatures. The average temperature is $23.81 \pm 0.01\,\mathrm{mK}$ (1σ width). The right plot shows the time dependence of the recorded temperature. A linear fit to the data shows that the temperature can be considered to be constant within $\pm 10\mu\,\mathrm{K}$ (the fitted slope is $1.1 \cdot 10^{-5}\,\mathrm{mK/\,h}$).

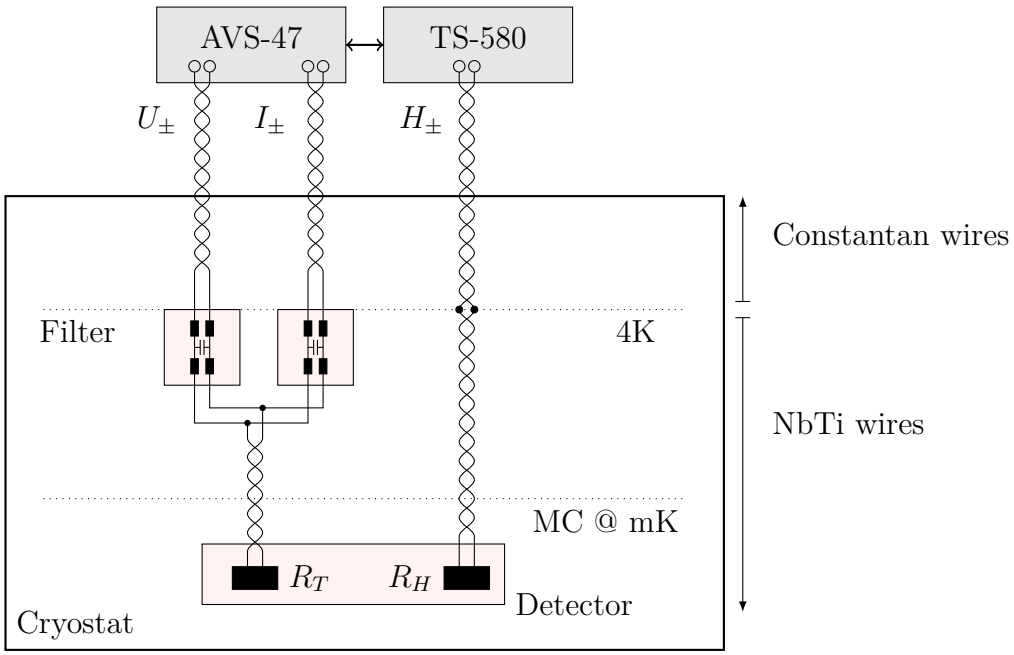

Figure 4.7: Schematic drawing of the electrical circuit used to stabilize the temperature of a detector holder at mK temperatures. The thermometer resistance R_T is read-out using a four-point resistance bridge (AVS-47). The resistance bridge is connected to a PID controller (TS-580) which controls the power dissipated in a heating resistance R_H to maintain a set resistance value.

4.3.2 SQUID System

As discussed in section 2.1, particle interactions within the absorber of a cryogenic detector rise the TES temperature and therefore induce a change in the TES resistance. This change in resistance is read-out using a matching low-impedance readout scheme based on Superconducting Quantum Interference Devices (SQUIDs). As mentioned before, within the present work the cryostat has been equipped with four independent SQUID read-out channels which allow the operation of four low-temperature detectors during one cool-down of the cryostat.

To translate these temperature induced resistance variations into an electrical signal, the TES film (characterized by R_{TES}) is connected to a readout circuit schematically depicted in figure 4.8. The electrical circuit consists of a shunt resistance R_{shunt} which is parallel to the TES film (characterized by the resistance R_{TES}) and the input coil (L_{SQ}) of a SQUID[3]. The electrical connections between the resistances and the input coil of the SQUID are made using NbTi wires which are superconducting at the temperatures used to operated the detector and the SQUID.

When a constant bias current I_{Bias} is applied to the circuit, it splits across both branches of the circuit according to Kirchhoff's law:

$$I_{TES} = I_{Bias} \cdot \frac{R_{shunt}}{R_{shunt} + R_{TES}} \tag{4.1}$$

A change in the TES film resistance therefore alters the branching ratio of the currents in the two branches of the circuit. The current change in the TES branch of the circuit induces a change of the magnetic field ($\Delta B_{\text{input coil}}$) in the input coil of the SQUID which is then translated into voltage signal.

An introduction to the working principle of SQUIDs can be found in [115, 116]. In this work, so-called dc-SQUIDS, which consist of a superconducting loop which is intersected by two Josephson junctions, are used. The shielding current I_S in the SQUID depends strongly on the flux Φ_A through the area A enclosed by the superconducting loop [115]:

$$I_S(\Phi_A) = 2I_c \sin\left(\frac{\delta_1 + \delta_2}{2}\right) \cos\left(\frac{\pi \Phi_A}{\Phi_0}\right) \tag{4.2}$$

I_c is the critical current of a Josephson junction, $\delta_{1,2}$ are the phase differences

[3]Superconducting Quantum Interference Device, a very sensitive magnetometer which can be used to translate small changes of a magnetic field into a voltage signal.

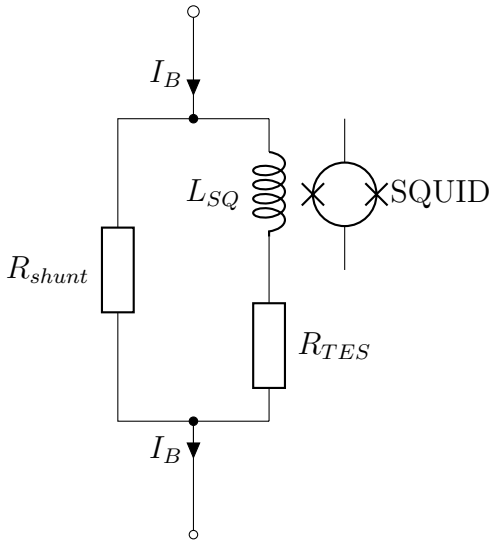

Figure 4.8: Schematic of the electrical circuit used to readout temperature changes of the TES film. A shunt resistance R_{shunt} is in parallel to the TES film resistance R_{TES} and the input coil of a dc-SQUID. The circuit is biased with a constant current I_{Bias}. Changes in the TES resistance alter the current through the TES branch of the circuit and induce a change ($\Delta B_{\text{input coil}}$) of the magnetic field in the input coil of the SQUID.

across the individual junctions, Φ_A is the flux through the superconducting loop and $\Phi_0 = \frac{h}{2e} \approx 2.0710^{-15}$ Wb is the magnetic flux quantum. The current $I_S(\Phi_A)$ shows a periodicity with Φ_0.

The SQUID is biased with a constant current I_{SQUID} which is superimposed to the screening current I_S and the corresponding voltage drop across the SQUID exhibits the same periodicity with Φ_0 as I_S. Therefore, if the voltage drop across the SQUID is measured, the magnetic flux through the superconducting SQUID loop can in imprinciple be measured very precisely. However, the SQUIDs response function is highly non-linear and therefore the SQUID is operated with an additional electronic feedback system. The employed Flux-Locked-Loop (FLL) electronics (feedback system) compensates the flux through the SQUID loop via the flux induced by an additional feedback coil ($\Phi_{Feedback}$)[4]. The feedback system linearizes the response function of the SQUID and increases its dynamic range.

When operated in FLL mode, the output of the FLL electronics is propor-

[4]The magnetic field in the feedback coil is generated by a current applied to the coil via the wire-pair $\Phi_\pm$ shown in figure 4.10.

tional to the change of the magnetic flux through the SQUID which is itself proportional to the current flowing through the input coil of the SQUID:

$$\Delta V_{SQUID} \propto \Delta \Phi_a \propto \Delta B_{\text{input coil}} \propto \Delta I_{TES}$$

A schematic representation of the SQUID readout electronics (FLL electronics) is shown in figure 4.9. Using this SQUID system, the current changes in the TES branch of the readout circuit (included by the temperature variations in the absorber) can be measured very precisely via the change in magnetic flux though the SQUID loop.

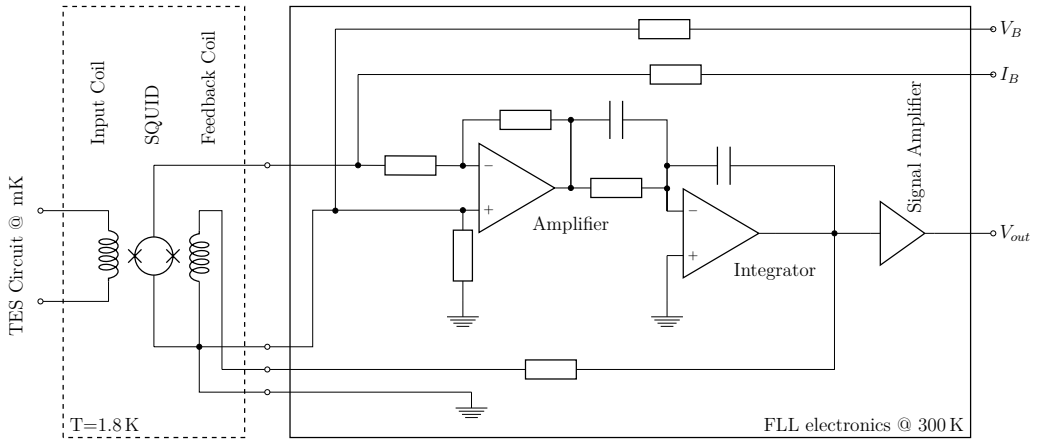

Figure 4.9: Schematic drawing of the SQUID readout electronics [117] used in this work. The electronics consists of a SQUID module mounted at the 1.8 K stage of the cryostat and a flux-locked loop (FLL) electronics module operated at room temperature. The input coil is connected to the TES readout circuit (figure 4.8). Changes in the TES resistance induce a magnetic field through the SQUID.

The SQUIDs and readout electronics used in this work were obtained from Supracon Jena[5]. The four SQUIDs (model CSblue, *Supracon* Jena, Germany) are mounted inside a superconducting niobium housing to shield external magnetic fields and are installed at the 1.8 K stage of the cryostat. The four shunt resistances[6] are mounted in copper boxes below the mixing chamber. In order to ensure a reliable cooling of the shunt resistance, it is coupled to the to copper box using epoxy resin (Stycast 2855FT). The shunt-box also

[5]formerly operating as *JeSEF - Jena Superconductive Electronics Foundry*, Germany.

[6]The the individual shunt resistors have a resistance of $R_{shunt} = 50\,\text{m}\Omega$ at room temperature.

acts as an electrical shielding for the shunt resistance. Figure 4.10 shows a schematic representation of the complete read-out system.

The wiring above the 1.8 K stage of the cryostat is provided by twisted-pair copper wires while the wiring below this stage is provided by superconducting NbTi ($T_C = 9.2\,\mathrm{K}$) twisted-pair wires (all wires are obtained from *GVL Cryoengineering GmbH*, Germany). The twisted-pair wires are additionally shielded by a CuNi mesh and all wires are thermally coupled to the 4 K, 1.8 K, 750 mK and 100 mK stage of the cryostat to reduce the thermal load on the mixing chamber.

The TES bias current (I_{bias}) is provided by a floating current source which can provide an adjustable current in the range from several nA to 10 mA. The current source is operated outside the cryostat at room temperature. To prevent the pick-up of electronic noise, the bias wires are filtered by a balanced RC low-pass filter with cut-off frequency of $f_{3\mathrm{dB}} = 30\,\mathrm{kHz}$.

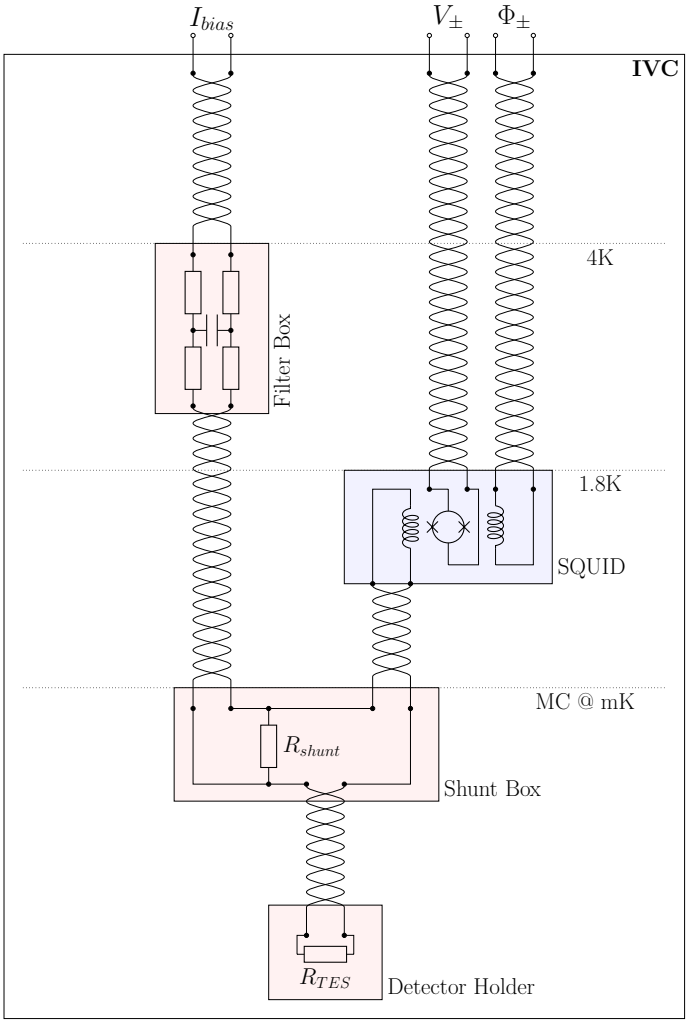

Figure 4.10: Schematic view of the detector readout installed in the ^{3}He/^{4}He cryostat. The SQUIDs are mounted at the 1.8 K stage of the cryostat and the shunt resistance is mounted below the mixing chamber at mK temperatures. The wiring from room-temperature to the 1.8K stage of the cryostat is provided by twisted-pair copper wires and below the 1.8 K stage of the cryostat, the wiring is provided by superconducting NbTi ($T_C = 9.2\,\mathrm{K}$) twisted-pair wires. All wires are thermally coupled to the 4 K, 1.8 K, 750 mK and 100 mK stage. The TES bias current is provided by a floating current source operated outside the cryostat at room temperature.

4.3.3 Operation of Neganov-Luke Light Detectors

The operation of Neganov-Luke amplified cryogenic light detectors requires additional wiring to apply the voltage between the aluminum electrodes on the silicon light absorber and an optical fiber to perform energy calibrations based on the LED calibration technique and also to regenerate NL light detectors [60].

Neganov-Luke Wiring

Three dedicated twisted-pair wires are installed in the cryostat to apply the Neganov-Luke voltage to up to three NL light detectors. The voltage required for the operation of such light detectors is generated by a single-channel floating voltage source (model *HCB 0,14-1250*, *FuG Elektronik GmbH*, Germany). The voltage source provides a voltage between 0 and $\pm 1250\,\mathrm{V}$ and a maximum current of $\pm 100\,\mu\mathrm{A}$. A balanced RC-filter at room temperature is used to prevent the pick-up of high-frequency noise. The wiring from room temperature to the 4 K-stage of the cryostat is made from shielded twisted-pair brass wires and the wiring from the 4 K to the mK-stage is made from shielded, super-conducing NbTi twisted-pair wires. Plugs at the mixing chamber are used to connect the detectors to the Neganov-Luke voltage.

LED System

For the energy calibration of cryogenic light detectors, short pulses of light generated by a light emitting diode (LED), are used. The LEDs are operated outside the cryostat at room temperature and the light is guided onto the light detector using optical fibers.

A custom made vacuum feed-through for the optical fibers, based on standard BNC connectors, depicted in figure 4.11, was constructed. The feed-through is sealed using Stycast 1266 epoxy resin (*Emerson-Cuming*) and the LED is operated inside a light-tight BNC plug. Two optical fibers ($d \approx 0.5mm$) leading from room temperature to the experimental chamber below the mixing chamber are installed in the cryostat.

For the measurements performed in this thesis, blue LEDs ($\lambda = 430\,\mathrm{nm}$, *Roithner Lasertechnik*, Austria) are used. The short light pulses used to deposit energy in the low-temperature light detector, e.g., for the energy calibration described in section 5.3.1, are generated by driving the LED with rectangular voltage pulses (typical parameters are: pulse width $\Delta t_{pulse} = 250\,\mathrm{ns}$, voltage $V_{LED} \sim 1.4 - 3\,\mathrm{V}$), generated by an arbitrary waveform generator (model

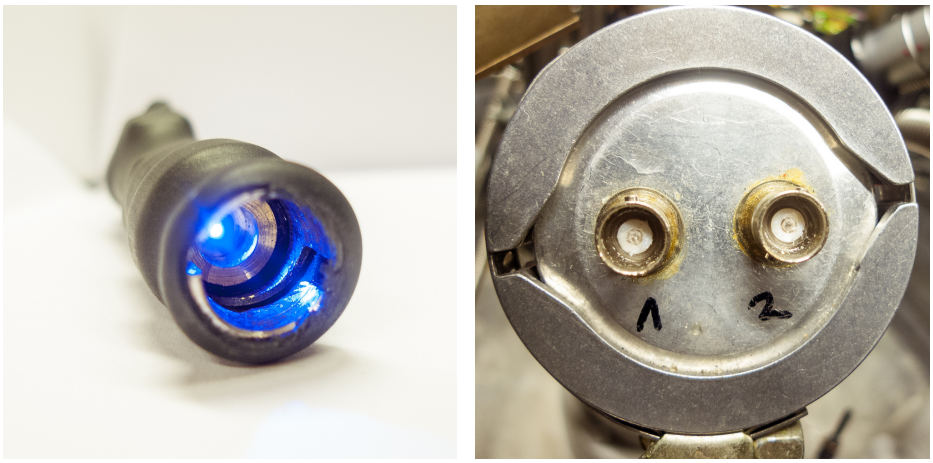

Figure 4.11: Image of the custom-made LED housing (left) and vacuum feed-through for the optical fibers (right). Then the feed-trough is sealed using Stycast 1266 epoxy resin.

HMF2525, HAMEG Instruments). These parameters lead to an instantaneous (within the time resolution of typical low temperature light detectors) energy deposition in the light detector. The arbitrary waveform generator can be controlled via a serial computer interface. All parameters of the waveform generator can be set via this interface. This allows to automatically set different LED intensities for the calibration of the light detector.

4.3.4 Data Acquisition System

The data acquisition (DAQ) system is based on the VME (Versa Module Europa) bus architecture. The system is based on the DAQ systems developed in [118] and the readout software is being developed in [119, 120].

The DAQ system consists of the following components:

- An 8 channel 16 bit FADC (flash analogue to digital converter) module (model SIS3302, *Struck GmbH*, Germany) with a sampling rate of up to 100MS/s (million samples per second) and a resolution of 16 bits each. Six channels with an input range of 0 to 20 V are used to record data from cryogenic detectors and two channels with an input range of 0 to 3 V are dedicated to the readout of the AVS47 resistance bridges described in section 4.3.1. A DC-offset can be superimposed on the signal via a built-in DAC (digital to analogue converter).

- A VME controller module (model *V2718*, *CAEN S.p.A.*, Italy).
- A VME crate housing the FADC and VME controller modules.
- A DAQ PC used to read-out the digitized data from the FADC module. In order to prevent an electrical connection between the DAQ PC and the VME system, the PC is equipped with an A2818 optical link card. This allows communication between the PC and the VME controller via an optical link based on the CONET protocol.

A schematic representation of the VME DAQ system is depicted in figure 4.12. The input range of each channel of the FADC module can be shifted individually by adding a DC voltage to the input signal using a 16 bit DAC (digital to analogue converter). Since the SQUID electronics (see section 4.3.2) are not designed to operate with voltage added to the signal, additional impedance matching amplifiers (operational amplifiers with a constant gain of unity) are used to separate the FADC input from the output of the SQUID electronics.

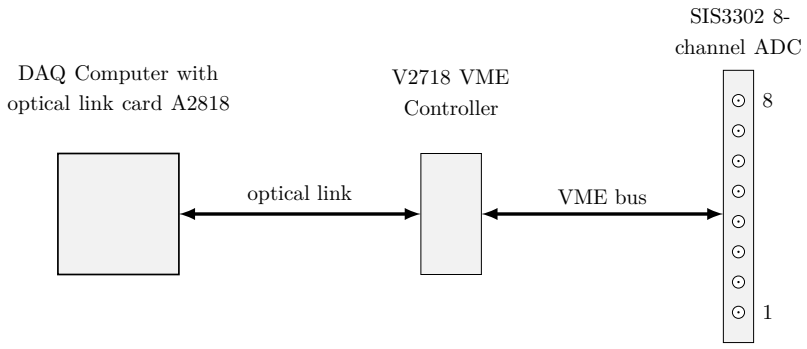

Figure 4.12: Schematic representation of the VME data acquisition system used for the measurements performed in this work. The data is digitized using a 8 channel FADC module (Struck SIS3302) with an input range of 0 to 20 V (and 0 to 3 V on the channels dedicated to the readout of the four-point resistance bridges) with 16 bits resolution and a sampling rate of up to 100MS/s each. The digitized signal is read-out via a VME controller module (CAEN V2718) by a dedicated DAQ PC equipped with an optical link card (CAEN A2818). The VME controller communicates with the ADC module via the VME bus and with the DAQ PC via an optical link.

Acquisition of Superconducting Phase Transitions

The DAQ system can be used to record the superconducting-to-normal phase transitions of IrAu TES films. To perform an accurate measurement, the TES

temperature has to be swept slowly ($\sim 10-20\,\mathrm{mK/h}$) through the transition region while constantly measuring the corresponding film resistance:

- The film resistance can be determined by applying a sinusoidal[7] bias current with a peak-to-peak amplitude ΔI_{Bias} (typically $1\ldots10\,\mu\mathrm{A}$) to the TES readout circuit (figure 4.8) and recording the corresponding SQUID response. By fitting the SQUID response with a sinusoidal function, the peak-to-peak amplitude ΔV_{SQUID} of the SQUID signal can be determined. Using the known values for the SQUID amplification A_{SQUID} ($[A_{SQUID}]= {}^{V}/_{A}$) and the resistance of the installed shunt R_{Shunt}, the corresponding film resistance R_{TES} can be calculated from the SQUID signal:

$$R_{TES} = R_{Shunt} \cdot \left(\frac{\Delta I_{Bias} \cdot A_{SQUID}}{\Delta V_{SQUID}} - 1 \right)$$

- To sweep through the transition region, the PID heater controller (section 4.3.1) can be controlled by the DAQ PC using a GPIB[8] interface. The AVS47 resistance bridge provides a voltage signal which is proportional to the measured resistance of the thermometer mounted on the detector holder. This signal is then digitized using one of the dedicated ADC channels with reduced input range. Using the calibration function of the resistance thermometer, the corresponding temperature can be calculated.

Typical transition curves are depicted in section 5.3.

Acquisition of Detector Events

The SQUID signals from a cryogenic detector operated in a working point[9] are digitized using one of the six input channels of the FADC that provide an input range of 0 to 20 V. To prevent aliasing, the signals are filtered using an RC low-pass filter with a cutoff frequency of $f_{3dB} = 80\,\mathrm{kHz}$.

An internal trigger of the FADC module, whose threshold can be set individually for each channel, is used to save events from the cryogenic detectors.

[7] A sinusoidal current can be generated by applying a sinusoidal voltage signal (generated by a function generator) to the input of the current source described in section 4.3.2. This voltage is converted into a current within the current source.

[8] GPIB is an abbreviation for General Purpose Interface Bus.

[9] A working point is characterized by the temperature of the detector holder (which is actively stabilized) and the applied bias current I_{Bias}.

Since the trigger is initiated once a set threshold is exceeded, any non constant (i.e., time dependent) DC offset on the signal has to be removed before triggering[10]. This is achieved by splitting the SQUID signal into a raw data signal and a trigger signal, both of which are fed into the FADC module. The trigger signal is filtered using an additional RC high-pass filter ($f_{3dB} = 8\,\mathrm{Hz}$) to remove the DC component of the signal. To be able to lower the trigger threshold, the trigger signal is additionally filtered using an RC low-pass filter with a cut-off frequency of $f_{3dB} = 1.7\,\mathrm{kHz}$ which removes high frequency noise contributing to the signal. This, however, also leads to a slight distortion of the signal which increases the trigger-walk of the threshold trigger. Figure 4.13 shows the "raw" signal (blue line, the pulse is only filtered by an 80 kHz low-pass filter[11]) and the trigger signal (red line) for a sample pulse. The effect of filtering the raw signal (i.e., reduction of the high frequency noise and distortion of the signal) can be seen. The trigger walk has to be considered when determining the pulse height by means of a template fit [119] (see section 5.4).

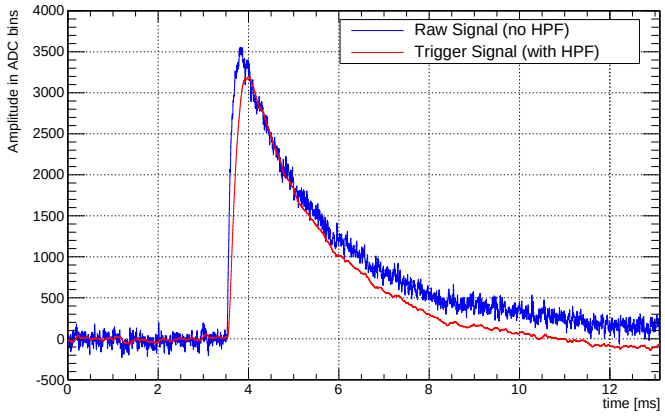

Figure 4.13: This plot shows both, the raw signal (blue line) and the trigger signal (red line) for a typical event in a cryogenic light-detector. The trigger signal is filtered using a 8 Hz high-pass filter in order to remove the DC component of the signal and a 1.7 kHz low-pass filter to remove high frequency noise from the signal. The "raw" signal is filtered using only a 80 kHz low-pass filter to prevent aliasing.

[10] The operational mode of the SQUID electronics leads to a varying DC offset.

[11] In the frequency domain, only frequencies smaller than $\sim 10\,\mathrm{kHz}$ contribute to the signal. Therefore, filtering the signal using an 80 kHz low-pass filter does not influence the signal [119]

Chapter 5

Measurements with a Cryogenic Detector Module

In this chapter, measurements of the Cherenkov radiation emitted from a TeO_2 crystal operated as a cryogenic phonon detector with a NL amplified cryogenic light detector will be discussed. The goal of these measurements is to show that a discrimination between γ induced events, which have an event signature similar to $0\nu\beta\beta$ events, and α induced events, which are considered a dominant background source in current generation $0\nu\beta\beta$ experiments, is possible on an event-by-event basis. The measurements will show for the first time that, at energies close to the $Q_{\beta\beta}$ value of ^{130}Te of $\sim 2.5\,\mathrm{MeV}$, an α-discrimination of $\gtrsim 99\%$ is possible while simultaneously accepting 99.8% of γ induced events (which have an event signature similar to the expected $0\nu\beta\beta$ signal).

In order to determine the suppression efficiency between α and e^-/γ induced events, measurements with a cryogenic detector module, consisting of a TeO_2 phonon and a NL light detector, irradiated with a ^{147}Sm α-source and a ^{228}Th γ-source have been performed.

5.1 Experimental Setup

The measurements performed in this work were performed with, a detector module consisting of a TeO_2 phonon detector and a Neganov-Luke amplified cryogenic light-detector. For the phonon detector, a $20 \times 20 \times 10\,\mathrm{mm}^3$ TeO_2 crystal with a mass of $\sim 24\,\mathrm{g}$ is used while the silicon absorber of the light detector is $20 \times 20 \times 0.5\,\mathrm{mm}^3$ in size. Both detectors are based on the composite detector design [73], using IrAu-based transition edge sensors evaporated

onto $5 \times 3 \times 0.5\,\mathrm{mm}^3$ silicon carrier substrates which are then glued onto the individual absorbers. The basic working principle of such detectors is described in section 2.1. The fabrication of IrAu transition edge sensors and the fabrication of aluminum electrodes for NL light detectors are described in section 4.1.1 and section 4.1.2, respectively.

The detector holder is mounted onto a cold plate below the mixing chamber of the ^{3}He/^{4}He dilution fridge (see section 4.2) by means of a Sintimid[1] rod which provides thermal and electrical insulation between the detector holder and the cryostat. A defined thermal link between the cold plate and the detector holder is established via a $\sim 1\,\mathrm{mm}$ diameter copper wire. The temperature of the detector holder is actively stabilized at a temperature of $\sim 42\,\mathrm{mK}$ using the technique described in section 4.3.1.

Figure 5.1 shows a schematic drawing of the detector module. The inner surface of the detector holder is covered with a light reflecting polymeric foil (3M© *VM2002*) to increase the collection efficiency of the Cherenkov radiation emitted from the TeO_2 crystal in the cryogenic light detector. Only the parts for mounting the detectors and additional openings in the detector holder, required for the bondpads for the TES readout and for the application of the NL voltage to the light detector, are left uncovered. For the energy calibration of the NL light detector, an optical fiber (see section 4.3.3) is used to guide light pulses generated by a LED operated outside the cryostat into the detector holder.

During the measurements, the phonon detector is irradiated by a ^{228}Th γ calibration source, placed outside the cryostat at a distance of $\sim 28\,\mathrm{cm}$ in the source lift indicated in figure 4.4, and a ^{147}Sm α source placed directly below the TeO_2 crystal (see figure 5.1) at a distance of $\sim 0.5\,\mathrm{cm}$. The α source is described in section 5.2).

It should be noted that the reflective foil (3M© *VM2002*) is also scintillating and that it can therefore not be used in future experiments employing the background suppression technique studied in this work[2]. This is due to the fact

[1] Sintimid is a polyimide with good mechanical properties at low temperatures. It furthermore provides good thermal and electrical insulation. The material used in the present work is *Tecasint 1011*, obtained from *ENSINGER GmbH*, Germany.

[2] Within this background suppression scheme, signal-like (e^-/γ) events are characterized by an energy deposition in the TeO_2 crystal and a simultaneous signal in the cryogenic light detector induced by the Cherenkov radiation emitted by highly energetic electrons within the crystal. α-induced background events on the other hand are characterized by a

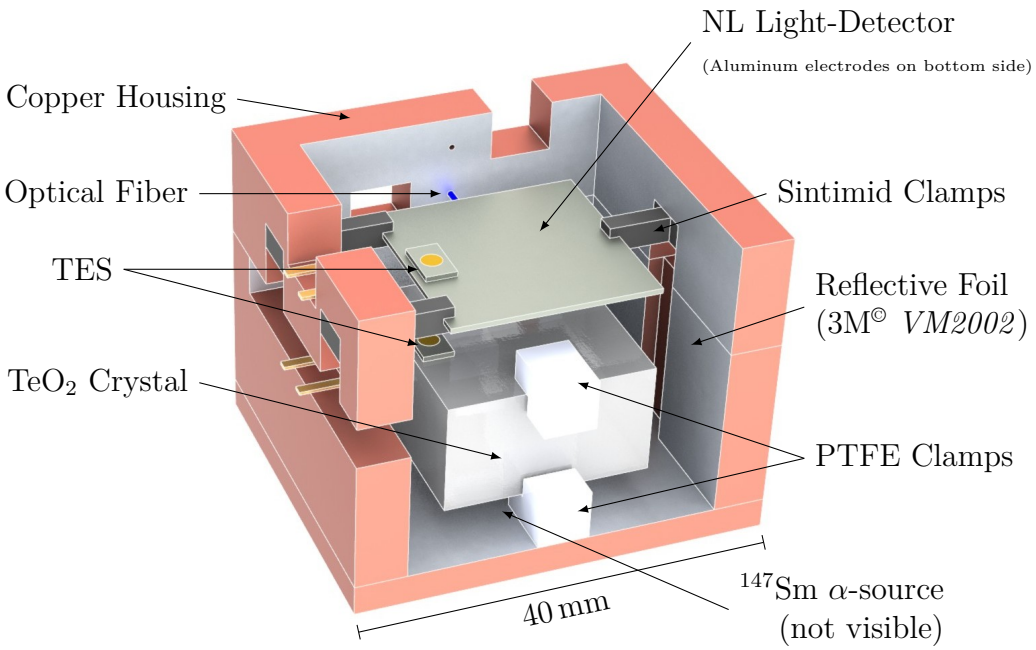

Figure 5.1: Schematic cut-away view of the detector module used for the measurement of Cherenkov radiation emitted from a TeO_2 crystal by α- and γ-induced events. A $20 \times 20 \times 10\,mm^3$ TeO_2 crystal is mounted inside a copper detector housing by means of four PTFE clamps. The Neganov-Luke amplified cryogenic light-detector is mounted using three Sintimid clamps. The inner surface of the copper housing is covered by a reflective polymeric foil (3M© *VM2002*). In order to perform an energy calibration of the light detector, an optical fiber is used to guide light from a LED operated at room-temperature directly into the detector housing. The temperature of the copper housing is actively stabilized at $\sim 42\,mK$. The aluminum electrodes of the NL light detector are located on the bottom side of the detector and are not visible here.

that α particles emitted at the surface of the crystal can produce scintillation light in the reflective and scintillating foil and therefore mimic the event signature of e^-/γ-induced events.

signal in the TeO_2 crystal and no simultaneous light emission from the crystal.

5.2 ^{147}Sm α-Source

In order to irradiate the TeO_2 crystal with α particles of an energy close to the Q-value of the $0\nu\beta\beta$ decay of ^{130}Te ($Q_{\beta\beta} = 2.53\,\text{MeV}$) a ^{147}Sm α-source is used.

Since no commercial source was available for the measurements in the present work, a custom made α source, consisting of a sheet of natural samarium, was employed. Natural samarium contains $\sim 15\%$ of ^{147}Sm [88], an α-decaying isotope of samarium with a half-life of $1.06 \cdot 10^{11}\,\text{yr}$ [121][3]. The specific α activity of natural samarium is $\sim 124\,\text{Bq/g}$ and the energy of the α particles emitted in the decay of ^{147}Sm is $\sim 2.31\,\text{MeV}$. Their range[4] within the material used to build the source is $\sim 6\,\mu\text{m}$ which indicates that only α particles emitted at or close to the surface of the source can reach the crystal. Since α particles not produced directly at the surface of the source lose part of their energy within the source, a flat spectrum of energy-degraded α events is expected.

Within the detector module, the source is placed in a groove machined into the bottom copper lid below the TeO_2 crystal and is fixed therein using low temperature varnish (also known as *IMI-7031* or *GE*, obtained from *Budzylek SCB GbR*, Germany). The dimensions of the samarium sheet are $\sim 13 \times 13 \times 1\,\text{mm}^3$. Figure 5.2 shows a photograph of the samarium source, mounted inside the copper lid and partly covered by a light reflecting foil (3M© *VM2002*). An area of $\sim 10 \times 10\,\text{mm}^2$ is left uncovered to provide a direct line of sight between the source and the TeO_2 crystal which is mounted directly above the α source (distance $\sim 0.5\,\text{cm}$). In order to prevent scintillation light from α particles which interact directly with the reflective foil, the surface of the foil facing the samarium source is covered by an $\sim 60\,\mu\text{m}$ thick Kapton tape.

To estimate the event rate expected from the source, it is assumed that the "active" volume is $10\,\text{mm} \times 10\,\text{mm} \times 6\,\mu\text{m}$ and only α-particles emitted within the solid angle covered by the crystal ($\sim 2/3\pi$) are considered. This leads to an expected α event rate of $\mathcal{O}(0.1\,\text{Hz})$ in the TeO_2 crystal.

[3] Since the other α-decaying isotopes of samarium are either only abundant in traces (^{146}Sm) or too long-lived (^{148}Sm) [88], their contributions to the total activity can be neglected.

[4] The range of the 2.31 MeV α-particles, emitted in the decay of ^{147}Sm, within samarium has been determined using the SRIM (The Stopping and Range of Ions in Matter) simulation software [122].

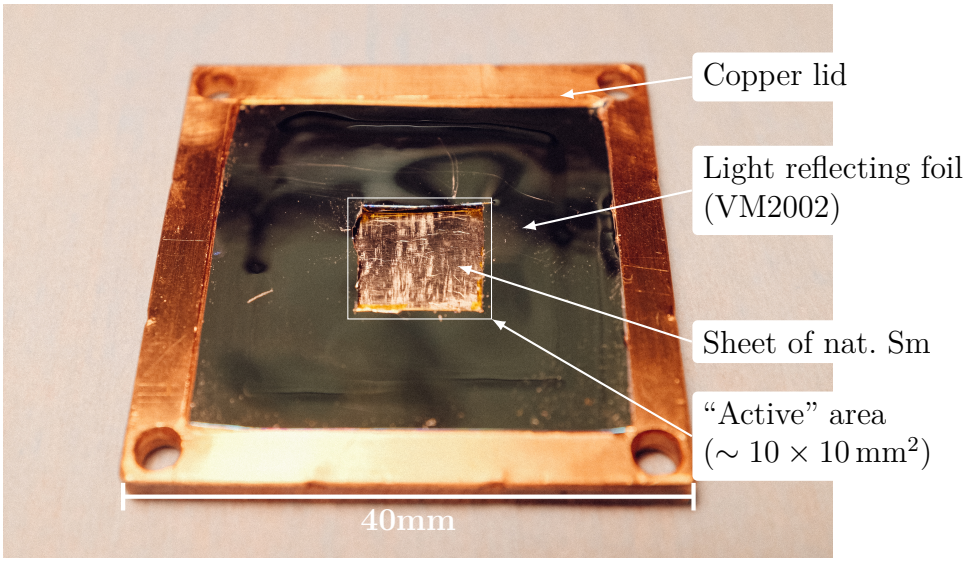

Figure 5.2: Photograph showing the sheet of natural samarium, used as an α source, mounted inside the bottom copper lid of the detector module. The copper lid is covered with a light reflecting foil (3M© *VM2002*) to increase the light collection efficiency in the detector module. Only an area of $\sim 10 \times 10\,\mathrm{mm}^2$ is left uncovered to provide a direct line of sight between the source and the TeO_2 crystal which is mounted directly above the source at a distance of $\sim 0.5\,\mathrm{cm}$.

5.3 Cryogenic Detectors

5.3.1 Neganov-Luke Amplified Light Detector

The Neganov-Luke amplified light detector (internal designation *Si593D*) consists of a $20 \times 20 \times 0.5\,\mathrm{mm}^3$ high-purity p-type silicon substrate (specific resistivity $\rho > 6\,\mathrm{k\Omega\,cm}$ at room temperature, both sides of the substrate are highly polished ("epi-polished") which acts as a light absorber. The phonon signals, induced by the absorbed photons, are read-out using a superconducting IrAu TES which is evaporated onto a $5 \times 3 \times 0.5\,\mathrm{mm}^3$ silicon carrier and then glued to the top of the absorber using an epoxy resin with good thermal properties at cryogenic temperatures (*Epo-Tek 301-2*, obtained from *John P. Kummer GmbH*, Germany). The fabrication of TESs is described in section 4.1.1.

On the bottom side, the silicon substrate is equipped with four aluminum electrodes (each $18 \times 0.2\,\mathrm{mm}^2$ in size and $\sim 500\,\mathrm{nm}$ thick, the distance between the electrodes is $\sim 6\,\mathrm{mm}$) which are used to generate the electric field required for the operation of the light detector in the Neganov-Luke amplified mode (refer to section 2.2 for a description of the working principle of NL light detectors and to section 4.1.2 for a description of the production process). This electric field is generated by a so-called Neganov-Luke voltage V_{NL} which is applied between adjacent electrodes. Figure 5.3 shows a schematic of the electrode layout as well as the way the voltage is applied between the individual electrodes.

The super-to-normal-conducting transition of the TES, which has a transition temperature of $T_C \approx 63\,\mathrm{mK}$ and a transition width of $\Delta T_C \approx 3\,\mathrm{mK}$, is depicted in figure 5.4. The detector holder is stabilized at a temperature of $\sim 42\,\mathrm{mK}$ (indicated by the red line in figure 5.4). This temperature is optimized to operate both the light detector and the TeO_2 phonon detector (see section 5.3.2) simultaneously. The TES is heated to the working point in the transition region by applying a bias current of $I_{Bias} \approx 110\,\mu\mathrm{A}$.

For this detector, a Neganov-Luke voltage of up to $\sim 110\,\mathrm{V}$ can be applied between the electrodes. Above this voltage, sudden break-downs of the substrate occurred which are likely caused by a current flowing across the absorber surface which leads to an immediate heating of the detector, the holder and the mixing chamber to temperatures of $100 - 200\,\mathrm{mK}$. During the measurements presented in this work, the device was operated continuously for periods of up to $\sim 42\,\mathrm{h}$ with a voltage of $V_{NL} = 70\,\mathrm{V}$ applied between the electrodes.

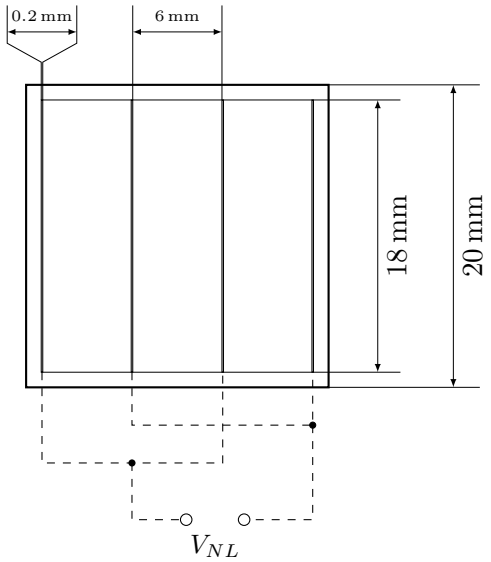

Figure 5.3: Schematic drawing illustrating the layout of the aluminum electrodes on the Neganov-Luke (NL) light detector *Si593D*. The dimensions of each strip are $0.2 \times 18\,\mathrm{mm}^2$ and the distance between the strips is $\sim 6\,\mathrm{mm}$. The thickness of the aluminum electrodes is $\sim 500\,\mathrm{nm}$. The dotted lines indicate the way the NL voltage is applied between the electrodes.

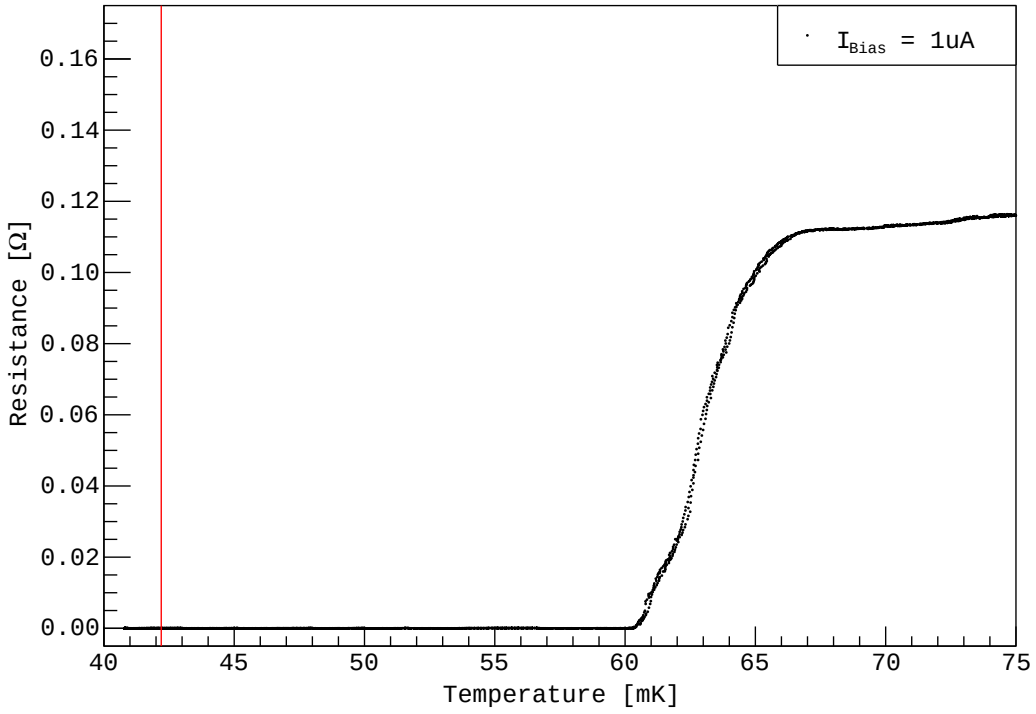

Figure 5.4: Super-to-normal-conducting transition curve of the IrAu TES used to readout the heat signals of the Neganov-Luke amplified light-detector (*Si593D*). The transition temperature of the TES is $T_C \approx 63\,\mathrm{mK}$ and the transition width is $\Delta T_C \approx 3\,\mathrm{mK}$. The transition curve was recorded by sweeping the temperature of the detector holder between $\sim 40\,\mathrm{mK}$ and $\sim 75\,\mathrm{mK}$, starting from below the transition temperature. A bias current of $1\,\mu\mathrm{A}$ was used to record this transition curve by means of the technique described in section 4.3.4. The red line indicates the temperature ($\sim 42\,\mathrm{mK}$) used to stabilize the detector holder during the measurements discussed in this work.

Energy Calibration without Applied Neganov-Luke Voltage

The energy calibration of the cryogenic light detector is performed using a calibration scheme based on the counting-statistics of the photons absorbed by the light detector as described in [59, 60] and [61]. At first, the calibration of the light detector without an applied NL voltage will be described[5].

For the calibration, the light detector is illuminated with short light pulses of various intensities, generated by a LED operated outside the cryostat at room temperature (compare section 4.3.3). Since the NL light detectors described in this work are primarily developed in the framework of direct dark matter search with $CaWO_4$ crystals, a LED[6] matching the scintillation spectrum of these crystals is used. However, the wavelength of the LED can be adapted to match the spectral response of other scintillating crystals as well. As will be discussed later, matching the LED to the spectral shape of Cherenkov radiation, due to the wide energy spectrum, was not possible in the present work.

The data acquisition system is triggered in coincidence with the LED signal and the raw pulses of the events in the light detector are recorded. For each individual event, the corresponding pulse height of the light detector is then determined in an offline analysis using a template fit on the raw pulses from the light detector (for a description of the applied fit refer to [119]).

Figure 5.5 shows several pulse-height spectra corresponding to the different LED intensities used in this calibration measurement. Following [59, 60], the pulses corresponding to an individual LED intensity are characterized by a mean pulse height x and a peak width σ_{tot}. These parameters are determined by fitting a gaussian function to each individual pulse-height spectrum as illustrated in figure 5.5.

In the case of a linear detector response, it is assumed that the total photon energy (E) for each detected light pulse in the cryogenic light detector is

[5] During the LED calibration measurements and measurements with calibration sources performed without an applied NL voltage, both NL electrodes were connected to ground potential outside the cryostat via an $50\,\Omega$ resistance.

[6] A blue InGaN LED ($\lambda_{LED} \approx 430\,\text{nm}$, corresponding to $E_{ph} \approx 2.9\,\text{eV}$), model *LED430-06* from *Roithner Lasertechnik*, Vienna, Austria is used.

directly proportional to the pulse height (x) of the heat signal[7], i.e.:

$$E = E_{ph} \cdot N = \frac{E_{ph}}{a} \cdot x = b \cdot x \tag{5.1}$$

where E_{ph} is the average energy of the detected photons and N is the number of detected photons. The parameter $a = \frac{x}{N}$ is a conversion factor between the pulse height x and the number of detected photons N.

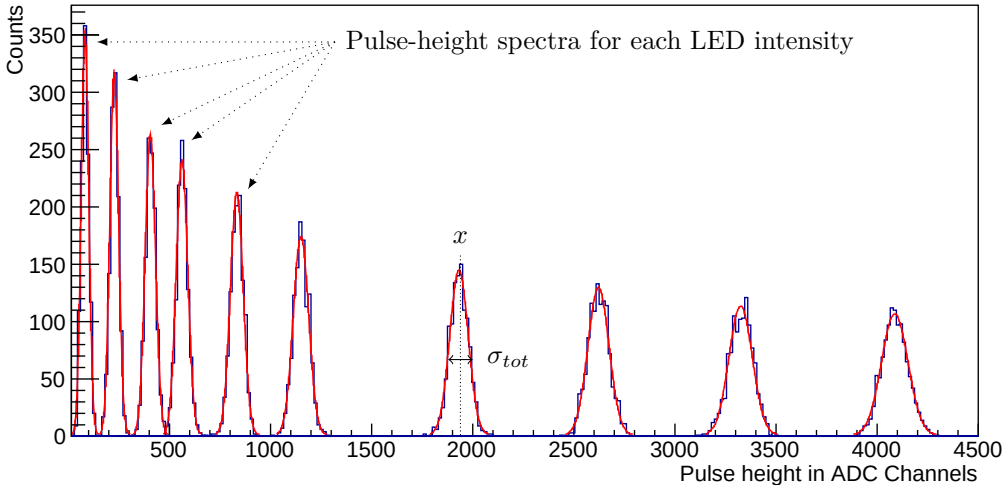

Figure 5.5: This figure illustrates the method used to derive the parameters required for the LED calibration technique. For each LED intensity, a histogram (blue lines) of the corresponding pulse heights (obtained from a template fit [119] of the raw pulses) is fitted with a gaussian function (red lines) to determine the average pulse height x and the variance σ_{tot}.

Equivalently, the parameter $b = E_{ph}/a = N \cdot E_{ph}/x$ (b is given in units [eV/Ch.][8]) is a conversion factor between the total energy and the corresponding pulse height. These scaling factors can be determined using the LED calibration technique.

[7]This assumption, however, is only valid for an instantaneous energy deposition in the light detector as it is expected for the LED calibration as well as the Cherenkov radiation emitted from TeO_2 crystals. For light detected from $CaWO_4$ crystals (e.g., in the CRESST-II experiment [52]), the time constant of the scintillation process leads to an energy deposition that is no longer instantaneous. See [61] for a description of the scintillation process in $CaWO_4$.

[8]The pulse height is measured in units of ADC channels of the data acquisition system. Throughout the present work, the abbreviation **Ch.** is used for ADC channels.

The peak width σ_{tot} (derived from fitting a gaussian function to the amplitude spectrum (compare figure 5.5)) corresponding to a certain LED intensity is assumed to depend only on contributions independent from each other, i.e., electronic noise (σ_{el}), position dependence (σ_{pos}), charge trapping (σ_{tr}) etc. and a contribution due to photon counting statistics (σ_{ph}), and can be expressed as [59, 60]:

$$\sigma_{tot}^2(E) = \sigma_{ph}^2(E) + \sigma_{el}^2 + \sigma_{tr}^2 + \sigma_{pos}^2 + ... \tag{5.2}$$

Furthermore, an energy dependence of all other contributions apart from the photon counting statistics is neglected. In this case, the peak width can be written as [59, 60]:

$$\sigma_{tot}^2(E) = \sigma_0^2 + \sigma_{ph}^2(E) \tag{5.3}$$

where the term σ_0^2 accounts for all energy independent contributions[9] and $\sigma_{ph}(E)$ describes the contribution due to photon counting statistics ($\sigma_N(N) = \sqrt{N}$). This contribution can be written in terms of ADC channels as [59, 60]:

$$\sigma_{ph}(x) = a \cdot \sigma_N(N) = a \cdot \sqrt{N} \tag{5.4}$$

The total peak width[10] can then be written as [59, 60]:

$$\sigma_{tot}(x) = \sqrt{\sigma_0^2 + \sigma_{ph}^2(x)} = \sqrt{\sigma_0^2 + a^2 \cdot N} = \sqrt{\sigma_0^2 + a \cdot x} \tag{5.5}$$

This relation is referred to as "calibration function" and is used to describe the parameters (i.e., $\sigma_{tot}(x)$) which are obtained by fitting the spectra corresponding to the individual intensities with a gaussian function (compare figure 5.5).

Figure 5.6 shows a plot of the obtained parameters for the LED calibration measurement shown in figure 5.5[11]. Both the constant term σ_0 as well as the

[9] The term σ_0 can be interpreted as the width of the baseline (σ_{BL}) of the light detector, i.e., the statistical fluctuation of the noise present in all recorded pulses. Similar to figure 5.5, a pulse height spectrum of events where no light pulses are present can be fitted with a gaussian function to determine σ_{BL}. Here, a value of $\sigma_{BL} = 16.5 \pm 0.3$ Ch. is obtained.

[10] Here, σ_0 is given in units of ADC channels.

[11] This calibration was performed prior to the measurement described in section 5.6. Since the operational conditions (i.e., the working point and the noise present during the measurement) can slightly change between individual measurements, e.g., if the cryostat has been refilled between measurements, the calibration measurements are performed prior to each measurement. In order to ensure operation in the correct working point, an active detector stabilization technique has to be employed. The operation of Neganov-Luke amplified cryogenic light detectors with with an active stabilization similar to the method used by the CRESST-II experiment [123, 124] is currently being investigated [125].

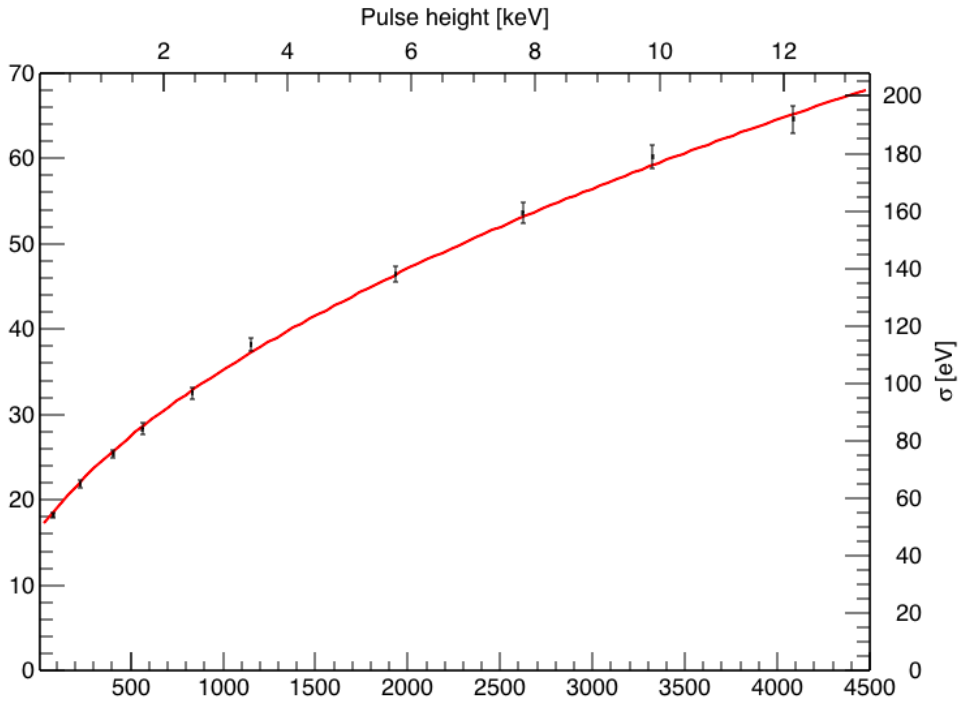

Figure 5.6: This plot shows the data points (black points) obtained from the measurement performed with NL light detector *Si593D* shown in figure 5.5. The error bars along both axis indicate the 1σ errors from the gaussian fit. A calibration function (equation (5.5)) is fitted to the data points (red line) to obtain the constant noise term σ_0 and the conversion factor a between the pulse height and the number of detected photons. The additional y-axis on the right shows the corresponding energy resolution of the detector in eV and the additional x-axis on the top shows the pulse height in keV.

scaling factor a are obtained by fitting the calibration function (eq. (5.5)) to the data points. The resulting fit function is also shown in figure 5.6 (red line). From the fit the following parameters are obtained for this measurement:

$$\sigma_0 = 16.29 \pm 0.19\,[\text{Ch.}] \tag{5.6}$$

$$a = 0.97 \pm 0.02\,[\text{Ch./photon}] \tag{5.7}$$

The errors correspond to the 1σ errors of the fit. The corresponding energy scale can also be calculated from the fit parameters of the fitted calibration function (eq. (5.6) and (5.7)):

$$b = 2.97 \pm 0.06\,[\text{eV/Ch.}] \tag{5.8}$$

and, therefore, the constant term σ_0 corresponds to $48.5 \pm 1.1\,\text{eV}$.

The energy resolution of the detector can also be written in terms of the detected energy as:

$$\sigma_{tot}(E) = \sqrt{\sigma_0^2 \cdot b^2 + E_{ph} \cdot E} \tag{5.9}$$

where E_{ph} is the average energy of the detected photons and E is the total energy detected by the light detector. In figure 5.6, the energy resolution in eV is given on the right y-axis while the energy E in keV is given on the upper x-axis.

The LED calibration technique has several advantages compared to a calibration performed with ^{55}Mn x-rays emitted by a ^{55}Fe source, which provides two ^{55}Mn X-ray lines at 5.9 keV and 6.5 keV and is commonly used to perform an energy calibration of cryogenic detectors:

a) For the measurements performed in this work, the energy provided by these X-ray lines is much higher than the expected signal of $\lesssim \mathcal{O}(400\,\text{eV})$ due to Cherenkov radiation. Therefore, the light detector resolution at low energies cannot be determined using a ^{55}Fe calibration. In [59, 60, 61] it was found that the energy scales obtained with an LED calibration and with a ^{55}Fe calibration are in very good agreement within $\lesssim 1\%$.

b) The absorption of ^{55}Mn X-rays leads to a localized energy deposition giving rise to $\mathcal{O}(1500)$ electron-hole pairs[12] while the absorption of

[12]This value can be obtained from the total energy ($\sim 6\,\text{keV}$) and the average energy required to create an electron-hole pair (3.64 eV [78]) in silicon.

optical photons in the spectral ranges relevant for both direct dark matter search with $CaWO_4$ as well as for the background suppression in TeO_2 leads to single electron-hole pairs distributed over the absorber surface.

c) The light detector can be calibrated using light with a wavelength matching the scintillation spectrum of the specific crystal used in the experiment.

d) As has been shown in [59], the detector's response, when operated in NL mode, to ^{55}Mn x-rays is different compared to the response to optical photons. This effect arises from the localized energy deposition (see [59] for details).

In the measurements performed in this work (see section 5.5 and section 5.6) the cryogenic light detector is used to detect Cherenkov radiation emitted by electrons within a TeO_2 crystal. The emitted Cherenkov radiation follows a broad spectral shape with a $\sim 1/\lambda^2$ wavelength dependence (see figure 3.2 for a simulated spectrum) and the detected spectrum furthermore depends on the optical properties of the TeO_2 crystal, the light reflecting foil, and the silicon absorber (i.e., their respective reflectivity, transmission, and absorption spectra). Therefore, the average detected wavelength is very likely to be different from the wavelength used during LED calibration and therefore also the detector resolution with respect to the detected Cherenkov photons.

The energy calibration obtained with the LED calibration technique is also applied to the measurements where Cherenkov radiation is detected. It is therefore assumed that the energy scale derived using the LED calibration technique (i.e., the detected energy corresponding to a certain pulse height of the heat signal in the light detector) does not depend on the wavelength of the detected photons (i.e., it is assumed that all deposited energy is converted into heat[13]). In the present work this aspect has not yet been not studied, however, measurements with LEDs of different wavelengths are planned in order to study this aspect [125, 127].

[13]Depending on the energy of the created electron-hole pairs (and therefore depending on the energy of the absorbed photons), part of the absorbed energy could be lost due to trapping of the charge carriers in defects within the absorber [126]. Furthermore, part of the emitted Cherenkov spectrum is emitted in the spectral range between $\sim 300\,\text{nm}$ and $\sim 390\,\text{nm}$, where one photon can, with a certain probability, produce more than one electron-hole pair [79]. Depending on the light collection within the detector module (see, e.g., section 2.4), part of these photons could also be absorbed in the light detector. These effects could, in principle, affect the conversion of the absorbed energy into heat.

Thermal Gain and Energy Calibration with Applied NL Voltage

When a cryogenic light detector is operated with a Neganov-Luke voltage V_{NL} applied between the electrodes and irradiated by photons with an average energy E_{ph}, the expected theoretical thermal gain G_{th} can be calculated from equation (2.4) in section 2.2. The experimentally observed thermal gain G_{exp} can be determined by comparing LED calibration measurements performed both with and without applied NL voltage.

With applied NL voltage, the average pulse height x_{0V} of a light signal with a certain intensity is amplified by the factor G_{exp} and results in pulses with an average pulse height $x_{NL}(V_{NL})$:

$$x_{NL}(V_{NL}) = x_{0V} \cdot G_{exp}(V_{NL}) \tag{5.10}$$

The thermal gain can then be derived by averaging the gain obtained from several peaks which have known intensities [61]:

$$G_{exp}(V_{NL}) = \frac{1}{n} \sum_{i=1}^{n} \frac{x_{i,NL}(V_{NL})}{x_{i,0V}} \tag{5.11}$$

Due to the trapping of the drifted charge carriers in impurities and defects, leading to reduced drift lengths of the charge carriers, the observed gain is typically smaller than the theoretically predicted value. Furthermore, due to the potential accumulation of charge carriers in the vicinity of the aluminum electrodes (compare discussion in [59]), the thermal gain can decrease over time when the detector is exposed to ionizing radiation and optical photons.

The energy scale of the Neganov-Luke amplified pulses can be deduced solely from the measured thermal gain by introducing a new scaling factor which takes the amplification of the signal into account [61]:

$$a_{NL}(V_{NL)} = a \cdot G_{exp}(V_{NL}) \tag{5.12}$$

$$b_{NL}(V_{NL}) = b/G_{exp}(V_{NL}) \tag{5.13}$$

therefore linking the energy scale obtained from the 0 V calibration to the measurement with applied NL voltage V_{NL}.

Typically, the thermal gain is obtained from a LED calibration measurement performed with applied NL voltage. However, the energy scale can in principle also be derived in this way when the spectrum of the light emitted from the crystal does not match the wavelength emitted by the LED or is not exactly known (e.g., for Cherenkov radiation as mentioned before when discussing

the LED calibration without applied NL voltage) by obtaining the thermal gain from the signal amplification observed for certain reference points, e.g., the average amount of light detected from γ lines (which can be identified using the energy deposition in the phonon detector). However, it should be noted that this aspect also requires further studies.

Energy Resolution with Applied NL Voltage

The application of the LED calibration technique to cryogenic light-detectors operated with applied Neganov-Luke voltage with the goal to determine the energy-dependent energy-resolution is discussed in great detail in [61].

Assuming that operating the NL light detector with applied voltage only results in an amplification of the heat signal and that any other effects can be neglected, the expected detector resolution can be derived from equation (5.5):

$$\sigma_{NL}(x) = \sqrt{\sigma_0^2 + a \cdot G_{exp}(V_{NL}) \cdot x} \tag{5.14}$$

and equivalently, the energy resolution can be written as:

$$\sigma_{NL}(E) = \sqrt{\sigma_0^2 \cdot b^2 / G_{exp}(V_{NL})^2 + E_{ph} \cdot E_{tot}} \tag{5.15}$$

In this case, the improvement in energy resolution can be attributed to an increased signal-to-noise ratio, i.e., a relative reduction of the constant term σ_0 and therefore an overall increase of the energy resolution.

It has been shown in [61] that, with applied NL voltage, the detector resolution is no longer described by the model used without applied NL voltage.

When operated with applied NL voltage, additional energy-dependent contributions to the energy resolution become important: In [61], an extended model of the detector resolution with applied NL voltage has been introduced:

$$\sigma_{NL}(x) = \sqrt{\sigma_0^2 + \sigma_{0,NL}(V_{NL})^2 + a \cdot G_{exp}(V_{NL}) \cdot x + \sigma_{cc}^2 + \sigma_{rc}^2} \tag{5.16}$$

which takes additional uncertainties in the amplification process of the heat signal (and therefore an uncertainty in the effectively measured energy) into account:

- The term $\sigma_{0,NL}(V_{NL})$ describes additional, energy independent, contributions to the detector noise, introduced by the application of the NL voltage (compare also [59]).

- The term $\sigma_{cc}(V_{NL}) = \sqrt{c_{cc}(V_{NL}) \cdot x} \propto \sqrt{N}$ describes an uncertainty in the amplification process of the heat signal induced by each electron-hole pair, i.e., by each absorbed photon, due to an incomplete charge collection of the generated electron hole pairs, caused by reduced drift lengths.

- The term $\sigma_{rc}(V_{NL}) = \sqrt{c_{rc}(V_{NL}) \cdot x^2} \propto N$ describes an uncertainty in the amplification process of the heat signal due to an uncertainty in the number of drifted electron-hole pairs, caused by a recombination of the charge carriers while being drifted in the electric field.

A detailed description motivating the introduction of these terms and their dependence on the NL voltage is given in [61]. The energy resolution corresponding to eq. (5.16) can be obtained by multiplying (5.16) with the conversation factor of (5.13):

$$\sigma_{NL}(x) = \sqrt{\sigma_0^2 + \sigma_{0,NL}(V_{NL})^2 + a \cdot G_{exp}(V_{NL}) \cdot x + \sigma_{cc}^2 + \sigma_{rc}^2} \cdot b_{NL}(V_{NL}) \qquad (5.17)$$

Figure 5.7 shows the energy resolution obtained from an LED calibration measurement (triangular data points with error bars and dashed red line) performed with a NL voltage of $V_{NL} = 70\,\mathrm{V}$ applied between the electrodes together with the previously discussed LED calibration without NL voltage (circular data points with error bars and solid blue line, compare figure 5.6)[14]. The figure furthermore shows the expected energy resolution given by equation 5.15 (blue dashed line). It can be seen that the data with applied NL voltage cannot be described using the model given in equation 5.15 but is well described by the model taken from reference [61] (given in equation (5.16)). Below an energy of $\sim 1400\,\mathrm{eV}$, the energy resolution of the detector operated with applied NL voltage improves compared to the calibration performed without applied NL voltage. Above this energy, the additional terms in eq. (5.9) lead to an energy resolution which is worse compared to the measurement performed without NL voltage.
The observed thermal gain is $G_{exp}(V_{NL} = 70\,\mathrm{V}) = 10.8 \pm 0.1$ (see eq. (5.11)) while the theoretical thermal gain expected form equation (2.4) (section 2.2) is $G_{th}(70\,\mathrm{V}) = 25.3$, i.e., a factor of ~ 2.5 larger than the observed value. The 1σ threshold of the NL detector with applied NL voltage is $\sigma_{NL}(x = 0) = 7.8 \pm 0.2\,\mathrm{eV}$, corresponding to an increase in the S/N ratio by a factor of 6.2 ± 0.1.

[14] This calibration was performed prior to the measurement discussed in section 5.6. The obtained fit results are: $\sigma_{0,NL}(70\,\mathrm{V}) = 23.0 \pm 0.2$ Ch, $c_{rc}(70\,\mathrm{V}) = 5.01 \pm 0.37$, and $c_{cc}(70\,\mathrm{V}) = (1.69 \pm 0.55) \cdot 10^{-4}$. The width of the baseline during this measurement was $\sigma_{BL} = 28.3 \pm 0.2\,\mathrm{Ch}$.

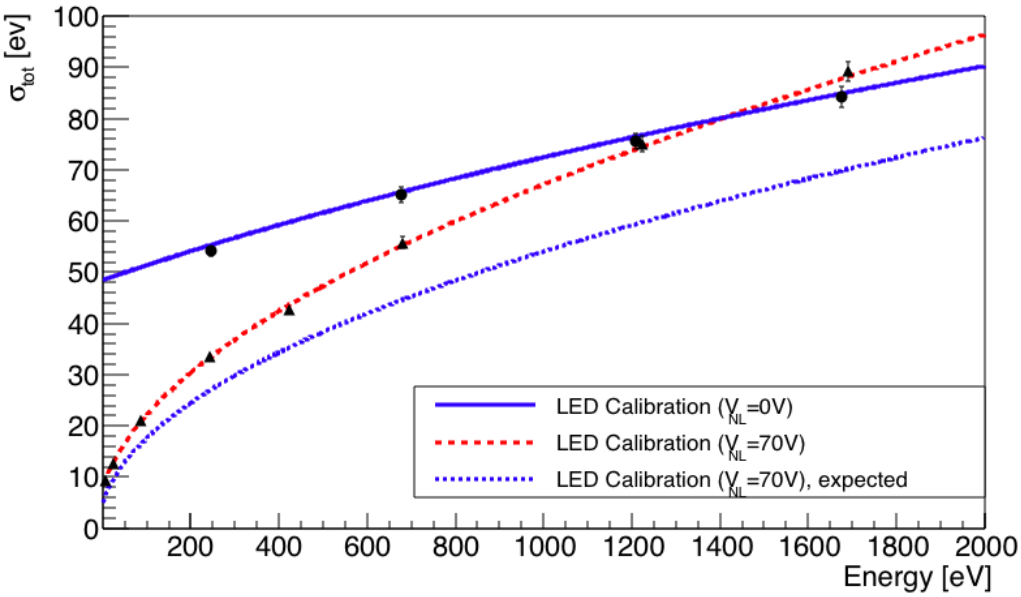

Figure 5.7: Energy resolution of the NL light detector without applied NL voltage (circular data points and solid blue curve corresponding to eq. (5.9)) and with applied NL voltage (triangular data points and dashed red fit curve corresponding to eq. (5.16)). Below $\sim 1400\,\mathrm{eV}$, the resolution of the light detector improves when operated in NL mode while above this energy, the additional terms in eq. (5.16) lead to a worse energy resolution. However, in the energy interval relevant for the detection of Cherenkov radiation emitted from a TeO_2 crystal ($0-400\,\mathrm{eV}$, compare, e.g., chapter 3), the resolution is significantly improved. The dashed blue line shows the expected energy resolution for a NL amplified cryogenic light detector as described by eq. 5.15.

Time Dependence of the Neganov-Luke Amplification

As reported in [59, 60], Neganov-Luke amplified cryogenic light detectors can exhibit a reduction of the pulse height over time when operated with applied NL voltage, which is caused by a reduction of the observed thermal gain. In [59, 60] this reduction is explained by an accumulation of charge carriers in defects in the vicinity of the aluminum electrodes. These charge carriers are expected to build up an internal counter-field to the externally applied NL voltage and in this way effectively reducing the voltage applied across the substrate with time. These defects are likely generated during the production process of the electrodes. In [59], a reduction of the pulse height by $\sim 20\%$ within $\sim 1\,\mathrm{h}$ was reported at a photon flux of approximately $50\,\mathrm{keV/\,sec}$[15].

In [61], a novel production process for the aluminum electrodes was developed which includes an additional process to anneal the silicon absorber after the deposition of the aluminum electrode strips (see also section 4.1.2). Due to this additional step, the number of defects below the aluminum contacts is significantly reduced leading to no observable decrease of the pulse height with time[16].

The light detector described in the present work was manufactured according to the new production process proposed in [61], however, the annealing step was performed under N_2 atmosphere instead of a forming gas atmosphere. A dedicated measurement where the light detector was irradiated by a constant photon flux has been performed to assess the reduction of the observed pulse height with time. Figure 5.8 shows the obtained pulse heights versus the corresponding time stamp. The data points are fitted using a function of the form:

$$A(t) = A_0 + \exp(p_1 + p_2 \cdot t) \tag{5.18}$$

[15]The photon flux is an important parameter when comparing measurements with different detectors since the rate by which the pulse height decreases depends on the number of electron-hole pairs created by each light pulse (i.e., the reduction depends on the rate by which the available defects and traps are filled by charge carriers.).

[16]During the measurement presented in [61] the light detector was irradiated with a comparable photon flux and no significant decrease of the pulse height was observed.

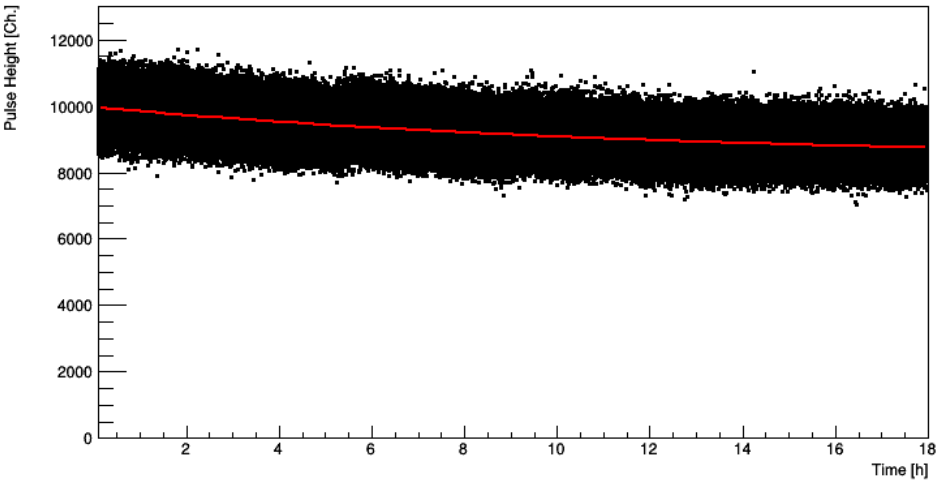

Figure 5.8: Time dependence of the measured pulse height of pulses recorded with the Neganov-Luke light detector (*Si593D*) used for the measurements in this work. The device is operated with a NL voltage of $V_{NL} = 70V$ and irradiated with light pulses from the blue LED at a rate of 20 Hz. The average pulse height corresponds to a detected energy of $\sim$ 3 keV and, therefore, the photon flux corresponds to $\sim$ 60 keV/ sec. During the 18 h measurement, the pulse height is reduced by $\sim$ 12%. The data points are fitted using the function given in equation (5.18).

and the following parameters are obtained:

$$A_0 = 8397.4 \pm 4.9\,[\text{Ch.}] \tag{5.19}$$
$$p_1 = 7.358 \pm 0.003 \tag{5.20}$$
$$p_2 = -0.083 \pm 0.001\,[1/\text{h}] \tag{5.21}$$
$$\tag{5.22}$$

During the measurement, the light detector was exposed to a photon flux of $\sim 60\,\text{keV}/\,\text{sec}$ and a reduction of the pulse height of only $\sim 12\%$ was observed after 18 h which corresponds to a reduction of $\sim 0.7\%$ in 1 h, a factor ~ 30 less than the reduction reported in [59, 60]. The observed reduction is an important factor which significantly influences the time interval between necessary regenerations of the detector. However, the influence of the specific atmosphere used during the annealing process has to be studied further in future experiments to improve the reproducibility of the fabrication process.

Summary

Using the LED calibration technique, it could be shown that the energy resolution of the light detector increases significantly at low light energies between $0-400\,\text{eV}$ (the energy range relevant for the detection of Cherenkov radiation emitted form a TeO_2 crystal in the present work) when operated with applied NL voltage compared to the operation of the detector without applied NL voltage.

Furthermore, it could be shown that the light detector can be operated continuously for extended periods of time without regeneration. This aspect is very significant for the application of NL detectors for rare event search experiments (e.g., direct dark matter search experiments like CRESST-II or future experiments searching for the neutrinoless double beta decay) which are expected to take data continuously for up to several years[17].

Until now, the achieved thermal gain is smaller than the theoretically expected value (compare also measurements performed in [59, 60] and [61]) and only relatively low voltages can be applied between the electrodes. The origin of these issues is currently being investigated and within the present work, a new manufacturing technique to produce the aluminum electrodes has been devised (see appendix A). First measurement show promising results, allowing

[17] The event rate in cryogenic rare event search experiments is typically $\lesssim \mathcal{O}(1\,\text{Hz})$, much smaller than the event rates within the present work, and, therefore, the operational time between the regeneration of NL light detectors is also expected to be significantly extended.

of voltages of up to $\sim 600\,\mathrm{V}$ to be applied between the electrodes [128]. First NL-amplified light detectors based on this new fabrication technique are presently also under investigation [127].

5.3.2 TeO_2 Phonon Detector

The phonon detector used for the measurements performed in this work (internal designation *Si591D*) consists of a $20 \times 20 \times 10\,\mathrm{mm}^3$ TeO_2 crystal with a mass of $\sim 24\,\mathrm{g}$. Figure 5.9 shows the phonon detector mounted inside the copper detector holder where the crystal is held by means of four PTFE clamps. The inner surfaces of the detector housing are almost completely (see below) covered by the same light reflecting foil (3M© *VM2002*) also used for the other parts of the detector module. All surfaces of the TeO_2 crystal are roughened to reduce trapping of the produced Cherenkov radiation within the crystal due to total internal reflection. (The influence of surface roughening on the light collection efficiency is, for example, described in [129] and is confirmed by the simulations performed in appendix A).

The detector is equipped with an IrAu TES (a circular film, $\varnothing \approx 2\,\mathrm{mm}$), which is evaporated onto a $5 \times 3 \times 0.5\,\mathrm{mm}^3$ silicon carrier and then glued to the crystal using epoxy resin (*Epo-Tek 301-2*). The TES is used to measure the heat signal induced by particle interactions in the crystal and the super-to-normal-conducting transition of the TES film is shown in figure 5.10 (the fabrication of IrAu thin films is described in section 4.1.1). The TES has a transition temperature of $T_C \approx 55\,\mathrm{mK}$ and a transition width of $\Delta T_C \approx 5\,\mathrm{mK}$. The temperature of the detector holder is, as mentioned in section 5.3.1, stabilized at a temperature of $\sim 42\,\mathrm{mK}$ which is optimized for the simultaneous operation of the phonon and light detector. The TES of the TeO_2 phonon detector is heated to the working point in the transition region by applying a bias current of $I_{Bias} \approx 72\,\mu\mathrm{A}$.

The TES is connected to the readout circuit using $25\,\mu\mathrm{m}$ diameter aluminum bond wires and the thermal coupling between the TES and the heat bath is realized using two $25\,\mu\mathrm{m}$ gold bond wires. The housing is not completely covered by the reflective foil since small openings are required by the PTFE support structure and the bond pads to reach into the detector holder. A significant amount of the emitted light ($\sim 1/3$, value obtained using the simulation described in appendix A) can escape the detector module. Thus, for future measurements, the coverage with the reflective foil will be increased further to achieve an improved light collection efficiency.

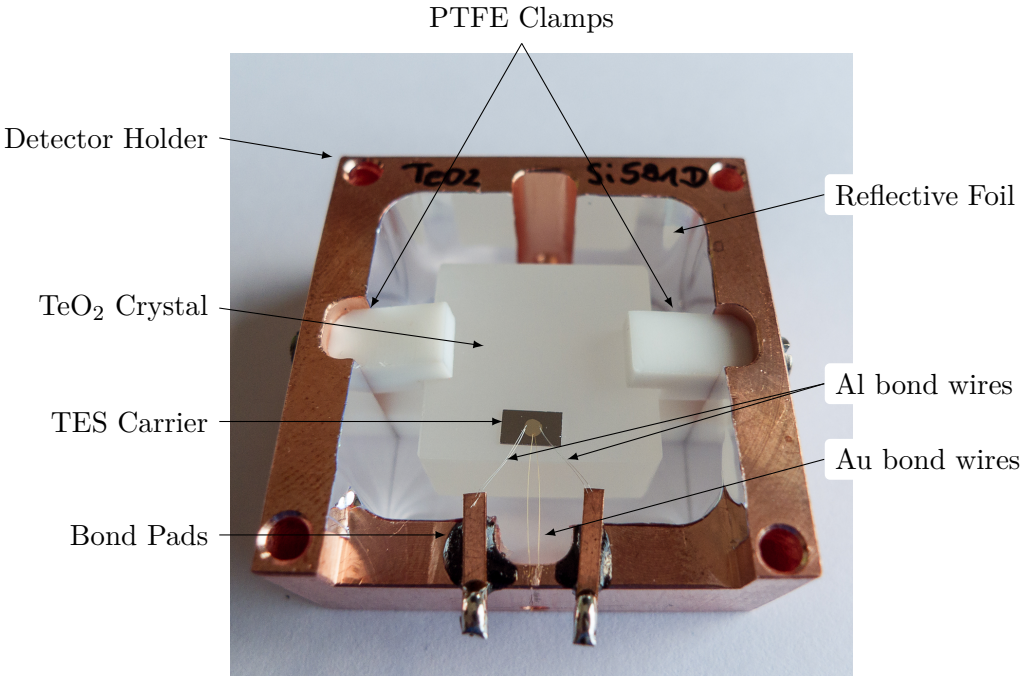

Figure 5.9: Photograph showing the $20 \times 20 \times 10\,\mathrm{mm}^3$ TeO_2 crystal mounted inside a copper detector holder by means of four PTFE clamps. To read out the heat signal induced by particle interactions, the crystal is equipped with an IrAu TES, evaporated onto a silicon carrier substrate which is glued to the absorber using *Epo-Tek 301-2* epoxy resin. The inner surface of the holder is covered with the same light reflecting foil used for all other components of the detector module (3M© *VM2002*). All sides of the crystal are roughened to increase light collection efficiency within the detector module [129].

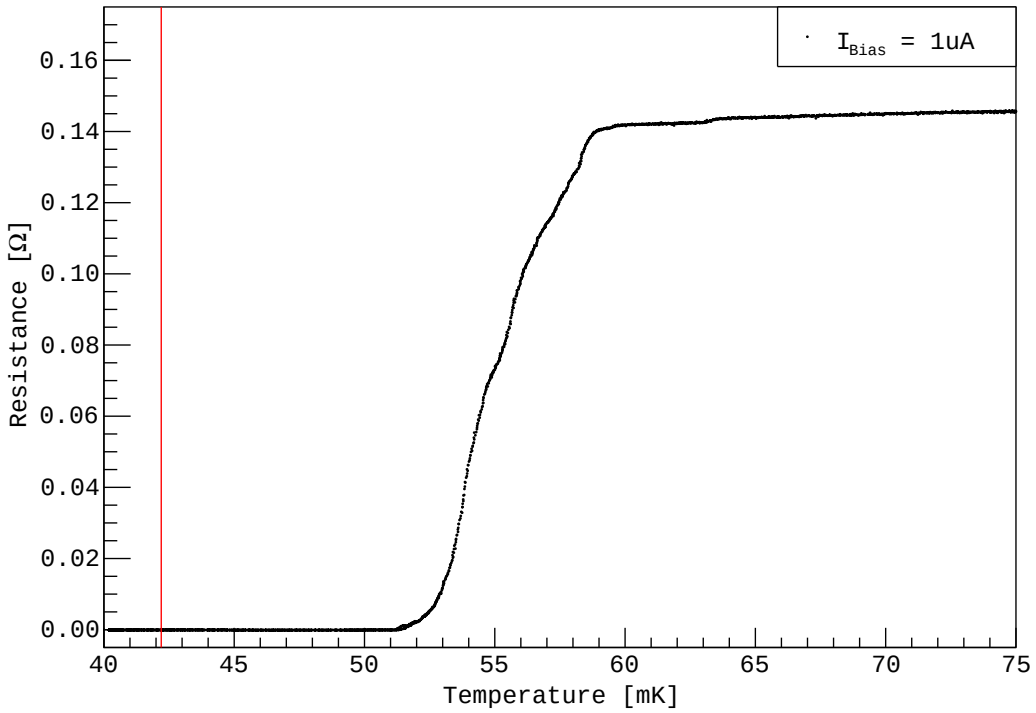

Figure 5.10: The super-to-normal-conducting transition of the TES used to measure the heat signal from the TeO_2 phonon-detector *Si591D* is shown. The transition curve is measured with a bias current of $1\,\mu A$. The red line indicates the temperature ($\sim 42\,mK$) used to stabilize the detector holder during the measurements discussed in this work.

Energy Calibration

The energy calibration of the TeO_2 phonon detector is performed using various γ lines present in the pulse height spectra of the measurements performed with the ^{228}Th γ calibration source. The source is placed outside the cryostat in the source lift between the liquid helium dewar and the lead shielding (as discussed in section 5.1, see also figure 4.4) at approximately the same height as the TeO_2 crystal. The distance between the source and the crystal is $\sim 30\,\text{cm}$ and the total activity of the source is $\sim 30\,\text{kBq}$. Due to the small solid angle covered by the crystal and the cryostat parts which are located between the source and the detector, the event rate in the TeO_2 crystal was only $\mathcal{O}(5\,\text{Hz})$.

The calibration source provides several γ lines which are used for the calibration: 583 keV, 861 keV and 2614 keV of ^{208}Tl and the 727 keV line of ^{212}Bi. Furthermore, the single escape peak (SEP) of ^{208}Tl at 2104 keV is used for the calibration. Due to the relatively low energy resolution of the detector, the double escape peak (DEP) of ^{208}Tl at 1593 keV and the 1620 keV γ line of ^{212}Bi cannot be separated and, therefore, this peak is not used for the calibration. Additionally, the 511 keV line, originating from γs which cause pair-production in the material surrounding the crystal, can be used for the calibration[18]. The energies of all γ lines are taken from [130].

Figure 5.11 shows several pulse height spectra[19] in the energy interval around the individual γ peaks as well as the results of gaussian fits performed to determine the mean pulse height corresponding to the individual γ lines. The background to the individual γ peaks is modeled by: an exponential in the fit performed to determine the mean pulse height corresponding to the peaks at 511 keV, 583 keV, 727 keV, and 861 keV, and the full energy peak of the 2614 keV γ line (^{208}Tl). For the single escape peak (corresponding to the 2614 keV γ line) at 2104 keV, a flat background is assumed. The mean pulse heights obtained by the fit are given in table 5.1. Figure 5.11 also shows the corresponding fit results.

Figure 5.12 shows the pulse heights obtained from the γ calibration measurement (see figure 5.11) versus the respective γ energy of the different γ-lines

[18] The data corresponds to the measurement discussed in section 5.6 where also an ^{147}Sm α source was present below the phonon detector. Events induced by this source add a constant offset to the spectrum below $\sim 2.3\,\text{MeV}$ but do not affect the peak positions of the γ lines.

[19] The pulse height is obtained from a template fit on the raw data (see section 5.4).

	E_γ [keV]	$\langle x \rangle$ [Ch]
e^-/e^+	511 keV	1821.6 ± 1.2
^{208}Tl	583 keV	2073.9 ± 0.7
^{212}Bi	727 keV	2591.5 ± 2.5
^{208}Tl	861 keV	3072.2 ± 4.1
^{208}Tl SEP	2104 keV	7532.2 ± 8.1
^{208}Tl FEP	2614 keV	9334.0 ± 2.0

Table 5.1: Mean pulse heights $\langle x \rangle$ in the phonon detector corresponding to the individual γ-lines. The values are obtained from the fits shown in figure 5.11.

used for the energy calibration. The data points are fitted using a linear function $y = p_0 + p_1 \cdot E$. The relative deviations of the data points from the fit function are also shown in figure 5.12 (bottom panel). The following parameters are obtained from the fit:

$$p_0 = -8.1 \pm 1.9\,[\text{Ch.}]$$
$$p_1 = 3.574 \pm 0.002\,[\text{Ch./keV}]$$

The detector shows a linear response in the energy range relevant for the measurements performed in this work ($\mathcal{O}(0 - 3000\,\text{keV})$).

Figure 5.13 shows an energy spectrum obtained with the $20 \times 20 \times 10\,\text{mm}^3$ TeO_2 crystal with logarithmic scale. The events depositing energies larger than $\sim 3\,\text{MeV}$ in the crystal are caused by muon interactions in the crystal or the cryostat[20].

The relative detector resolution at the full energy peak of the 2.614 MeV γ-line of ^{208}Tl is $\sim 2.5\%$ (FWHM, corresponding to $\sim 66\,\text{keV}$) and is by a factor of ~ 10 lower than the energy resolution achieved by the CRESST experiment with $CaWO_4$ crystals and TES readout [131]. Possible explanations for this behavior are a poor glue-interface between the crystal and the silicon TES

[20]Within the present work, the detectors are operated in a shallow underground laboratory where a muon flux of $\mathcal{O}(20/(m^2 s))$ is observed [110]. This leads to a high trigger rate of the muon veto system ($\gtrsim 300\,\text{Hz}$), and, therefore, the identification of muon-induced events could not be performed reliably in the energy range below $\sim 3\,\text{MeV}$ where a large number of events is present. However, the veto system can be used to identify $\gtrsim 98\%$ of all events above 3 MeV, where only few events are present, to be coincident with events in the muon veto system. Refer to [111] for a description of the muon veto system.

carrier substrate or an acoustic mismatch between the crystal material (TeO_2) and the carrier material (Si), caused by the different Debye temperatures of silicon and TeO_2 (see [66] for a discussion of the acoustic mismatch in cryogenic detectors with directly evaporated TES.)[21].

[21] Since only one TeO_2 crystal and only one TES with a transition temperature matching matching that of the light detector (*Si593D*) were available for the measurements performed in this work, no further tests could be performed.

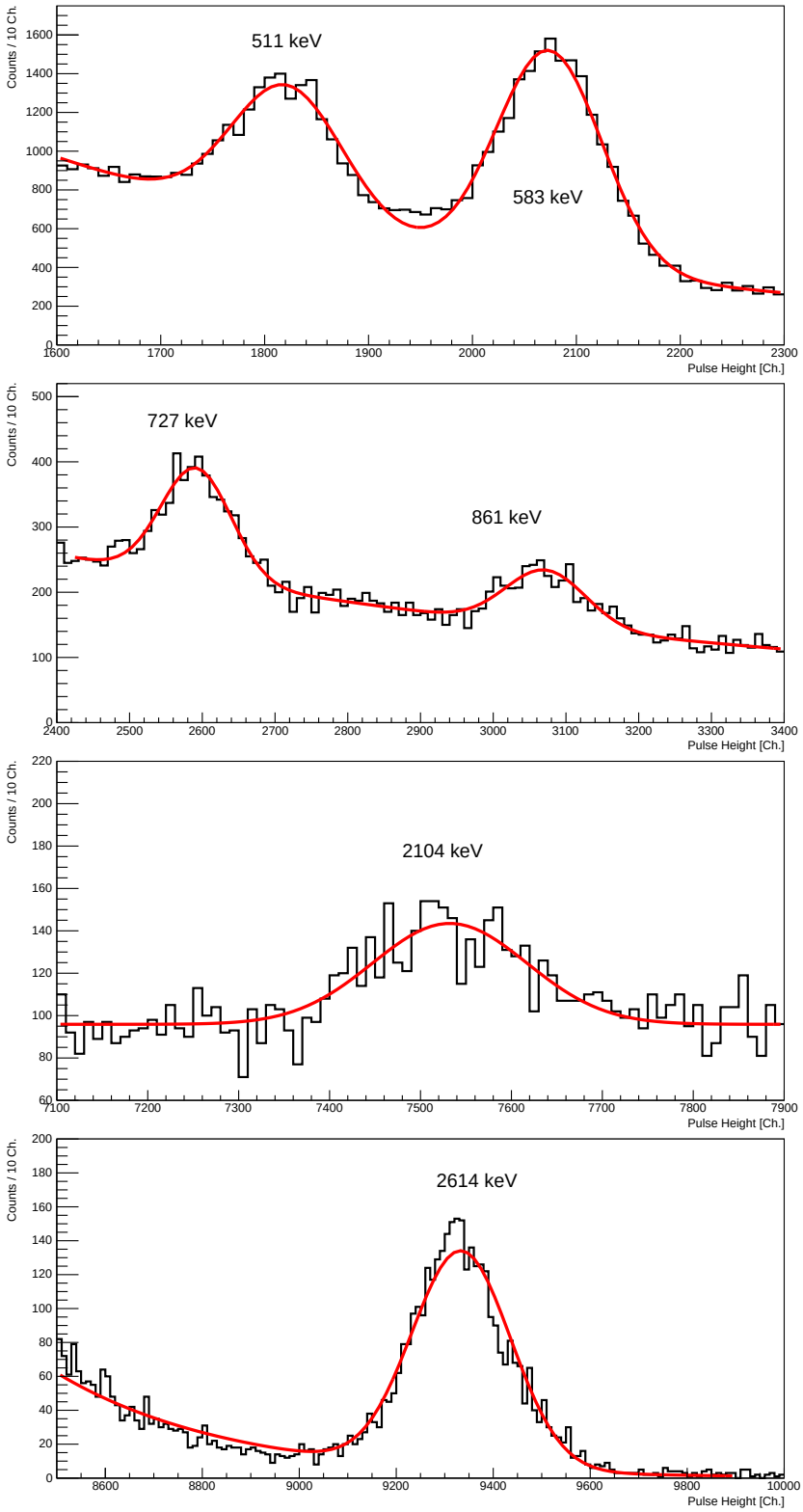

Figure 5.11: These plots show the results of the fits performed to determine the pulse heights of the individual γ-lines recorded in the TeO_2 phonon detector. The pulse heights obtained from these fits are given in table 5.1. The models used to describe the backgrounds to the individual peaks are given in the main text.

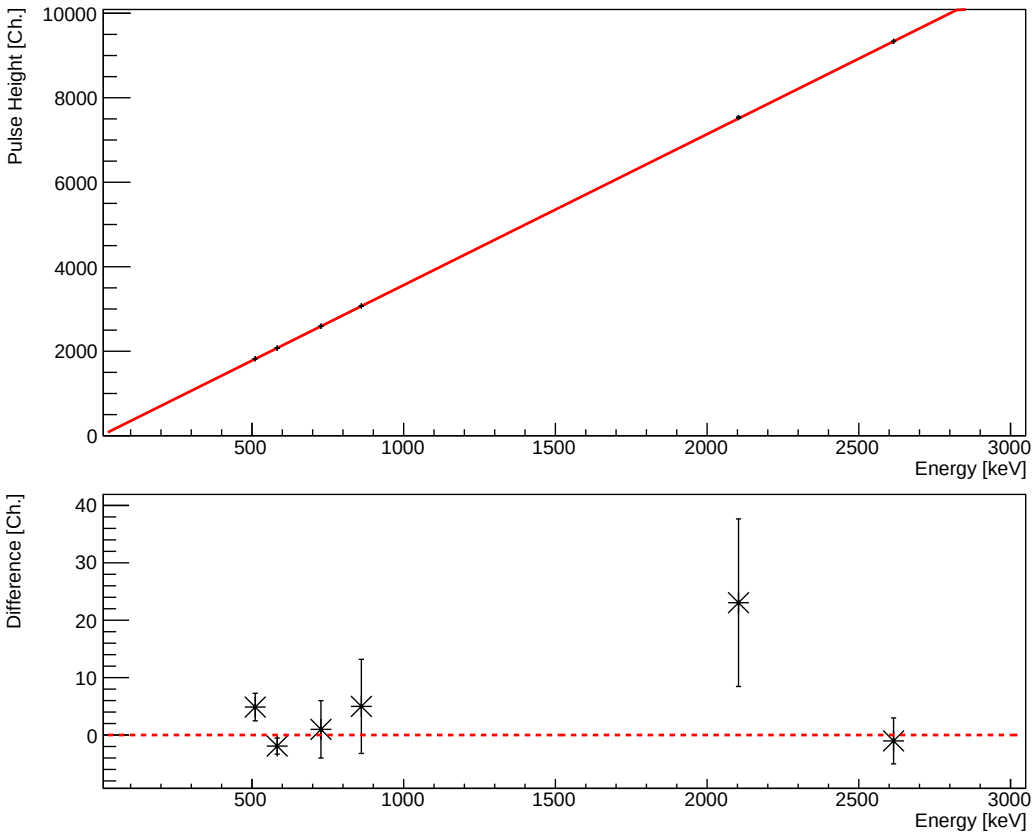

Figure 5.12: Top panel: Mean pulse heights corresponding to the various γ lines versus their respective energy. The error bars are too small to be visible. The data points are fitted using a linear function $y = p_0 + p_1 \cdot E$, shown as a red line in the plot. The results of the fit are given in the main text. **Bottom panel:** Deviations (in channels) of the data points from the values expected from the fitted function which is indicated by the dashed red line. The detector shows a linear response in the energy range relevant for the measurements performed in this work ($0 - 3000\,\mathrm{keV}$).

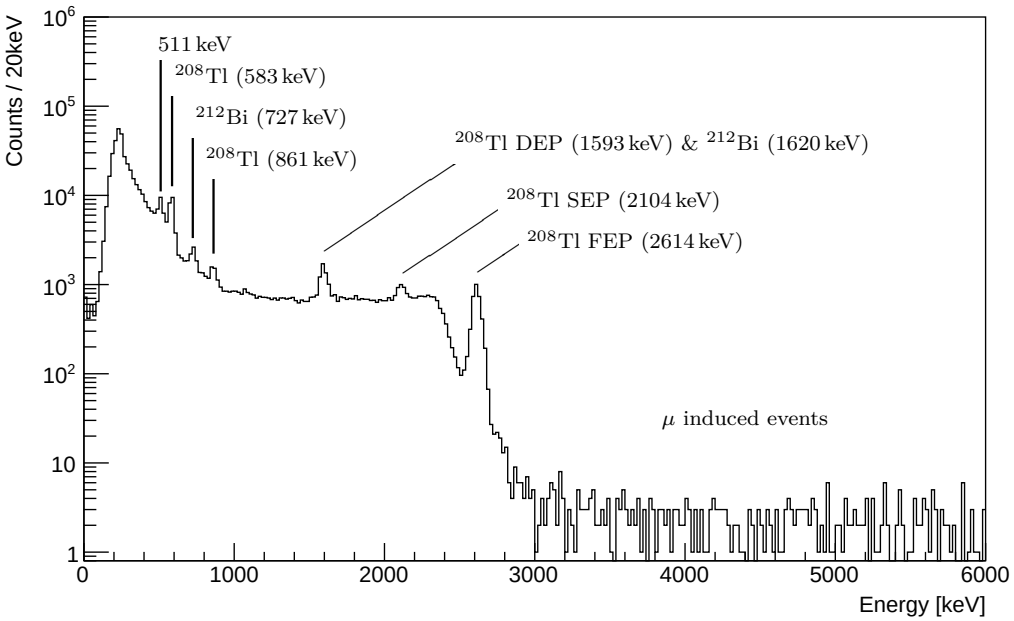

Figure 5.13: Energy spectrum measured with the TeO_2 crystal using an external ^{228}Th source. The relative detector resolution at the full energy peak of the 2.614 MeV γ-line of ^{208}Tl is $\sim 2.5\%$ (FWHM, corresponding to ~ 66 keV). This spectrum also contains events from the ^{147}Sm source, however, the contribution of these events to the spectrum can be neglected due to the low rate emitted by the α source ($\mathcal{O}(0.1\,\text{Hz})$) compared to the ^{208}Tl γ source ($\mathcal{O}(5\,\text{Hz})$). Several γ lines can be identified as well as the single- and double-escape peaks (SEP and DEP, respectively) and the full energy peak (FEP) of the 2.614 MeV γ-line of ^{208}Tl. The events above 2.614 MeV γ-line are induced by muons passing through the setup.

5.4 Data Analysis

In this section, the analysis of the obtained raw data will be described. For the cryogenic detectors used in this work it is generally assumed that the pulse height (x) of the heat signal is a measure for the deposited energy (E), i.e., $x \propto E$. The heat signal induced by a particle interaction and measured with the TES is superimposed by electronic and microphonic noise present in the measurements[22]. Since the frequency spectrum of the noise present in the recorded data is almost flat (compare discussion in [119]), the recorded samples can be assumed to be independent of each other and the recorded raw data can be analyzed using the template fit described in [119]. This fit is performed in order to determine the pulse height of the heat signal from the recorded data by fitting a template pulse, which is obtained by averaging similar recorded pulses, to the raw-data pulses.

Since the signals studied in the present work lead to correlated signals in both low-temperature detectors of the detector module (i.e., the heat signal induced by particle interactions in the TeO_2 crystal and the heat signal induced by the Cherenkov light absorbed in the cryogenic light detector) a simultaneous template fit of both detectors is performed. A dedicated software developed in [119] to analyze the raw signals recored with the data acquisition system described in section 4.3.4 has been extended in the present work to perform the template fit simultaneously on the raw data of two detectors.

The template pulses used to analyze the measurements with the low-temperature detector module discussed within the present work are generated using events from the same set of events[23] obtained from the full energy peak of the 2614 keV γ line (^{208}Tl). Basic quality cuts (comparable to the cuts described in [119][24]) are applied to the raw data and pulses of similar amplitude and shape (determined by the decay time of the pulses) are averaged to obtain the template pulse. Figure 5.14 shows template pulses from the measurement with applied NL voltage (see section 5.6)[25]. In order to obtain the pulse height from the template fit, the template pulses are normalized to unity.

[22] The electronic noise is due to the pickup of high-frequency electronic signals in the measurement electronics while the microphonic noise originates from mechanical vibrations ob the setup, e.g., due to vibrations of the pumping lines.

[23] Since the simultaneous measurement of the phonon and the light signal leads to a time correlation between the events in both detectors, the template pulses have to be generated from the same set of events.

[24] Since the detectors operated within the present work differ from the detector used in [119], the absolute values of the applied cuts are different.

[25] For each measurement, individual template pulses are created.

The template fit is performed with the goal of obtaining the pulse height of the heat signal from the raw data. The free parameters of the fit are a shift[26] of the position of the template pulse along the time axis to account for trigger walk due to the filtering of the trigger signal (see section 4.3.4), an offset of the template to account for an incorrect determination of the baseline[27], and the amplitude of the template pulse which gives the pulse height of the heat signal. For a certain shift of the template pulse, the χ^2 of the fit is minimized to find the corresponding pulse height and offset (see description of the fit in [119]). The optimal shift of the template pulse is determined by minimizing the χ^2 values obtained for each individual shift [119]. Since the signal in the phonon channel is much larger compared to the signal in the light channel (see, e.g., figure 5.15), the shift of both channels is determined by using the optimal shift determined for the phonon channel. For the amplitude and offset of the light channel, the values corresponding to this shift are used. The result of such a template fit is shown in figure 5.15 which depicts a typical event induced by the deposition of the full γ energy of the 2614 keV γ line (^{208}Tl). Spurious and unphysical events (i.e., electronic noise in the acquired data, pile up, events containing SQUID resets) are removed by applying basic data quality cuts to the data of both channels. Furthermore only well fitted events, based on the goodness-of-fit (χ^2), are accepted [119].

The parameters obtained for the template fit shown in figure 5.14 are given in table 5.2.

Fit parameter	TeO_2 phonon detector	NL light detector
Pulse height [Ch.]	9237.1 ± 11.4	482.6 ± 3.2
Offset [Ch.]	35.3 ± 4.9	-25.4 ± 0.8

Table 5.2: Fit parameters obtained for the template fit shown figure 5.14.

This method is used to process the raw data of the measurements where both detectors of the cryogenic detector module are operated simultaneously. For the LED calibration measurements, no simultaneous fit is performed.

[26]The shift is given in units of pulse samples, the time between individual samples is determined by the sampling rate of the DAQ system.

[27]The signals have a varying constant offset (compare section 4.3.4) which is removed in the analysis of the data by subtracting the mean value of the baseline (typically determined from the first 15 % of the pulse) from the raw signal, thereby setting the baseline to zero.

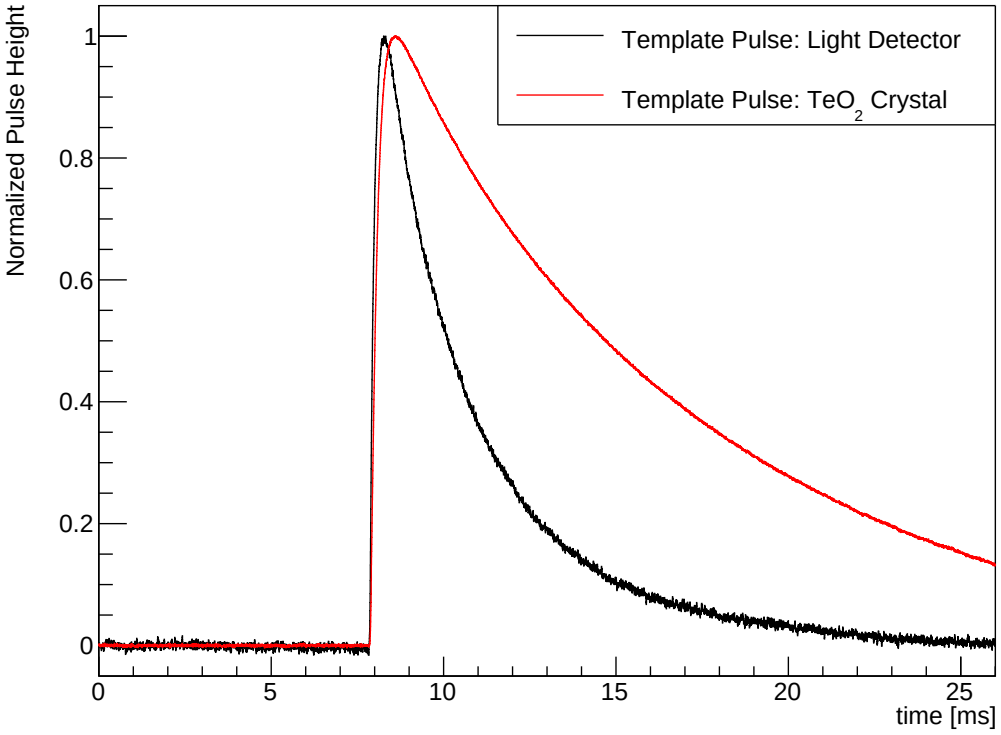

Figure 5.14: The templates pulses of both the phonon detector (red line) and the light detector (black line) for the measurements discussed in section 5.6. Both template pulses are obtained (using the same set of events) from the full energy peak of ^{208}Tl. Basic quality cuts (comparable to the cuts described in [119]) are applied to the raw data of both detectors. Pulses of similar shape are selected via their respective decay time. For each measurement, individual template pulses are generated. To extract the pulse height from the template fit, the template pulses are normalized to unity.

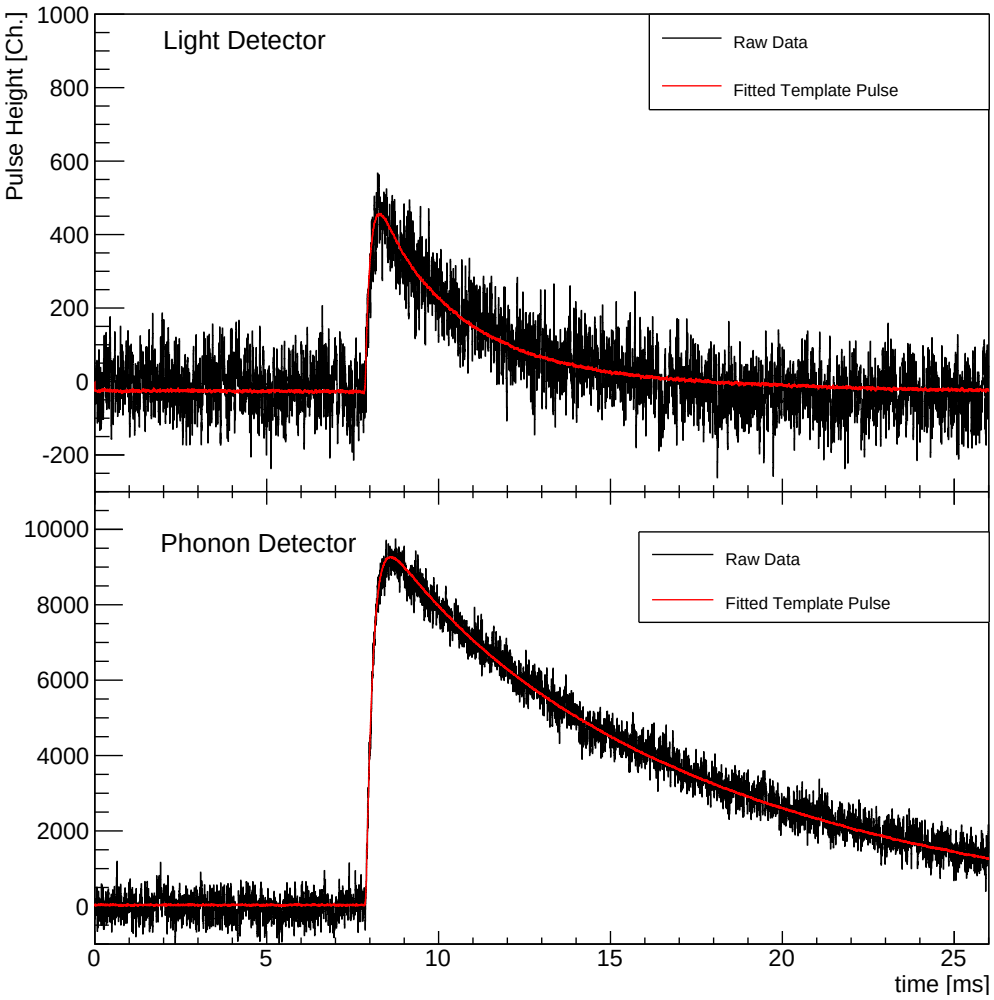

Figure 5.15: This figure shows the raw pulses of the light detector (**top**) and phonon detector (**bottom**) for a $\sim 2600\,\mathrm{keV}$ γ-induced event in the detector module shown in figure 5.1. The light detector is operated with a NL voltage of $V_{NL} = 70\,\mathrm{V}$ applied between the electrodes. The red line in both plots shows the result of a template fit which is performed for both channels simultaneously. The free parameters of the fit are a shift of the template position along the time axis, a constant offset, and the amplitude of the fitted template. The pulse parameters obtained from the fit are given in the main text.

5.5 Measurement without Applied Neganov-Luke Voltage

In order to evaluate whether a separation between α and e^-/γ induced events is possible when the NL light detector is operated without applied NL voltage, a $\sim 16\,h$ measurement with the detector module described in section 5.1 has been performed. The detector module is irradiated by both a ^{228}Th γ source and a ^{147}Sm α source (see section 5.1).

Figure 5.16 shows a 2-dimensional histogram of the energy calibrated pulse heights for the events (in the NL light detector and the TeO_2 phonon detector) acquired in this measurement[28]. The color coding of the histogram corresponds to a logarithmic scale in order to allow a better visualization of the events above $\sim 1\,MeV$ where only a relatively low count rate is observed. In the figure, an inclined band of γ-induced events extending up to the $2.614\,MeV$ γ-line and above this γ line, μ-induced events can bee seen. The slope of this band is due to the Cherenkov radiation detected for these events. Furthermore, the double escape peak (at $\sim 1592\,keV$) corresponding to the $2.614\,MeV$ γ line of ^{208}Tl can be seen. The other γ-lines induced by the ^{228}Th source can only be vaguely identified (see section 5.3.2 for an energy spectrum of the phonon detector). The plot furthermore contains α-induced events from the ^{147}Sm source with a maximal energy of $2.3\,MeV$. Due to the low intensity of the α source[29], these events cannot be clearly identified.

In order to study the suppression efficiency of α from e^-/γ induced events based on the amount of Cherenkov radiation detected for these events, two reference regions[30] are defined for which the signal in the light detector will be studied further. An α reference region between 2000 and $2300\,keV$ and a pure e^-/γ-reference region (from $2581\,keV$ to $2647\,keV$) corresponding to the full width at half maximum (FWHM) of the full energy peak (FEP) of the

[28]For the LED calibration corresponding to this measurement values very similar to the calibration without applied NL voltage described in section 5.3.1 were obtained ($\sigma_0 = 16.28 \pm 0.17$ and $a = 0.96 \pm 0.02$). The width of the baseline in the light detector during this measurement amounts to $\sigma_{BL} = 15.2 \pm 0.3\,Ch$.

[29]The expected rate of α-induced events ($\mathcal{O}(0.1\,Hz)$) is much smaller compared to the rate of γ-induced events ($\mathcal{O}(5\,Hz)$).

[30]The reference regions are chosen based on the measurement with applied NL voltage discussed in section 5.6. The upper limit of the α reference region corresponds to the energy of the α particles emitted in the decay of ^{147}Sm while the lower limit of this reference region is chosen to maximize the number of α events in this region while simultaneously preventing a strong overlap with the e^-/γ events from this region.

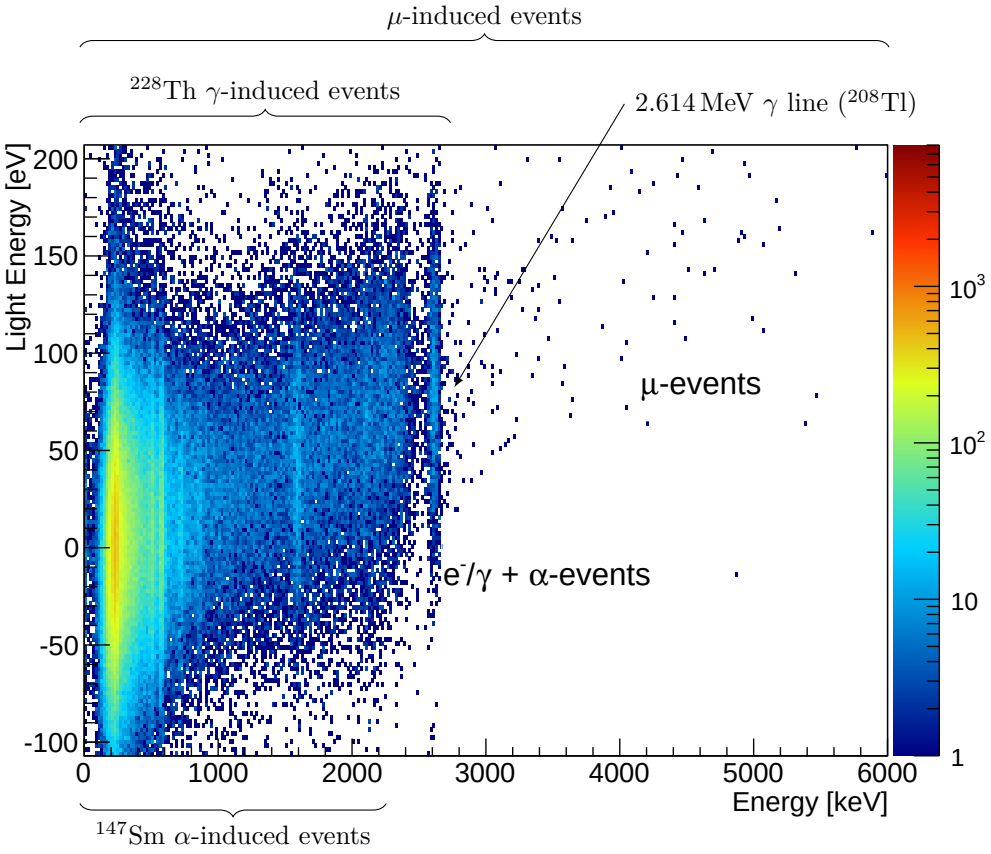

Figure 5.16: A 2-dimensional histogram of the energy-calibrated data (pulse heights in the phonon and light detector) obtained during a $\sim 16\,\mathrm{h}$ measurement with a TeO_2 phonon detector and a NL light detector (see section 5.1). The light detector was operated without a voltage applied between the aluminum electrodes. Basic data quality cuts have been applied to the data (comparable to the cuts described in [119]). The spectrum contains events from a ^{147}Sm α source, placed directly below the TeO_2 crystal, events from a ^{228}Th γ calibration source, placed outside the cryostat, and muon-induced events which are visible above the 2614 keV γ line. No separation between the α- and γ-induced events is possible under these conditions. See also [55].

2614 keV γ line (^{208}Tl) . The α reference region is expected to contain events from the ^{147}Sm source as well as from the Compton continuum induced by the individual γ lines emitted from the ^{208}Tl source while the e^-/γ reference region is expected to contain only γ-induced events.

Figure 5.17 shows the distribution of the energy detected in the light detector for the two reference regions. The distribution of the amount of Cherenkov radiation detected within the e^-/γ reference region is fitted using a single normal distribution (red histogram and line in figure 5.17). Due to the detector resolution and the significantly lower count rate of α-induced events[31], the individual contributions to the α reference region cannot be disentangled. Therefore, the α reference region is also fitted using only a single gaussian function (black histogram and line in figure 5.17)[32]. The signal in the light detector, corresponding to the Cherenkov radiation detected in both reference regions is well described by the respective fit functions. The results of the individual fits are given in table 5.3. Furthermore, since the α-induced events are expected to give rise to a continuous energy spectrum between $0 - 2300$ keV, the contribution due to α events cannot be clearly identified. Such an identification would be possible with a crystal which has an intrinsic α contamination since in this case, the α-induced events would give rise to a distinctive line (compare discussion in section 5.2).

From these results it can be concluded that, under these conditions, no separation between α and e^-/γ-events is possible and a light detector with a higher sensitivity is required, i.e., with a lower energy threshold and an improved energy resolution.

In chapter 3 it was shown that the amount of Cherenkov radiation detected at the FEP of the 2.614 MeV γ-line (^{208}Tl) can be used as an indicator for the expected amount of Cherenkov radiation produced by the two electrons emitted in the $0\nu\beta\beta$ decay of ^{130}Te. Since no Cherenkov light is expected to be produced by the α-induced events in the TeO_2 crystal, it is assumed that the distribution of the signal in the light detector for α-induced events in the α-reference region can be extrapolated up to the endpoint of the $0\nu\beta\beta$ decay at $Q_{\beta\beta} = 2.53$ MeV.

As will be shown in section 5.6, the individual distributions (α and e^-/γ) in the α reference region can, however, be separated when the light detector is

[31] The respective rates are $R(e^-/\gamma) = \mathcal{O}(5\,\text{Hz})$ and $R(\alpha) = \mathcal{O}(0.1\,\text{Hz})$.

[32] For this region, a fit with two gaussian functions could not be performed reliably.

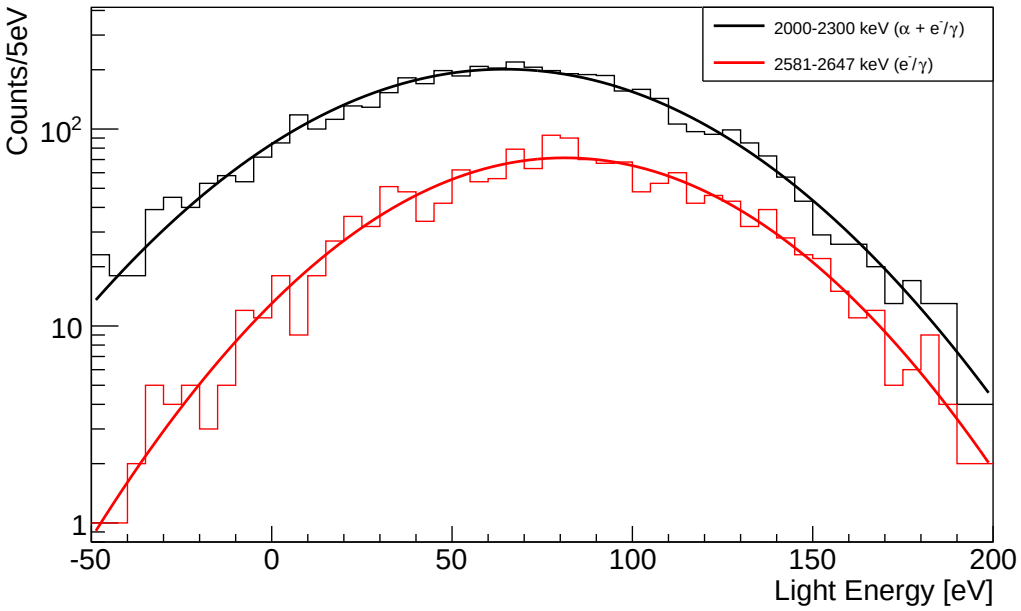

Figure 5.17: This plot shows the results of a fit to the energy detected in the light detector for the α reference region between 2000 and 2300 keV (black histogram and line) and the e^-/γ reference region (red histogram and line) corresponding to the full width at half maximum of the full energy peak of the 2614 keV γ line (^{208}Tl). This measurement was performed with no NL voltage applied between the aluminum electrodes, the corresponding 2-dimensional histogram for this measurement is shown in figure 5.16. Both reference regions are fitted using a single normal distribution. The results of these fits are given in table 5.3. In the α reference region, the contribution due to α events cannot be distinguished from e^-/γ induced events and therefore no separation of these events is possible. As can be seen in figure 5.20, these events can be separated when the light detector is operated with a NL voltage of $V_{NL} = 70$ V applied between the electrodes. See also [55].

	ΔE [keV] (reference regions)	x_0 [eV]	σ [eV]
α & e^-/γ	$2000 - 2300$	64.6 ± 0.7	48.8 ± 0.6
e^-/γ (FEP)	$2581 - 2647$	81.2 ± 0.9	44.0 ± 0.9

Table 5.3: Values obtained for the mean x_0 and the standard deviation σ of the individual normal distributions fitted to the light-energy distributions for the measurement performed without applied NL voltage (shown in figure 5.17). ΔE gives the energy range in the phonon detector used to define the individual reference regions.

operated with an applied NL voltage. This is due to the reduced threshold of the light detector when operated with NL voltage (see section 5.3.1).

5.6 Measurement with Applied Neganov-Luke Voltage

In the previous section it was found that a separation between α and e^-/γ induced events is not possible given the observed energy threshold of the light detector when operated without applied NL voltage.

However, as has already been shown in section 5.3.1, the threshold and energy resolution of the cryogenic light detector at low light-energies increases significantly when the detector is operated with a NL voltage applied between the aluminum electrodes. In order to further study the effect of this increased light detector sensitivity on the background suppression capabilities of a cryogenic detector module with a TeO_2 crystal and a NL light detector, a measurement similar to the measurement described in the previous section has been performed.

During the measurement described in this section, the ^{228}Th γ source as well as the ^{147}Sm α source (compare section 5.1 and section 5.2 for the position of the γ source and a description of the α source) were irradiating the detector module. The light detector was operated continuously for $\sim 42\,\mathrm{h}$ with a Neganov-Luke voltage of $V_{NL} = 70\,\mathrm{V}$ applied between the electrodes. This measurement also marks the first time a cryogenic NL amplified light detector has been operated continuously for such extended periods without

being regenerated (compare, e.g., previous measurements performed in [60] where NL amplified light detectors have been operated continuously without regeneration for measuring times of $\mathcal{O}(1-2\,\mathrm{h})$).

In the following details of this measurement as well as the results will be discussed.

5.6.1 Reduction of the Neganov-Luke Amplification

As already discussed in section 5.3.1, the Neganov-Luke light detector used for the measurements performed in the present work exhibits a reduction of the thermal gain with time when operated with applied Neganov-Luke voltage. Figure 5.18 shows a plot of the pulse height in the light detector for events in the full energy peak of the 2.614 MeV γ line of ^{208}Tl (FWHM) versus the corresponding time stamp of the event during a $\sim 42\,\mathrm{h}$ measurement. The reduction of the pulse height, caused by a reduction of the thermal gain which is explained by an accumulation of charge carriers in the vicinity of the aluminum electrodes (compare, e.g., [59, 61]), can be clearly seen.

To describe this reduction of the thermal gain with time, the data points[33] are fitted using a linear function of the form $A(t) = A_0 + p_{decr} \cdot t$, where A_0 is the initial pulse height of these events at the beginning of the measurement and p_{decr} is the decrease per unit time. The following parameters have been obtained from the fit:

$$A_0 = 403.1 \pm 0.1\,[\mathrm{Ch.}]$$
$$p_{decr} = -0.769 \pm 0.005\,[\mathrm{Ch./h}]$$

Under the present measurement conditions, the reduction of the pulse height of the signals in the light detector amounts to $\sim 8\%$ during the 42 h measurement[34].

[33] The error of the pulse height is obtained from the template fit (compare section 5.4).

[34] It should be noted that the reduction of the signal amplitude determined here can not be directly compared to the measurement described in section 5.3.1 since the experimental conditions were different: In the present measurement, the event rate as well as the average amount of light detected for each event are significantly smaller than in dedicated measurement performed where only the LED was used to irradiate the light detector. Furthermore, in the measurement discussed here, also the ^{228}Th γ source is irradiating the light detector directly in addition to the Cherenkov radiation detected from the TeO_2 crystal. A direct energy deposition due to γ radiation can cause the generation of a large number of free charge carriers which can then lead to a faster reduction of the thermal gain.

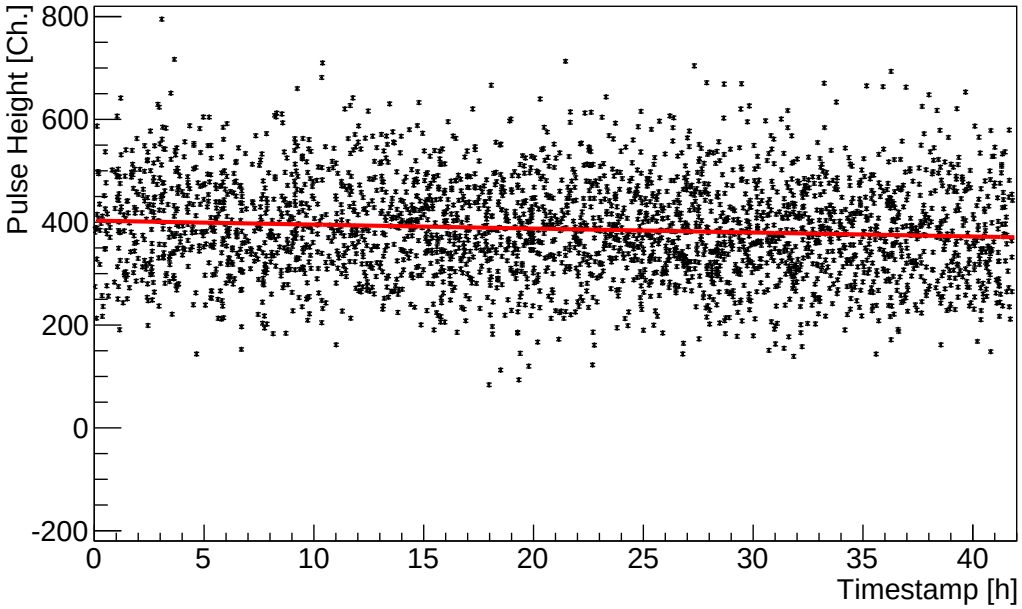

Figure 5.18: This plot shows the time dependence of the pulse height in the light detector for the full energy peak of the 2.614 MeV γ line of ^{208}Tl. The pulse height decreases by $\sim 8\%$ over the course of the ~ 42 h measurement due to a reduction of the Neganov-Luke amplification. This reduction of the thermal gain with time is explained by an accumulation of charge carriers in the vicinity of the aluminum electrodes. The red solid line shows a linear fit to the data points. See the main text for a discussion of this fit and the reduction of the pulse height.

This reduction of the pulse height effectively leads to a reduction of the signal-to-noise ratio which in turn leads to a reduced separation between α- and e^-/γ-induced events and limits the measurement time in which a certain separation between the individual kinds of events can be achieved (see section 5.7 for the determination of the suppression efficiency between these events). The initial thermal gain of the light detector can be restored by regenerating the detector as described in [59, 60] (i.e by switching off the NL voltage and flushing the detector with photons from an LED, thereby removing the accumulated charge carriers). Since the detector used for the present measurements shows a significantly improved performance with respect to the reduction of the thermal gain with time compared to the measurements performed in [59, 60], no measurement over multiple regeneration cycles were performed in this work.

As discussed in [59], such a reduction of the thermal gain can in principle be taken into account by correcting the pulse heights according to a fit function describing the reduction of the pulse height of the signal in the light detector with time(e.g., the fit shown in figure 5.18). However, since the measurement discussed in this section is performed with the goal of discriminating events which produced light (i.e., e^-/γ-induced events) from events which are expected to produce no light (i.e., α-induced events), such a correction is not practical since the suppression capabilities are based on the achieved signal-to-noise ratio. This is due to the fact that the correction of the pulse heights can not increase the signal-to-noise ratio and therefore cannot improve the separation between these different kinds of events.

5.6.2 Energy Calibration of the Light Detector with Applied Neganov-Luke Voltage

As discussed in section 5.3.1, an energy calibration of the NL light detector when operated without applied NL voltage, can be performed using the LED calibration technique. In addition, a method for deriving the energy calibration for measurements performed with applied NL voltage was introduced in section 5.3.1.

This method can be applied to measurements where the spectrum of the wavelengths emitted by the LED matches the spectrum detected from, e.g., a scintillating crystal. However, in the measurements discussed in the present

work, the average wavelength of the Cherenkov radiation detected from the TeO_2 crystal is likely to be different from the average wavelength in the calibration measurement performed with an LED[35]. This fact also influences the observed thermal gain (which depends on the average number of electron-hole pairs drifted in the electric field generated by the NL voltage) in the measurement where Cherenkov radiation emitted from the electrons within the TeO_2 crystal is detected compared to the LED calibration measurement.

In the measurement discussed here, the thermal gain in the light detector for signals induced by Cherenkov radiation emitted from the TeO_2 crystal is determined using the average pulse height in the light detector for events in the full energy peak of the 2.614 MeV γ line of ^{208}Tl (FWHM) as a reference point. In this case, a thermal gain of ~ 14.8 at the beginning of the measurement is determined by comparing the average pulse height of the detected Cherenkov light with and without applied NL voltage. For this measurement, the energy calibration of the light detector operated without NL voltage (obtained using the LED calibration technique described in section 5.3.1) is corrected accordingly. Therefore, the conversion factor between pulse height and the corresponding energy (see equation (5.13)) is calculated using the thermal gain of the detected Cherenkov radiation.

It has to be noted furthermore that, in order to determine the suppression efficiency between α and e^-/γ events, an absolute energy calibration of the light detector is not required.

5.6.3 Results

A 2-dimensional histogram of the energy-calibrated pulse heights of the cryogenic light detector versus the TeO_2 phonon detectors (the pulse heights are obtained by fitting the raw data with a template fit as described in section 5.4) of the events acquired in the measurement described in this chapter is shown in figure 5.19. It can be seen that the distribution of events induced by the ^{228}Th γ source as well as muon-induced events (inclined band) can be clearly separated (already by eye) from the α induced events (horizontal band) at energies greater than ~ 2000 keV. A pure e^-/γ-reference region, corresponding

[35] This is due to the fact that the produced Cherenkov radiation follows a continuous spectral shape which has a wavelength dependence of approximately $\propto 1/\lambda^2$. In addition it has to be considered that the spectral shape of the Cherenkov radiation detected in the light detector, and therefore also the average detected wavelength, depends on the spectral response of the reflective foil, of the light absorber, and on the transmission of the TeO_2 crystal.

to the full width at half maximum (FWHM) of the full energy peak (FEP) of the 2614 keV γ line of ^{208}Tl (2581 keV to 2647 keV), is used. For the α reference region, an energy interval between 2000 keV (an energy where both the α and e^-/γ induced events can be separated by eye[36]) and 2300 keV (the maximal energy emitted in the α decay of ^{147}Sm within the source, compare section 5.2) is chosen.

Figure 5.20 shows the histograms of the energies detected in the light detector for both, the α and the e^-/γ reference region. In this measurement, where the light detector is operated with a NL voltage of $V_{NL} = 70$ V, the distributions of α and e^-/γ events within the α reference region can be described using two independent normal distributions characterizing the contributions due to α-induced events (black dashed line) and e^-/γ-induced events (black dotted line), respectively. The distribution of e^-/γ events from the full energy peak of the 2.614 MeV γ line of ^{208}Tl is fitted using a single normal distribution. The individual distributions are characterized by the mean energy detected in the light detector x_0 and their respective variance σ. The results of the fits to the individual reference regions are given in table 5.4.

	E [keV] (reference regions)	x_0 [eV]	σ [eV]
α-events	$2000 - 2300$	2.9 ± 0.3	7.1 ± 0.3
e^-/γ-events	$2000 - 2300$	65.6 ± 0.2	20.4 ± 0.2
e^-/γ-events	$2581 - 2647$	77.5 ± 0.3	19.5 ± 0.2

Table 5.4: Values obtained for the mean x_0 and the standard deviation σ of the individual normal distributions fitted to the light-energy distributions shown in figure 5.20. The energy ranges of the individual reference regions in the phonon detector are also given in the table. In comparison to the results obtained in the measurement with the light detector operated without applied NL voltage, it can be seen that in the present measurement with applied NL voltage, the reference region from $2000 - 2300$ keV can clearly be described by two normal distributions (corresponding to α and e^-/γ induced events, respectively).

Since the energy calibration of the light detector was performed with the thermal gain determined at the beginning of the 42 h measurement and a

[36] This lower limit of the α reference region was also chosen since it provides a sufficient number of events to perform a fit on the α events.

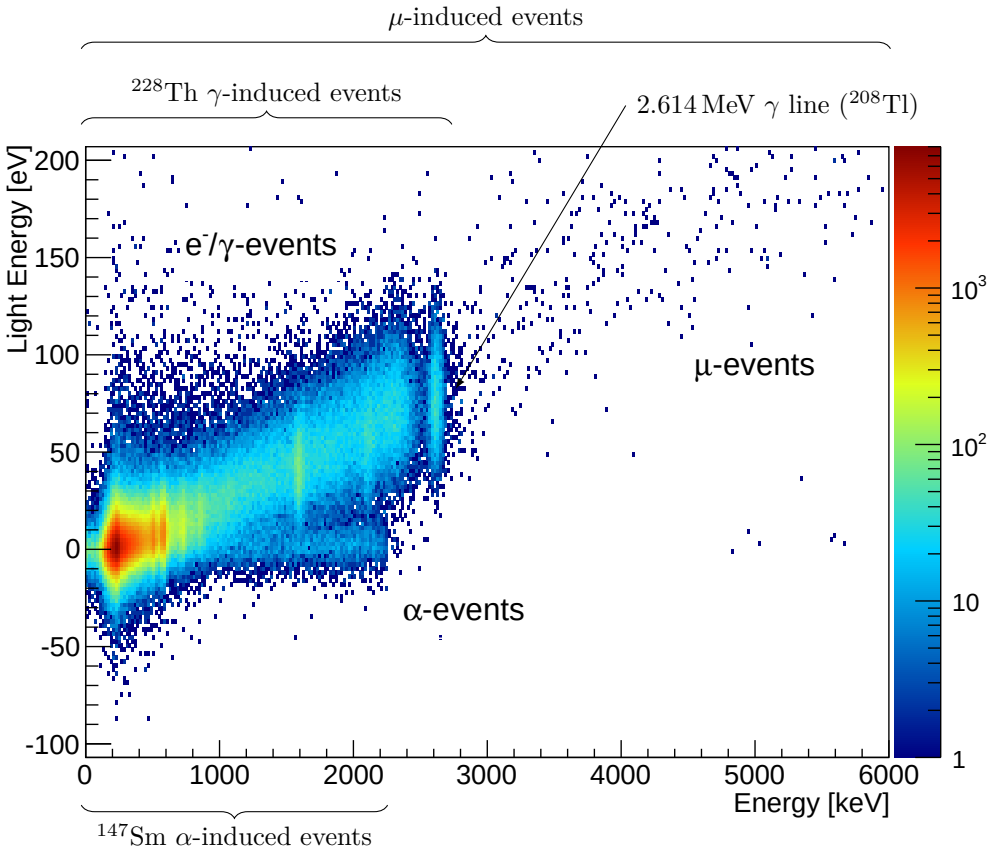

Figure 5.19: This figure shows a 2-dimensional energy spectrum of the events recorded with the detector module consisting of a $20 \times 20 \times 10\,\mathrm{mm}^3$ TeO_2 crystal and a NL amplified cryogenic light detector, operated with a NL voltage of $V_{NL} = 70\,\mathrm{V}$. A ^{228}Th source, placed outside of the cryostat, and a ^{147}Sm source, placed directly below the TeO_2 crystal, were irradiating the detector module (compare section 5.1). In this plot several kinds of events are visible: the inclined band consists mainly of γ events induced by the ^{228}Th source as well as muon-induced events which can be seen at energies above $\sim 3\,\mathrm{MeV}$ in the TeO_2 crystal. The horizontal band between $0 - 2300\,\mathrm{keV}$ contains α events induced by the ^{147}Sm source. To determine the discrimination efficiency between α-induced events an e^-/γ-induced events, two reference regions are defined. A pure e^-/γ region around the full energy peak of the 2614 keV γ line of ^{208}Tl and an α reference region between $2000 - 2300\,\mathrm{keV}$. The α region also contains e^-/γ events induced by the γ source. The distribution of the energy detected in the light detector for these regions is shown in figure 5.20. See also [55].

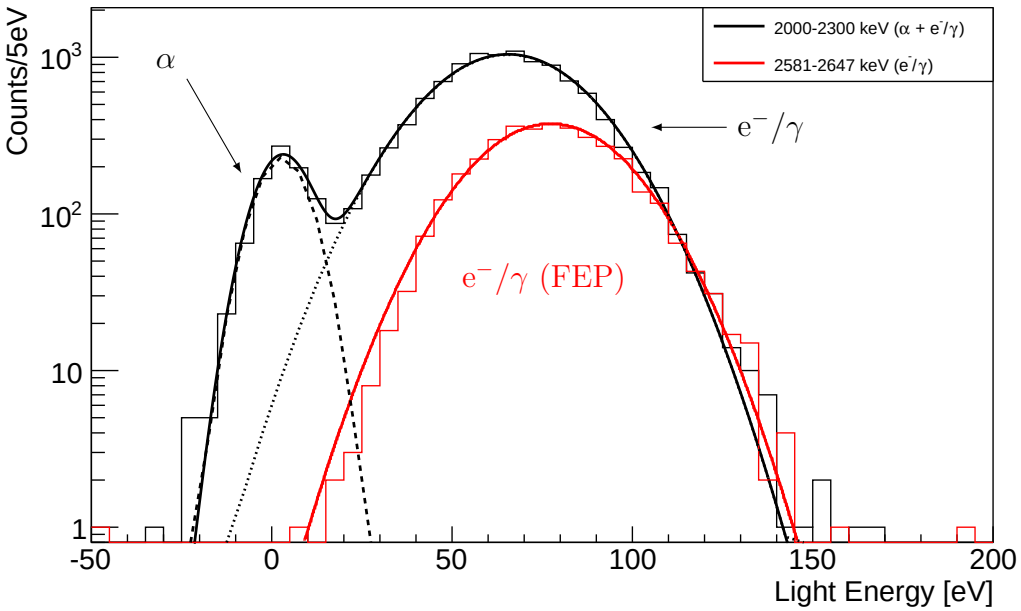

Figure 5.20: This plot shows the results of a fit to the distributions of the energy detected in the NL light detector for the e^-/γ reference region (red histogram and solid line) and of the energy detected for the α reference region (black histogram and dashed lines). In this measurement, the light detector was operated with a NL voltage of $V_{NL} = 70\,\mathrm{V}$ applied between the aluminum electrodes. The α reference region is fitted with two gaussian functions while the e^-/γ reference region is fitted with a single gaussian. The functions fit the respective spectra very well. The separation between α and e^-/γ-induced events will be discussed in section 5.7.

decrease of the gain by $\sim 8\%$ during this measurement is observed, this results in an apparent reduction of the average detected light energy. As a result, the mean light energy of the events in the e^-/γ-reference region (obtained from the gaussian fit) is slightly reduced with respect to the mean value obtained from the measurement performed without applied NL voltage.

It can be seen from the fit results given in table 5.4 that for the α-induced events an offset corresponding to a light energy of 2.9 eV is observed even though no Cherenkov radiation is expected to be produced for these events. The exact cause of this offset could not be determined. However, several indications point towards a correlated noise (or crosstalk) between the signals of the phonon and the light detector which leads to an offset when the data is analyzed with the correlated template fit:

- Since the signals in the phonon channel of these events, corresponding to an energy deposition between $2000 - 2300$ keV in the TeO_2 crystal, are much larger than the signals in the light channel (where no pulses are visible by eye), the fitted shift of the template fit (compare section 5.4) is determined using the phonon channel. Thus, the position of the template pulse in the light channel is fixed to the value obtained from the phonon channel and therefore the fit parameters in the light detector correspond to this shift. When the light channel is fitted independently from the phonon channel, a mean pulse height corresponding to zero is observed, i.e., no offset is present. Similarly, when empty-baseline events with no signal in both detectors (obtained from randomly-triggered events) are fitted, the mean pulse height of these events is compatible with zero.

- The width of the distribution of α-induced events corresponds to the width of the baseline obtained from the empty-baseline samples[37]. This indicates that in fact no photons were absorbed in the light detector for these events and just empty baselines were recorded. Otherwise, e.g., when one photon with an average energy of $E_{ph} = 2.9$ eV would have been absorbed, an increased width due to photon counting statistics would be expected. This is, however, not observed.

- A separate measurement where only the α source was present showed that the offset in the light channel is constant and energy independent.

[37] The width of the distribution of α-induced events in the light detector during this measurement amounts to $\sigma_\alpha = 35.1 \pm 1.2$ Ch while the baseline width (obtained from empty baseline samples) is $\sigma_{BL} = 34.9 \pm 0.4$ Ch. The broader baseline compared to the LED calibration measurement performed prior to this measurement is due to increased electronic noise, probably caused by the high-voltage power supply of the muon veto.

If a light production mechanism for α particles were present, this process would be expected to be energy dependent[38].

The fit parameters obtained from this measurement can now be used to determine the suppression efficiency between α-induced events from the α reference region and e^-/γ-induced events from the γ reference region. This will be discussed in the next section.

5.7 Determination of the α-Suppression Efficiency

An important aspect for experiments searching for the $0\nu\beta\beta$ decay of ^{130}Te with TeO_2 bolometers is a high signal acceptance in the region of interest (ROI) in a narrow ($\Delta E \approx 100\,\text{keV}$) energy interval around $Q_{\beta\beta}$ since any cuts on the data (i.e., to discriminate background events or to remove unphysical events) can also reduce the exposure of the experiment and consequently reduce the sensitivity to $T^{0\nu}_{1/2}$ (compare chapter 1). However, it is also crucial to significantly reduce the amount of background events in the ROI around $Q_{\beta\beta}$ to further increase the sensitivity to $T^{0\nu}_{1/2}$.

Therefore, an active background suppression technique, such as the method studied in this work, aiming to discriminate α-induced background from signal events on an event-by-event basis effectively has to fulfill two requirements: providing a high signal acceptance in the ROI while simultaneously discriminating a large amount of background events with high efficiency.

In this work, the discrimination efficiency between α and e^-/γ induced events, caused by the ^{147}Sm and ^{228}Th sources, respectively, is determined by the fit parameters obtained for the α- and e^-/γ reference region described in the previous section (see table 5.4).

For a certain signal acceptance (given in [%]) a corresponding acceptance threshold in the light detector can be calculated from the fit parameters obtained in the e^-/γ reference region[39] by using the cumulative distribution function (CDF) corresponding to the fitted normal distribution. Here, the signal acceptance threshold is chosen such that at least 99.8% of the events

[38] In general, light production processes such as scintillation or Cherenkov radiation are energy dependent.

[39] In an actual experiment searching for $0\nu\beta\beta$ decay, these parameters could also be obtained, as is done here, from an ^{228}Th γ calibration campaign.

within the full width at half maximum of the full energy peak of the 2614 keV γ line (^{208}Tl) are accepted. This corresponds to an energy which is 3σ below the mean of the light energy distribution of the Cherenkov radiation detected for the events in the e^-/γ reference region from $2581 - 2647$ keV. From the parameters given in table 5.4, a signal acceptance threshold[40] of 19.0 eV can be determined for the measurement with applied NL voltage.

The percentage of α events above this threshold (i.e., the leakage of α events into the signal region) can also be calculated using the parameters given in table 5.4. For the present measurement and a signal acceptance of 99.8% in the e^-/γ region, the number of α-induced events above this threshold is $\lesssim 1\%$. The distributions of the events recorded with applied NL voltage and the obtained acceptance threshold are shown in figure 5.21. These results show that the level of α-induced background events can be reduced by ~ 2 orders of magnitude by using the phonon-light technique.

The results of the measurements performed in this work show for the first time that an highly efficient event-by-event discrimination (i.e., providing a high signal acceptance and a large suppression of background events simultaneously) between α and e^-/γ induced events with energies close to $Q_{\beta\beta}(^{130}\text{Te})$ can actually be achieved by detecting the Cherenkov radiation emitted by electrons within the TeO_2 crystal [54] with NL amplified cryogenic light detectors.

Discussion

A highly efficient background suppression is particularly relevant for the next generation of $0\nu\beta\beta$-decay experiments with TeO_2 bolometers. In these experiments, the achievable sensitivity strongly depends on the background level in the region of interest (ROI) around $Q_{\beta\beta}$ (see, e.g., [132]). By the CUORE-0 (Cryogenic Underground Observatory for Rare Events) experiment [64], a level of α-induced background events of 0.019 cts/keV/kg/yr in the energy interval between 2.7 MeV and 3.4 MeV is reported. This α background is also expected to be present in the ROI around $Q_{\beta\beta}(^{130}\text{Te})$ at ~ 2.5 MeV.

Given the background level achieved by the CUORE-0 experiment, the CUORE experiment [44], anticipates an α-background level of the order of 0.01 cts/keV/kg/yr in the ROI (see, e.g., [64]) which is expected to be dominated by α-induced

[40] Only events with a light energy larger that the threshold value are accepted as "signal-like" (i.e., $\beta\beta$-like) events. Events with a light energy below this value are considered background events.

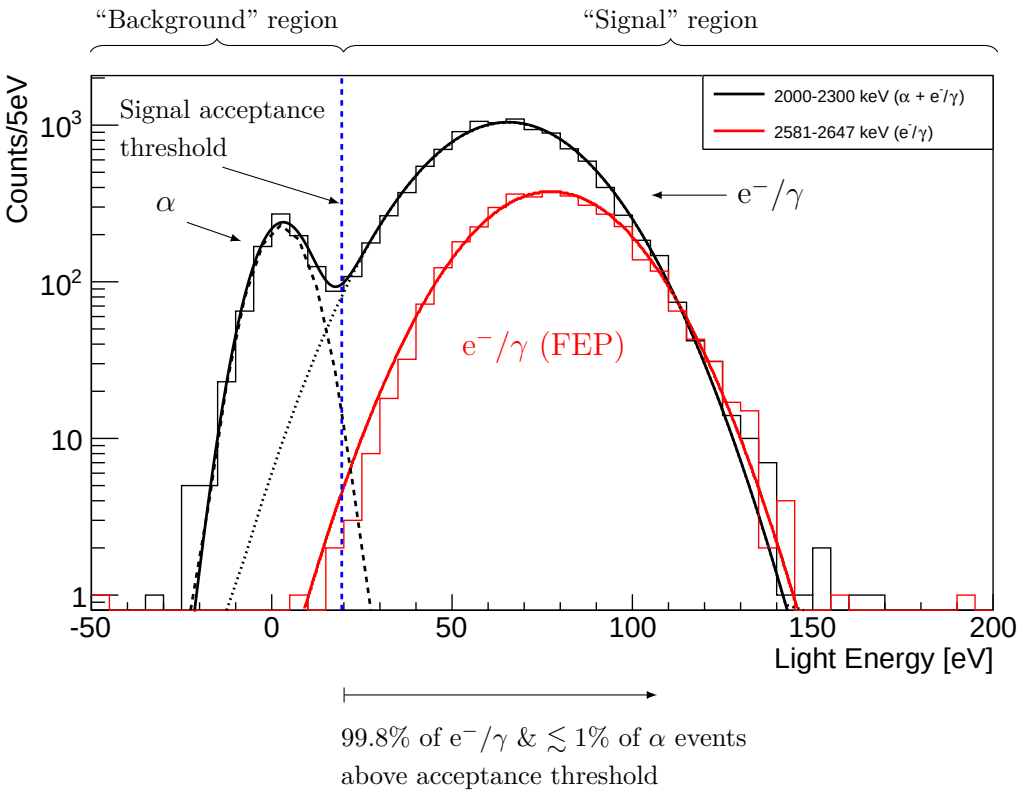

Figure 5.21: For this measurement with applied NL voltage (compare figure 5.19 for a 2d histogram of the data), a signal acceptance threshold of 19 eV (vertical dashed line) is obtained, corresponding to a signal acceptance of 99.8% in the e^-/γ reference region (red histogram and solid line). The percentage of α-induced events (black dashed line) above this threshold is $\lesssim 1\%$. See also [55].

background events [84, 62].

The suppression efficiency determined in the present work therefore allows to anticipate the contribution due to α-induced events to the background level in the ROI for next generation $0\nu\beta\beta$-decay experiments employing the phonon-light technique with NL amplified light detectors. Using the background level anticipated by the CUORE experiment, the background level in future experiments would correspond to $\sim 10^{-4}$ cts/keV/kg/yr (resulting in a background level close to zero for an exposure on the ton $\times$ year scale).

Therefore, the background suppression technique investigated experimentally in the present work can provide an important contribution to future generation $0\nu\beta\beta$-decay experiments. It should, however, be noted that the success of employing this background suppression technique depends on the assumption that the excellent energy resolution and background level in the ROI achieved by current experiments (see, e.g., [64]) can be maintained when operating additional light detectors required for the detection of the emitted Cherenkov radiation. Especially the potential introduction of additional background sources into the experiment (e.g., via radioactive contaminations in the wiring required to operate the additional detectors or in the light-reflecting foils used to increase the light collection efficiency) has to be investigated by experiments adapting this background suppression technique.

Due to practical reasons[41], the crystals employed in cryogenic experiments searching for the $0\nu\beta\beta$ decay have masses of $\sim 500 - 1000$ g. It is therefore important to show that the background suppression efficiency achieved in the present work can also be achieved with such larger crystals. In previous measurements which used TeO_2 crystals with a mass of 117 g [86] and 750 g [62] and germanium light detectors with NTD readout to measure the Cherenkov radiation, no highly efficient background suppression could be achieved. In a recent measurement [63], however, it could be shown that the background suppression demonstrated in the present work (see also [55]) can also be achieved with a larger (mass 285 g) TeO_2 crystal.

In order to fully evaluate the potential of this background suppression technique, further systematic studies regarding the influence of various experimental parameters (e.g., the size and geometry of the TeO_2 crystal, the light

[41] By using larger crystals, the number of required readout channels can significantly be reduced. This is especially important for experiments operating total detector mass of $\mathcal{O}(1\,\text{ton})$.

reflecting foil used to increase the light collection efficiency in the detector module, and the absorber material of the light detector) as well as the optical properties of the TeO_2 crystals (i.e., mainly regarding the absorption and scattering lengths in TeO_2) on the background suppression efficiency have to be performed.

Chapter 6

Summary and Outlook

The Neganov-Luke effect provides a method to significantly increase the sensitivity of cryogenic light detectors at low energies. The heat signal, induced by the absorption of photons in a semiconductor absorber operated at cryogenic temperatures, is amplified by drifting the produced charge carriers in an applied electric field. In addition to the signal amplification, this also leads to an improvement of the signal-to-noise ratio of the detector and, consequently, to an increased sensitivity. Previously, Neganov-Luke amplified light detectors have been studied in the framework of the direct dark matter search experiments CRESST-II and EURECA. In the work presented here, the application of Neganov-Luke amplified cryogenic light detectors for the background suppression in non-scintillating TeO_2 bolometers, which are being used in cryogenic experiments searching for the $0\nu\beta\beta$ decay, has been demonstrated for the first time.

The development of active background suppression techniques is particularly relevant for future generation $0\nu\beta\beta$-decay experiments which strive to reach a sensitivity of $\sim 10\,\mathrm{meV}$ for the effective neutrino Majorana mass (corresponding to a sensitivity on the $0\nu\beta\beta$-decay half life of $\sim 10^{27} - 10^{28}\,\mathrm{yr}$). The key to achieve this projected sensitivity is a significant reduction of the radioactive background in these experiments. A novel background suppression technique for cryogenic experiments employing non-scintillating target crystals (such as TeO_2 crystals) in the search for $0\nu\beta\beta$ decay is based on the simultaneous detection of the Cherenkov radiation emitted by high-energetic ($\mathcal{O}(2 - 3\,\mathrm{MeV})$) electrons within the crystal using a cryogenic light detector and the heat signal in the main target crystal. Using this technique, α-induced events (which produce no Cherenkov radiation) can efficiently be discriminated from e^-/γ-induced events (which produce a small amount of Cherenkov radiation).

To validate the potential of Neganov-Luke amplified light detectors for this background suppression technique, a new cryogenic detector module consisting of a $\sim 24\,\mathrm{g}$ TeO_2 crystal ($20 \times 20 \times 10\,\mathrm{mm}^3$) and Neganov-Luke amplified cryogenic light detector (a $20 \times 20 \times 0.5\,\mathrm{mm}^3$ silicon substrate equipped with four aluminum electrodes deposited onto the side of the substrate facing the crystal) has been successfully operated in the shallow underground laboratory at the Technische Universität München.

For the application of this background suppression technique in future $0\nu\beta\beta$-decay experiments it is important to show that a highly efficient suppression between α- and e^-/γ-induced events can be achieved at energies close to the $Q_{\beta\beta}$ value of ^{130}Te ($\sim 2.5\,\mathrm{MeV}$). Therefore, the TeO_2 crystal is irradiated with α particles from a ^{147}Sm α-source (which provides a continuous, energy degraded, spectrum of α particles with a maximal energy of $\sim 2.3\,\mathrm{MeV}$) and by γ rays from a ^{228}Th source (providing $2.614\,\mathrm{MeV}$ γs from the decay of ^{208}Tl). It could be shown by simulations that the amount of Cherenkov radiation produced by γ interactions in the full energy peak of the $2.614\,\mathrm{MeV}$ γ line is practically identical to the amount of Cherenkov radiation expected for $0\nu\beta\beta$-decay events of ^{130}Te.

Within the present work, the light detector is operated with a Neganov-Luke voltage of $V_{NL} = 70\,\mathrm{V}$ applied between the electrodes. The heat signal induced by the absorption of photons in the silicon substrate could be amplified by a factor of ~ 10.8 and an improvement in the signal-to-noise ratio of ~ 6.2 could be reached. By employing a novel LED-calibration technique, the energy-dependent resolution of the light detector was evaluated and a significant improvement of the energy resolution at low energies could be achieved. The 1σ energy resolution of the light detector, when operated with applied Neganov-Luke voltage, was found to be $\sim 7.8\,\mathrm{eV}$. In a $\sim 16\,\mathrm{h}$ measurement, performed without a Nevanov-Luke voltage applied to the detector, no suppression between α- and e^-/γ-induced events as obtained. However, during a $\sim 42\,\mathrm{h}$ measurement performed with a Neganov-Luke voltage of $V_{NL} = 70\,\mathrm{V}$ applied to the detector, a suppression of $\gtrsim 99\%$ of alpha induced events could be achieved while at the same time accepting 99.8% of the singal-like e^-/γ events. These results indicate that the background level in $0\nu\beta\beta$-decay experiments employing TeO_2 crystals could be improved by ~ 2 orders of magnitude.

The results of the measurements performed in this work show for the first time that a highly efficient event-by-event discrimination between α and e^-/γ induced events with practically no reduction in signal acceptance can be achieved using Neganov-Luke amplified cryogenic light detectors. Showing

that such a highly efficient background suppression can be realized in practice is an important milestone in the development of an active background suppression for the next generation of $0\nu\beta\beta$ experiments employing TeO_2 bolometers.

To apply this background suppression technique in future-generation $0\nu\beta\beta$-decay experiments, a better systematic understanding of the individual results concerning the background suppression efficiency obtained by different groups investigating this technique has to be reached (see discussion in section 5.7). This includes studying the influence of different crystal properties (i.e., crystal size, crystal shape, surface roughness, and absorption and scattering lengths), different light detector materials (i.e., silicon, germanium, and silicon-on-sapphire), and light reflecting materials like VM2002 or PTFE foils on the collection efficiency of the emitted Cherenkov radiation. The Monte-Carlo simulations performed in this work show that roughening the surface of the crystal as well as the absorption length in TeO_2 crystals have significant influence on the light collection efficiency. Furthermore, the simulations also indicate that, by employing a light reflecting foil with a high reflectivity in the UV spectrum, the amount of Cherenkov radiation which can in principle be detected could be doubled.

The next step in the development of Neganov-Luke amplified cryogenic light detectors will be an increase in the size of the light absorber (i.e., to sizes of $40 \times 40\,mm^2$ or larger) in order to make this technology compatible with the larger-sized crystals currently employed by direct Dark Matter and $0\nu\beta\beta$-decay experiments. It is furthermore important to study the origin of the reduced thermal gain and the relatively low voltages applicable to silicon-based Neganov-Luke light detectors since the sensitivity and signal-to-noise ratio could be significantly increased if the full potential of this technology could be utilized. First indications point towards a significant influence of the photolithographic lift-off process on the achievable detector performance which leads to a significant reduction of the applicable voltages. In appendix B an improved manufacturing technique for Neganov-Luke light detectors is described and first measurements with cryogenic detectors produced according to this technique are currently in preparation.

Appendices

Appendix A

Monte-Carlo Simulation of the Light-Collection Efficiency

This appendix describes first results of a Monte-Carlo simulation, performed to study the collection efficiency of Cherenkov radiation in a TeO_2 detector module. The simulation is based on a similar simulation for $CaWO_4$ crystals which has been carried out in [74]. The simulation has been adapted to incorporate the experimental conditions relevant for detecting Cherenkov radiation from TeO_2 crystals.

Setup

This Monte-Carlo simulation uses, as the simulation described in chapter 3, version *4.9.6.p03* of the GEANT4 simulation toolkit [102]. In this simulation, only the propagation of optical photons within the simulated setup is implemented. Their propagation is determined by the optical properties of the individual materials (e.g., the refractive index and absorption and scattering lengths) and the optical properties (e.g., the reflectivity and surface roughness) of the boundary surface between different media (e.g., TeO_2-vaccum or vaccum-VM2002).

The setup implemented in the simulation, as shown in figure A.1, resembles a simplified model of the detector module used for the low-temperature measurements[1]. The simulation includes a TeO_2 crystal and a silicon light absorber and the whole setup is completely enclosed by a reflective foil (3M© VM2002). The simulation includes the dimensions of the TeO_2 crystal ($20 \times 20 \times 10\,mm^3$)

[1]The present setup does not take any support structure required to mount the crystal and light detector within the housing into account, i.e., the PTFE and Sintimid clamps described in section 5.1 are not simulated.

and light detector ($20 \times 20 \times 0.5\,\mathrm{mm}^3$) used in the low-temperature measurements described in chapter 5 as well as the dimensions for a hypothetical detector module employing a $50 \times 50 \times 50\,\mathrm{mm}^3$ TeO_2 crystals. In the latter case, the size of the light detector is adapted accordingly ($50 \times 50 \times 0.5\,\mathrm{mm}^3$). The distance between the crystal and the light detector is 1 cm and the distance between the reflective housing and the crystal and the light detector is 0.5 cm. These values are constant throughout all simulations.

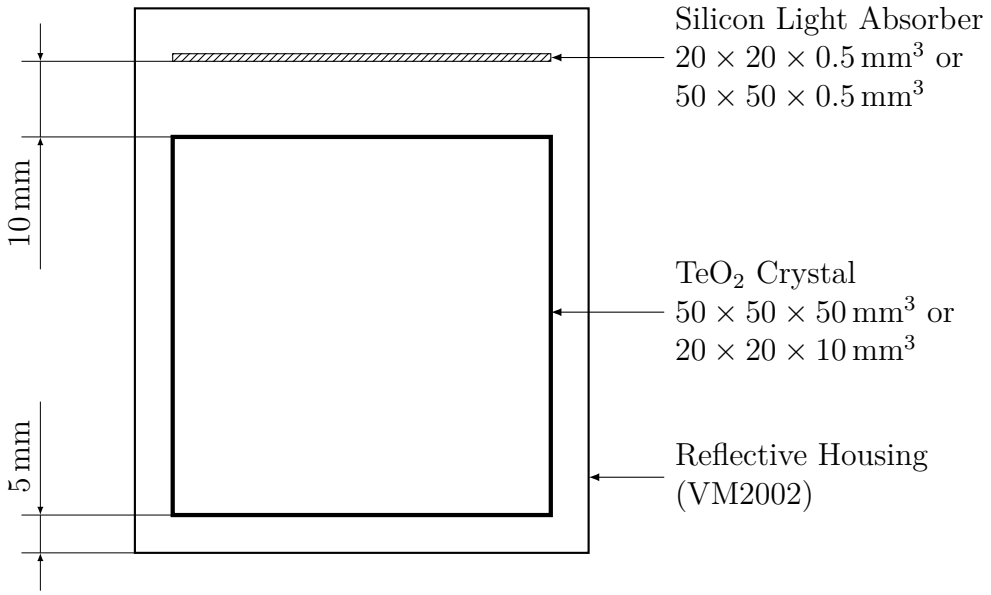

Figure A.1: Schematic drawing of the geometry of a detector module consisting of a TeO_2 crystal and a silicon light detector, as implemented in the Monte-Carlo simulation.

In the simulation, a simplified model of the optical properties of the TeO_2 crystal is implemented. Since no implementation of birefringent materials is possible using standard GEANT4 methods, an average refractive index (see figure 2.5) is implemented in the simulation. Unfortunately, the absorption and scattering length of the TeO_2 crystal used in the low-temperature measurements are unknown. The author is only aware of absorption length measurements for a similar TeO_2 crystal, published by the Rome group [85, 91], which show values that differ by a factor of ~ 2 ($\sim 38\,\mathrm{cm}$ and $\sim 80\,\mathrm{cm}$) in the spectral range above $\sim 320\,\mathrm{nm}$. Since no values for the scattering length in TeO_2 are available, this parameter is not implemented in the simulation[2].

[2]The scattering length is a parameter which also has influence on the light collection efficiency since, due to scattering, the angle between the photons' trajectory and the crystal surface can be changed. This affects the probability of the photon to escape the crystal.

To study the influence of different absorption length in the simulation, an wavelength-dependent absorption length is modeled according to the following equation:

$$L_{abs}(\lambda) = l_0 \cdot 1/2(1 + \mathrm{erf}((\lambda - \lambda_{cutoff})/\Delta\lambda) \tag{A.1}$$

which is an approximation of the values given in [85, 91]. The parameter l_0 describes the constant absorption length above the cut-off wavelength $\lambda_{cutoff} = 325\,\mathrm{nm}$ and the term $\Delta\lambda = 5\,\mathrm{nm}$ implements a finite transition width between the transparent and non-transparent region. Figure A.2 shows the spectral shape of the three implemented absorption lengths ($l_0 = 20, 60, 100\,\mathrm{cm}$).

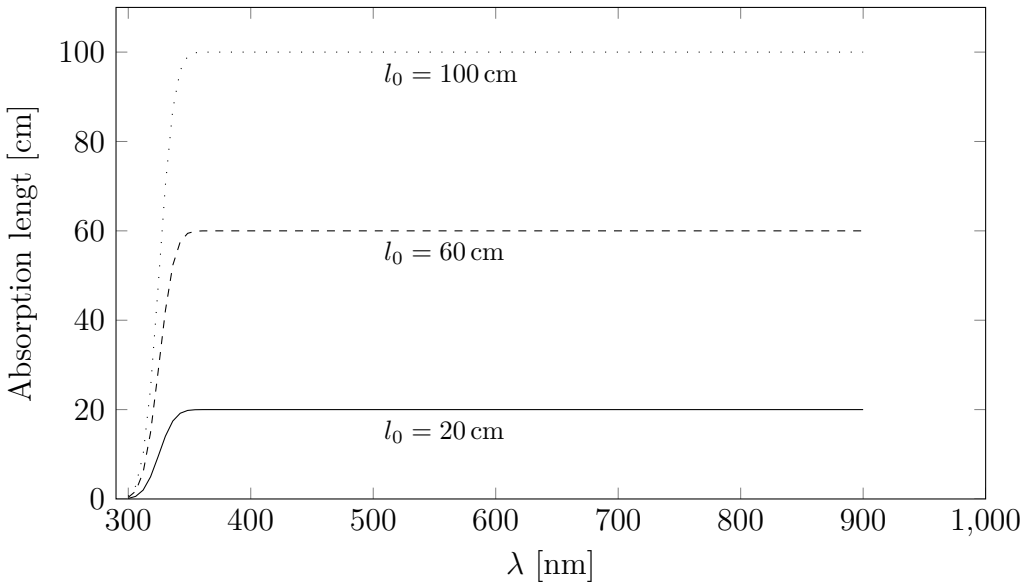

Figure A.2: Different absorption lengths as a function of wavelength. The absorption lengths implemented in the simulation are modeled according to equation (A.1) using $\lambda_{cutoff} = 325\,\mathrm{nm}$ and $\Delta\lambda = 5\,\mathrm{nm}$.

As has been shown in [74], the absorption length has significant impact on the observed collection efficiency, i.e., favoring longer absorption length. This is due to the fact that a significant amount of the produced light is trapped inside the crystal due to total internal reflection at the crystal surfaces. In TeO_2, the critical angle for total internal reflection is only $\theta_g \approx 24°$ (assuming a refractive index of $n = 2.4$).

In the future, systematic measurements of the optical properties of TeO_2 crystals, especially with respect to the absorption and scattering lengths, have

to be carried out in oder to perform extensive studies of the optimization potential of the collection efficiency.

The surface of the crystal is implemented to be either polished or roughened. The surface properties are implemented using the method described in [74]. The roughened surface is modeled using randomly oriented micro-facets and is described by a single parameter σ_α which characterizes the normal distributed angle α between the micro-facet normal and the average surface normal. Here, the value of $\sigma_{alpha} = 45°$, as used as used in [74], is implemented. For future simulations, a measurement of the roughness of surface crystals is planned and will be compared to the values obtained for $CaWO_4$ crystals in [74].

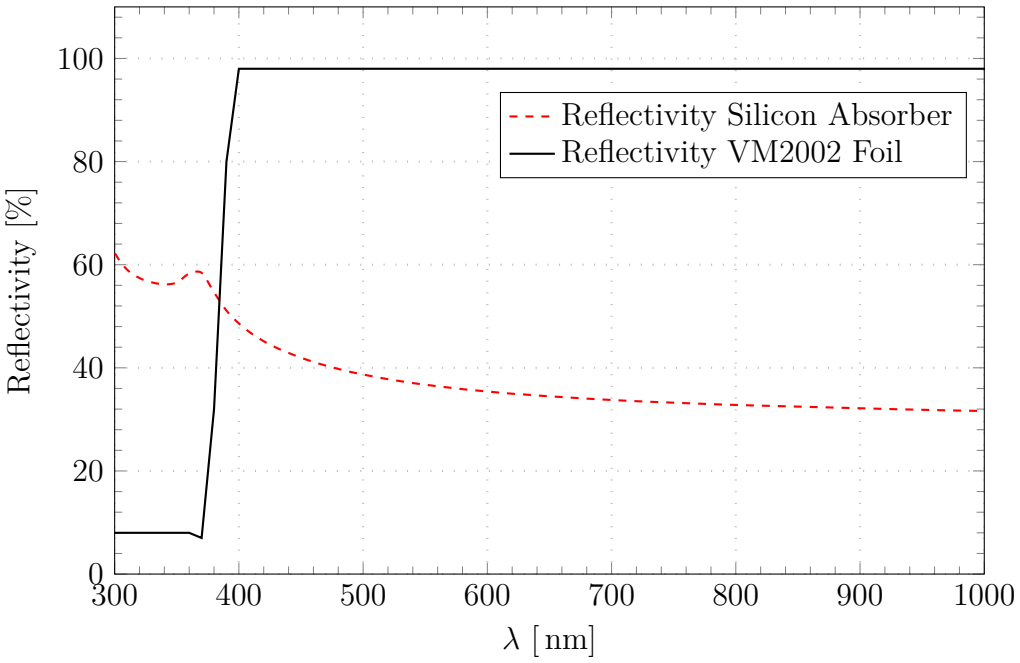

Figure A.3: Wavelength dependent reflectivity of the silicon light detector (calculated using values given in [98]) and the reflective foil (3M© *VM2002*) (using data from [96]) used to cover the detector housing.

At the surface of the silicon light detector and the reflective housing, the optical photons are either reflected or absorbed, according to the respective efficiencies implemented in the simulation. The reflectivity of the VM2002[3] foil is taken from a room temperature measurement [96] and is implemented according to [74]. The reflectivity of the silicon light detector is calculated

[3] As discussed in [74], the scintillation properties are not implemented in the simulation.

using room temperature values from [98]. Figure A.3 shows the reflectances implemented in the GEANT4 simulation. The absorption efficiency for both the light detector and the VM2002 foil is unity in the whole spectral range, i.e., all optical photons which are not reflected are absorbed at the surface of the respective volumes.

As in [74], for each simulation run 5000 events are generated at random positions inside the crystal. The angular and polarization distribution of the photons is modeled according to the method implemented in [74], i.e., for each event 10000 photons with random linear polarization are emitted over a solid angle of 4π, which describes the generation of scintillation light very well. However, the produced Cherenkov radiation is emitted on a cone with an opening angle of Θ_C relative to the charged particles direction. This could lead to a larger statistical uncertainty in the light collection efficiency, depending on the direction in which the particle moves (e.g., towards the light detector or away). The energy of the photons is sampled according to the spectral shape obtained from the simulation described in chapter 3 (see figure 3.2). For future simulations, the implementation of the event generators described in chapter 3 is planned which allows to study possible differences in the collection efficiency for different kinds of interactions (e.g., γ or e^- induced events). Nonetheless, the method implemented here is expected to yield the correct average collection efficiency.

Challenges for the Experimental Validation of the Simulation

In contrast to scintillating crystals, the experimental validation of the simulation code for non-scintillating crystals is more challenging. In [74], measurements with a photomultiplier tube (PMT) were performed to validate the simulated collection efficiencies. Events due to Cherenkov radiation produced by γ interactions, e.g., in the glass of the PMT can in principle be distinguished from scintillation events based on their time evolution (i.e., Cherenkov events lead to prompt signals (decay time $\tau \ll 1\,\mathrm{us}$) while scintillation events are characterized by the decay time of the scintillation ($\tau = \mathcal{O}(10\,\mathrm{us})$). This however is not possible in this case since only Cherenkov events are expected.

Results

In a first step, the light collection efficiency in the detector module shown in figure A.1 is studied for a TeO_2 crystal of $20 \times 20 \times 10\,mm^3$ in dependence of the absorption length in the crystal. The simulations were performed for both a crystal where all sides are roughened as well as for a crystal where all sides are perfectly polished. The two panels of figure A.4 show the fraction of the produced number of photons which is absorbed in the individual components of the detector module for both cases.

From these plots it can clearly be seen that roughening the surfaces increases the amount of light which can escape the TeO_2 crystal by a factor of $2 - 3$, depending on the absorption length. A significant amount of light is absorbed in the reflective foil due to the cut-off in reflectivity at $\sim 390\,nm$ (compare to figure A.3 and section 2.4.3). It can be seen that for a crystal with polished surfaces, a large fraction of the light is trapped inside the crystal due to total internal reflection.

This simulation was also performed for a detector module which is not completely covered by the reflective foil and additionally contains openings in the detector housing which are comparable to the actual detector module (compare figure 5.1) used for the low-temperature measurements in the present work[4]. In this simulation, all crystal surfaces are roughened. The results of the simulation is shown in figure A.5. It can be seen that a significant amount of light escapes the detector module[5] through these openings, resulting in a light collection efficiency which is reduced by a factor of $\sim 1/3$. The collection efficiency determined for this detector module[6] is compatible with the light collection efficiency determined in chapter 5. Therefore, by further increasing the coverage with reflective foil in the actual housing used for the measurements, the light collection efficiency achieved in the low-temperature measurements performed in the present work could be significantly improved.

[4]These openings are required to facilitate the electrical feed troughs and bond pads.

[5]It should be noted that the fraction of light escaping the module also includes light in the spectral range below $\sim 390\,nm$ otherwise which would be absorbed in the reflective foil.

[6]The actual coverage with reflective foil, due to the support structure required to mount the detectors within the module, is likely smaller than in the simplified geometry implemented in the simulation which only features openings in the reflective housing. Therefore, the values obtained here can be as considered upper limits of the actual light collection efficiency.

In order to determine the effects of the absorption length and surface roughening, the simulation is also performed using a larger crystal with dimensions of $50 \times 50 \times 50\,\mathrm{mm}^3$. The reflective housing is scaled up from the reflective housing used to simulate the $20 \times 20 \times 10\,\mathrm{mm}^3$ crystal. The results of this simulation are shown in figure A.6. It can be seen that roughening the crystal surface increases the amount of light which can escape from the crystal by a factor of $\gtrsim 2$ (a result similar to the increase observed for $CaWO_4$ crystals [74]) and that a signifiant amount of light is absorbed in the reflective foil.

It can be concluded that, in order to maximize the light collection efficiency in such a cryogenic detector module, roughening the crystal surfaces is essential and that the light collection efficiency could be significantly increased by using a reflective foil with a higher reflectivity in the UV spectrum.

Future Developments and Improvements

The results of these simulations show that the light collection efficiency can be significantly increased by roughening the surface of the TeO_2 crystal. The simulation furthermore shows the importance of the absorption length of the TeO_2 crystal, a parameter currently not yet systematically investigated for crystals used in $0\nu\beta\beta$ experiments. Future experiments planning to integrate the phonon-light technique in an experiment using TeO_2 crystals will be required to systematically study the optical properties of the employed crystals.

For the future, the following improvements of the simulation are planned:

- Implementation of more accurate optical parameters of TeO_2 crystals (i.e., the refractive index measured at cryogenic temperatures, systematic measurements of the absorption and scattering lengths) once they are available.
- Implementation of the event generators described in section 3.1.4 into this simulation to study effects of Cherenkov radiation produced by electrons of different origin (e.g., $0\nu\beta\beta$ induced or γ induced).
- Implementation of additional reflector materials, especially reflectors with a high reflectivity in the UV range (e.g., PTFE foil).
- Implementation of additional light detectors (e.g., Germanium, SOS see [74]) to study the differences in the light collection efficiency for these absorbers.

- Determination of the actual TeO_2 crystals surface roughness using a surface profiler as described in [74].

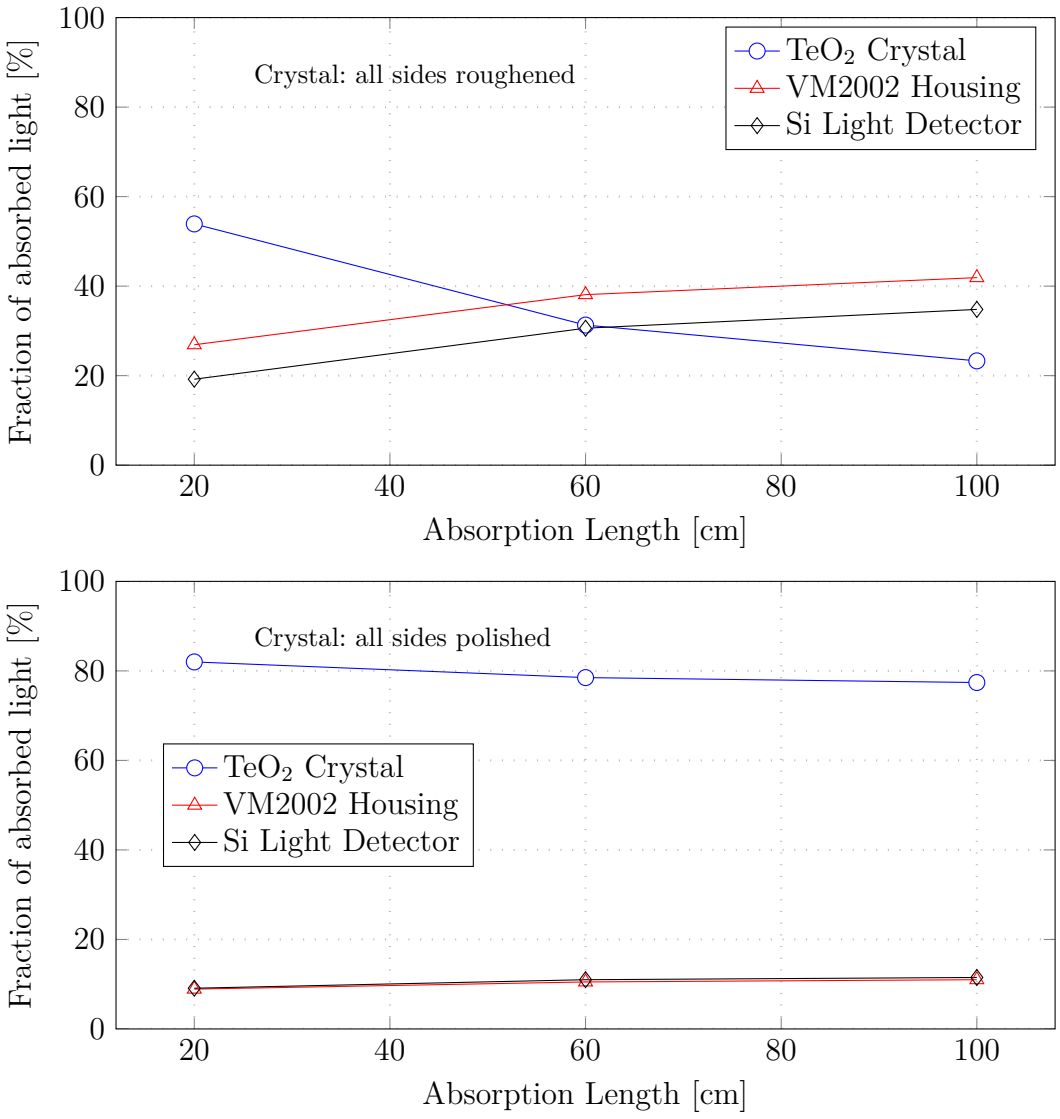

Figure A.4: Results of the simulation concerning the light propagation in a detector module (consisting of a $20 \times 20 \times 10\,\mathrm{mm}^3$ TeO_2 crystal and a $20 \times 20 \times 0.5\,\mathrm{mm}^3$ silicon light detector placed inside a reflective housing (compare figure A.1)) showing the fraction of the initially produced light which is absorbed in the individual components of the detector module. All sides of the crystal are either roughened (top) or polished (bottom). It can be seen that roughening the crystal surfaces increases the amount of light which can escape the crystal by a factor of $\sim 2 - 3$.

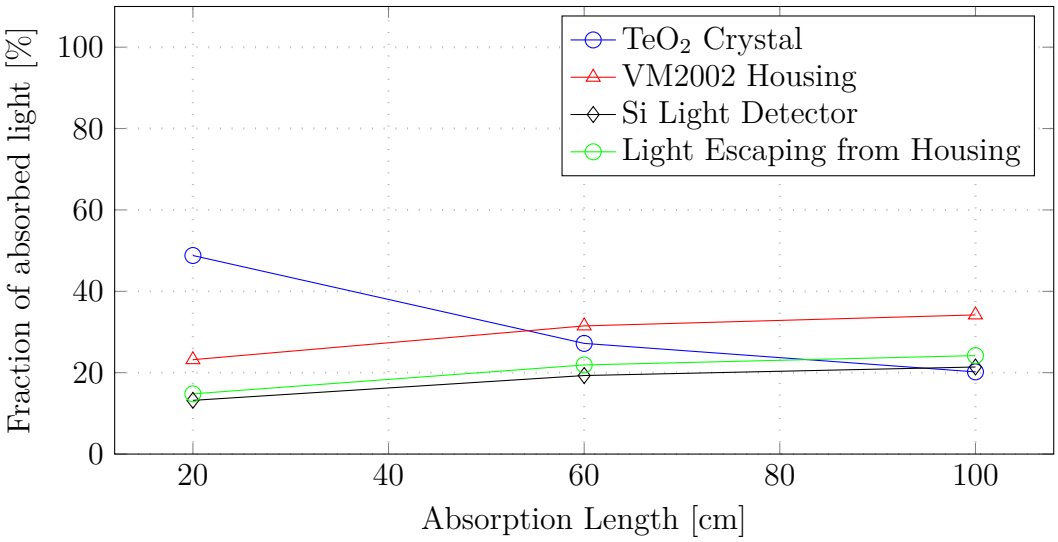

Figure A.5: Results of the simulation concerning the light propagation in a detector module (consisting of a $20 \times 20 \times 10\,\mathrm{mm}^3$ TeO_2 crystal and a $20 \times 20 \times 0.5\,\mathrm{mm}^3$ silicon light detector placed inside a reflective housing which features openings similar to the openings present in the detector module used for the low-temperature measurements in this work (compare figure A.1 and section 5.1)) showing the fraction of the initially produced light which is absorbed in the individual components of the detector module. All sides of the crystal are roughened. It can be seen that a significant amount of light escapes the detector module undetected. By optimizing the coverage of the reflective foil in the detector module used for the low-temperature measurements, a significant improvement of the total amount of collected Cherenkov light could be achieved.

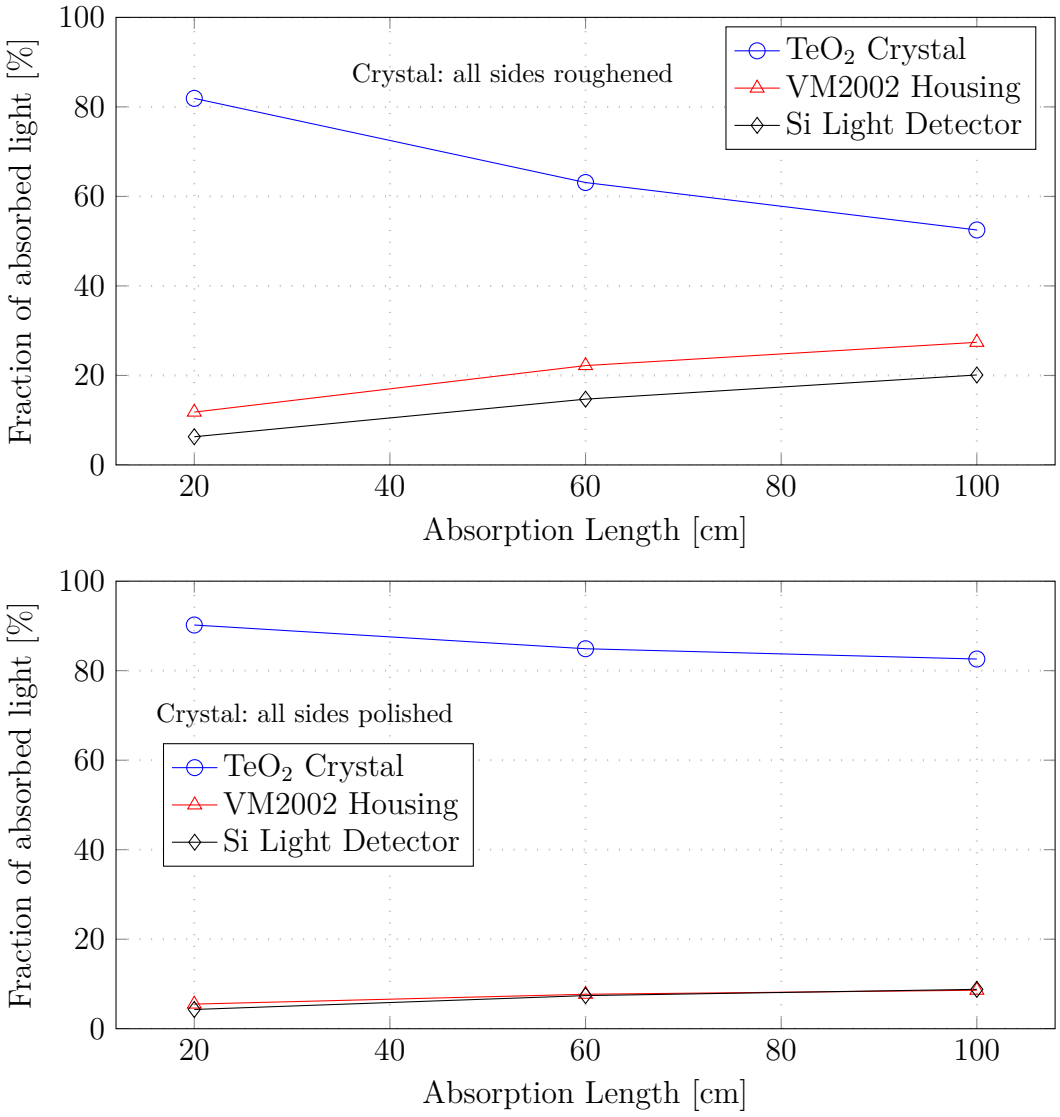

Figure A.6: Results of the simulation concerning the light propagation in a detector module (consisting of a $50 \times 50 \times 50\,\mathrm{mm}^3$ TeO_2 crystal and a $50 \times 50 \times 0.5\,\mathrm{mm}^3$ silicon light detector placed inside a reflective housing (compare figure A.1)) showing the fraction of the initially produced light which is absorbed in the individual components of the detector module. All sides of the crystal are either roughened (top panel) or polished (bottom panel). It can be seen that roughening the surface significantly increases the amount of light which can escape the crystal by a factor of $\gtrsim 2$. However, a large fraction of the light is absorbed in the reflective foil ($\lambda_{cut-off} \approx 390\,\mathrm{nm}$). The light collection efficiency could be significantly increased by using a reflective foil with a higher reflectivity below 390 nm.

Appendix B

New Production Process for Aluminum Contacts

Motivation

As discussed in this work and in [59] and [61], the potential of NL light detectors is currently limited by the observed reduction of the thermal gain with time and the fact that the theoretical expected thermal gain can not be not achieved currently. Furthermore, only relatively small voltages of $\mathcal{O}(100 - 150\,\mathrm{V})$ can presently be applied to NL light detectors. The first point has been studied in [61] and the new production process described therein leads to significantly lower reduction of the gain with time. The last two points are likely correlated since both are affected by the surface of the substrate (i.e. the reduced gain compared to the expected value is likely caused by trapping of charge carriers in impurities and defects at the absorber surface. These defects at the absorber surface are also likely to aid the formation of currents flowing across the substrate surface once the break-through voltage is exceeded). If higher voltages could be applied across the substrate, it is very likely that the observed thermal gain and therefore also the achievable improvement in the signal-to-noise ratio will increase.

Recent measurements [128] indicate that the photolithographic lift-off process used during the deposition of the aluminum electrodes on the silicon absorber (similar to the process described in section 4.1.2) has a negative impact on the voltage which can be applied between the electrodes. Once the photolithographic process has been performed, the voltage which can be applied across the surface of the substrate is significantly reduced from $\mathcal{O}(600\,\mathrm{V})$ prior the application of the photoresist to $\lesssim 100\,\mathrm{V}$ after photolithographic process

is completed. This is likely due to residue of the photoresist remaining on the substrate surface and defects induced during the handling of the substrate.

To overcome the limitations caused by the relatively low applicable voltage, a new production method based on the deposition of the aluminum electrodes via a shadow mask is proposed. In the following, this new method will be discussed in detail.

Modified Production Technique

For the deposition of well defined aluminum contacts on the silicon absorber substrates of NL light detectors, there are mainly two commonly used production methods:

- Thin-film deposition using a photolithographic lift-off process (compare section 4.1.2).
- Thin-film deposition using a metallic shadow mask (compare e.g. [59])

The second production process has also some several disadvantages since a direct contact between the metallic shadow mask (typically made from a sheet of tantalum) and the semiconductor absorber can also lead to damages on the crystal surfaces and metallic residue, two effects which have been found to reduce the performance of such light detectors.

Therefore, a modified production method is proposed which allows the fabrication of the aluminum electrodes using metallic shadow masks. In the new method, the aluminum film is deposited onto a substrate which is mounted inside a special detector holder, depicted in figure B.1. The substrate is placed into a PTFE holder and is directly covered with a thin ($\mathcal{O}(50 - 100\,\mu\mathrm{m})$) PTFE or Kapton foil. The metallic shadow mask is placed above this foil. The PTFE or Kapton foil is cut out on the same positions as the shadow mask. Springs inside the substrate holder are used to ensure a firm contact between the substrate and the shadow mask.

This fabrication technique has several advantages compared to the photolithographic lift-off process:
a) The number of production steps is significantly reduced, i.e. the application and removal of the photoresist as well as the baking and exposure to UV light are not required anymore. This furthermore reduces the risk of accidentally damaging the silicon substrate.

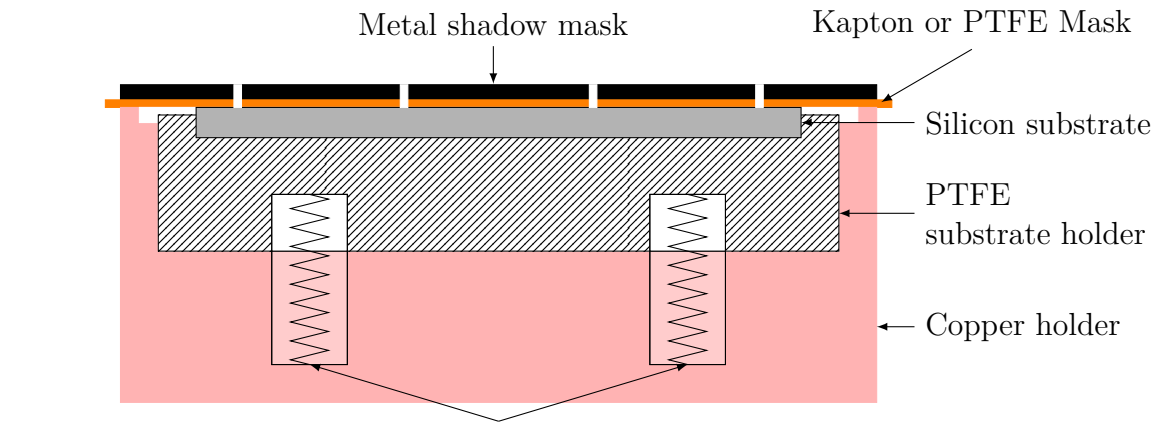

Figure B.1: Schematic representation of the substrate holder conceived for the new production process of aluminum electrodes.

b) The risk of damaging the silicon substrate during the deposition process is also reduced since the substrate is only in contact with "soft" materials, i.e. Kapton or PTFE.

First measurements already show [128] that by using this production method in combination with the annealing step described in [61] much larger voltages can be applied between the electrodes. First measurements with cryogenic light detectors produced with to this modified method are in preparation [127].

Due to the low melting point of PTFE of 600K, this fabrication method cannot be used in cases where the substrate is heated during the deposition process (i.e. to increase the adhesion of the metallic film to the substrate) where typically temperatures of up to 500 °C are required.

Furthermore, the structures of the shadow mask are currently limited to a minimal width of $\sim 500\,\mu$m and are limited in their complexity since they have to be either milled or cut using a circular saw. However, by employing laser-cutting techniques, micro machining of structures as small as $\lesssim 100\,\mu$m in thin metal sheets (e.g. stainless steel) can be achieved.

For the fabrication of smaller sized structures, a slightly different fabrication method is proposed which employs shadow masks made from thin silicon or sapphire substrates [133]. Fine structures in silicon substrates can be produced by means of chemical etching, a technique widely used in the micro

fabrication of semiconductor devices. In this way, shadow masks with very fine structures could be produced. This technique also allows the deposition of the metallic thin films at much higher temperatures and additionally, the materials used for the fabrication of the shadow mask can be selected to have a high radio-purity. This aspect could also be important for rare event search experiments.

First Results

In [128], first measurements of the current-voltage characteristic of silicon substrates with NL electrodes have been performed in order to determine influence of different production steps on the voltages applicable across a substrate. The voltage is applied between the electrodes using a high-voltage source (model *HCB 0,14-1250*, *FuG Elektronik GmbH*, Germany) and the corresponding current is measured using the current meter built into the voltage source. The voltage is applied to the substrate with both positive and negative polarity. Figure B.2 shows the current-voltage characteristic of a silicon substrate with NL electrodes which are manufactured according to the process described in section 4.1.2 during various steps of the production process (i.e., for an untreated substrate as delivered by the manufacturer, for a substrate cleaned in an ultrasonic bath, and after the deposition of the aluminum electrodes). All curves have been measured at at temperature of 4 K using a LHe-dipstick [128]. The steep rises in the current-voltage characteristics indicates the "break-through" of the substrate which is characterized by a current of several μA flowing suddenly across the substrate[1]. It can be seen that the break-through occurs at much lower voltages after the aluminum electrodes have been deposited onto the substrate using the photolithographic process[2]. Figure B.3 shows the current-voltage characteristics for a substrate where the electrodes have been manufactured according to the new process described here (i.e., via a shadow mask). It can be seen that break-throughs occur only at relatively high voltages of ~ 500 V when this new process is employed. The observed behavior was reproducible for multiple substrates

[1] Due to the high specific resistivity of the silicon substrates used for these measurements ($\rho \approx 20\,\mathrm{k\Omega cm}$ at room temperature) [128], it is very likely that the current is flowing across the surface of the silicon substrate and not through the bulk.

[2] For the current-voltage characteristics for the untreated substrate and after the cleaning step, the substrate was contacted directly via ultrasonic wedge-bonding. After the deposition of the aluminum electrodes, the electrodes were contacted via ultrasonic wedge-bonding.

[128].

These results indicate that the fabrication of the aluminum electrodes via a photolithographic lift-off process significantly reduces the voltages applicable to the substrate and therefore also the achievable thermal gain, which is likely caused by the generation of defects at the surface of the substrate during the photolithographic process. The potential of this new fabrication process with respect to the performance of realized NL light detectors will be evaluated in measurements which are currently in preparation [127].

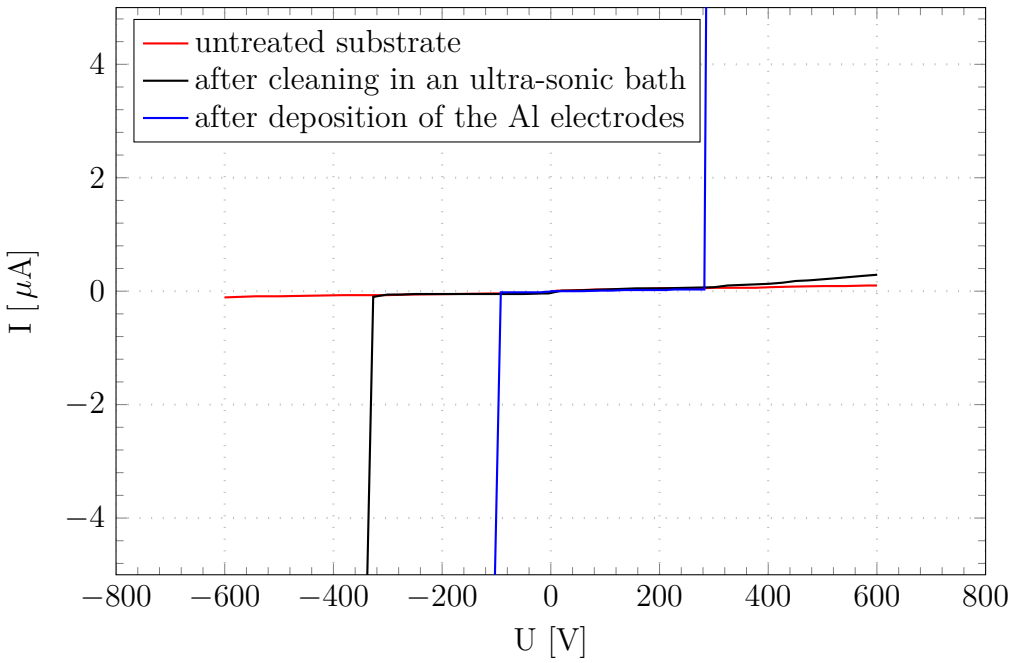

Figure B.2: Current-voltage characteristics for a silicon substrate with NL electrodes fabricated according to the photolithographic lift-off process described in section 4.1.2. It can be seen that a current is flowing across the substrate at relatively low voltages of $\sim 200\,\mathrm{V}$ once the aluminum electrodes have been deposited onto the substrate. Data taken from [128].

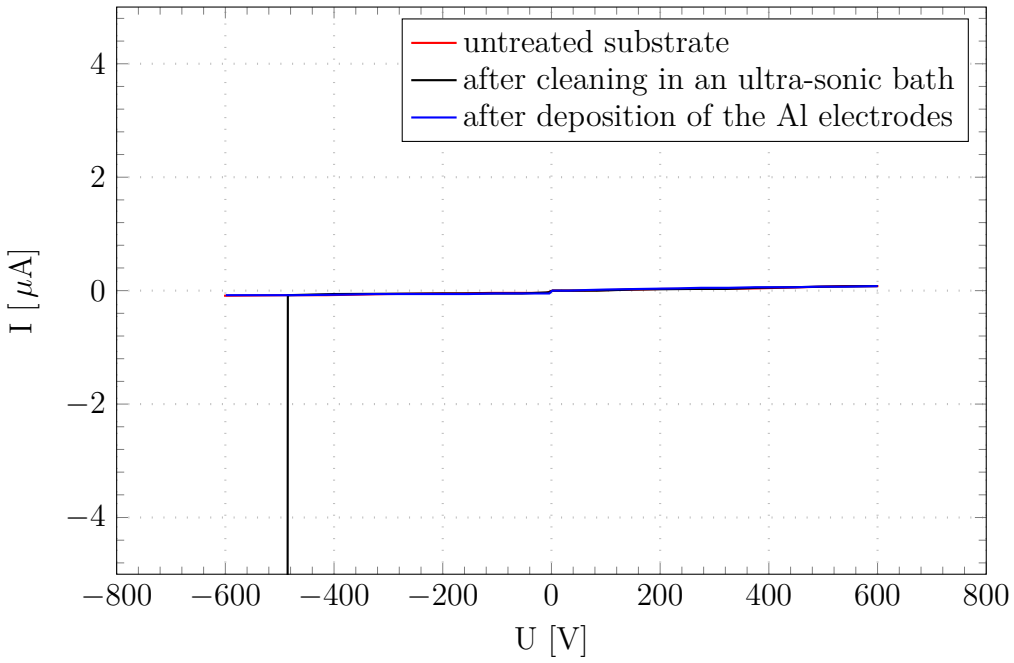

Figure B.3: Current-voltage characteristics for a silicon substrate with NL electrodes fabricated according to the new production process involving the deposition of the electrodes by means of a metallic shadow mask. It can be seen that a voltages of up to $\sim 500\,\mathrm{V}$ can be applied between the electrodes. This is a significant improvement compared to the results obtained for substrates manufactured using a photolithographic lift-off mask. Data taken from [128].

Bibliography

[1] J. Beringer, et al., *Review of Particle Physics*, Physical Review D **86**, 010001 (2012)

[2] B. T. Cleveland, et al., *Measurement of the solar electron neutrino flux with the Homestake chlorine detector*, Astrophysical Journal **496**, 505 (1998)

[3] Y. Fukuda, et al., *Measurements of the Solar Neutrino Flux from Super-Kamiokande's First 300 Days*, Physical Review Letters **81**, 1158 (1998)

[4] W. Hampel, et al., *GALLEX solar neutrino observations: results for GALLEX IV*, Physics Letters B **447**, 127 (1999)

[5] J. N. Abdurashitov, et al., *Measurement of the solar neutrino capture rate with gallium metal*, Physical Review C **60**, 055801 (1999)

[6] M. Altmann, et al., *GNO solar neutrino observations: results for GNO I*, Physics Letters B **490**, 16 (2000)

[7] Q. R. Ahmad, et al., *Direct Evidence for Neutrino Flavor Transformation from Neutral-Current Interactions in the Sudbury Neutrino Observatory*, Physical Review Letters **89**, 011301 (2002)

[8] S. N. Ahmed, et al., *Measurement of the Total Active ^8B Solar Neutrino Flux at the Sudbury Neutrino Observatory with Enhanced Neutral Current Sensitivity*, Physical Review Letters **92**, 181301 (2004)

[9] K. Eguchi, et al., *First Results from KamLAND: Evidence for Reactor Antineutrino Disappearance*, Physical Review Letters **90**, 021802 (2003)

[10] Y. Fukuda, et al., *Evidence for Oscillation of Atmospheric Neutrinos*, Physical Review Letters **81**, 1562 (1998)

[11] K. Abe, et al., *Observation of Electron Neutrino Appearance in a Muon Neutrino Beam*, Physical Review Letters **112**, 061802 (2014)

[12] F. P. An, et al., *Observation of Electron-Antineutrino Disappearance at Daya Bay*, Physical Review Letters **108**, 171803 (2012)

[13] Y. Abe, et al., *Improved measurements of the neutrino mixing angle θ_{13} with the Double Chooz detector*, JHEP **1410**, 86 (2014)

[14] J. Kopp, et al., *Sterile neutrino oscillations: the global picture*, Journal of High Energy Physics **2013**, 50 (2013)

[15] S. M. Bilenky, et al., *Neutrinoless Double-Beta Decay: a Probe of Physics Beyond the Standard Model* (2014), `arXiv:1411.4791v1`

[16] Borexino Collaboration, *First Evidence of pep Solar Neutrinos by Direct Detection in Borexino*, Physical Review Letters **108**, 051302 (2012)

[17] F. Capozzi, et al., *Status of three-neutrino oscillation parameters, circa 2013*, Physical Review D **89**, 093018 (2014)

[18] S. K. Agarwalla, et al., *The mass-hierarchy and CP-violation discovery reach of the LBNO long-baseline neutrino experiment*, Journal of High Energy Physics **2014**, 94 (2014)

[19] W. Winter, *Neutrino mass hierarchy determination with IceCube-PINGU*, Physical Review D **88**, 013013 (2013)

[20] K. Abe, et al., *Letter of Intent: The Hyper-Kamiokande Experiment — Detector Design and Physics Potential* (2011), `arXiv:1109.3262`

[21] L. Zhan, et al., *Experimental requirements to determine the neutrino mass hierarchy using reactor neutrinos*, Physical Review D **79**, 073007 (2009)

[22] E. W. Otten, et al., *Neutrino mass limit from tritium β decay*, Reports on Progress in Physics **71**, 086201 (2008)

[23] C. Kraus, et al., *Final results from phase II of the Mainz neutrino mass search in tritium β decay*, Eur. Phys. J. C **40**, 447 (2005)

[24] V. N. Aseev, et al., *Upper limit on the electron antineutrino mass from the Troitsk experiment*, Physical Review D **84**, 112003 (2011)

[25] V. Lobashev, *The search for the neutrino mass by direct method in the tritium beta-decay and perspectives of study it in the project KATRIN*, Nuclear Physics A **719**, 153c (2003)

[26] F. M. Fränkle, *KATRIN: an experiment to determine the neutrino mass* (2011), `arXiv:1110.0087v1`

[27] A. Nucciotti, *Neutrino mass calorimetric searches in the MARE experiment*, Nuclear Physics B (Proceedings Supplement) **229-232**, 155 (2010)

[28] L. Gastaldo, et al., *The Electron Capture ^{163}Ho Experiment ECHo*, Journal of Low Temperatur Physics **176**, 876 (2014)

[29] Planck Collaboration, *Planck 2013 results. I. Overview of products and scientific results*, Astronomy & Astrophysics **571**, A1 (2013)

[30] Planck Collaboration, *Planck 2013 results. XVI. Cosmological parameters*, Astronomy & Astrophysics **571**, A16 (2013)

[31] K. N. Abazajian, et al., *Cosmological and astrophysical neutrino mass measurements*, Astroparticle Physics **35**, 177 (2011)

[32] G. Pagliaroli, et al., *Neutrino mass bound in the standard scenario for supernova electronic antineutrino emission*, Astroparticle Physics **33**, 287 (2010)

[33] G. Fogli, et al., *Global analysis of neutrino masses, mixings and phases: entering the era of leptonic CP violation searches*, Physical Review D **86**, 013012 (2012)

[34] M. Goeppert-Mayer, *Double Beta-Disintegration*, Physical Review **48** (1935)

[35] A. S. Barabash, *Double Beta Decay: Historical Review of 75 Years of Research*, Phys. Atom. Nucl. **74**, 603 (2011)

[36] J. Gomez-Cadenas, et al., *Sense and sensitivity of double beta decay experiments*, JCAP **1106**, 007 (2011)

[37] W. Rodejohann, *Neutrinoless double-beta decay and neutrino physics*, Journal of Physics G **39**, 124008 (2012)

[38] J. Schechter, et al., *Neutrinoless double-β decay in SU(2)$\times$U(1) theories*, Physical Review D **25**, 2951 (1982)

[39] J. Kotila, et al., *Phase-space factors for double-β decay*, Physical Review C **85**, 034316 (2012)

[40] S. R. Elliott, et al., *Double beta decay*, Ann. Rev. Nucl. Part. Sci. **52**, 115 (2002)

[41] F. T. Avignonne, et al., *Double beta decay, Majorana neutrinos, and neutrino mass*, REVIEWS OF MODERN PHYSICS **80** (2008)

[42] M. Agostini, et al., *Results on Neutrinoless Double- Decay of ^{76}Ge from Phase I of the GERDA Experiment*, Physical Review Letters **111**, 122503 (2013)

[43] N. Abgrall, et al., *The MAJORANA DEMONSTRATOR Neutrinoless Double-Beta Decay Experiment*, Advances in High Energy Physics **2014**, 365432 (2014)

[44] C. Arnaboldi, et al., *CUORE: a cryogenic underground observatory for rare events*, Nuclear Instruments and Methods in Physics Research A **518**, 775 (2004)

[45] L. Canonica, et al., *First CUORE-0 Performance Results and Status of CUORE Experiment*, Journal of Low Temperatur Physics **175**, 986 (2013)

[46] J. Beeman, et al., *Current Status and Future Perspectives of the LUCIFER Experiment*, Advances in High Energy Physics **2013** (2013)

[47] M. Mancuso, et al., *An Aboveground Pulse-Tube-Based Bolometric Test Facility for the Validation of the LUMINEU $ZnMoO_4$ Crystals*, Journal of Low Temperatur Physics **176**, 571 (2014)

[48] L. Bergé, et al., *Purification of molybdenum, growth and characterization of medium volume ZnMoO4 crystals for the LUMINEU program*, Journal of Instrumentation P06004 (9)

[49] A. Gando, et al., *Limit on Neutrinoless $\beta\beta$ Decay of ^{136}Xe from the First Phase of KamLAND-Zen and Comparison with the Positive Claim in ^{76}Ge*, Physical Review Letters **110**, 062502 (2013)

[50] The EXO-200 Collaboration, *Search for Majorana neutrinos with the first two years of EXO-200 data*, Nature **510**, 229 (2014)

[51] B. Schwingenheuer, *Status and prospects of searches for neutrinoless double beta decay*, Annalen der Physik **525**, 269 (2013)

[52] G. Angloher, et al., *Results from 730 kg days of the CRESST-II Dark Matter search*, The European Physical Journal C **72**, 1971 (2012)

[53] M. A. Fehr, et al., *Application of MC-ICPMS to the precise determination of tellurium isotope compositions in chondrites, iron meteorites and sulfides*, International Journal of Mass Spectrometry **232**, 83 (2004)

[54] T. Tabarelli de Fatis, *Cerenkov emission as a positive tag of double beta decays in bolometric experiments*, The European Physical Journal C **65**, 359 (2010)

[55] M. Willers, et al., *Background discrimination in neutrinoless double beta decay search with TeO_2 bolometers using Neganov-Luke amplified cryogenic light detectors* (2014), `arXiv:1407.6516`

[56] B. Neganov, et al., Otkrytia i izobreteniya **146**, 215 (1985)

[57] P. N. Luke, *Voltageassisted calorimetric ionization detector*, Journal of Applied Physics **64**, 6858 (1988)

[58] G. Angloher, et al., *EURECA Conceptual Design Report*, Physics of the Dark Universe **3**, 41 (2014)

[59] C. Isaila, *Development of Cryogenic Light Detectors with Neganov-Luke Amplification for the Dark Matter Experiments CRESST and EURECA*, Ph.D. thesis, Technische Universität München (2009)

[60] C. Isaila, et al., *Low-temperature light detectors: Neganov–Luke amplification and calibration*, Physics Letters B **716**, 160 (2012)

[61] S. Roth, *The Potential of Neganov-Luke Amplified Cryogenic Light Detectors and the Scintillation-Light Quenching Mechanism in CaWO4 Single Crystals in the Context of the Dark Matter Search Experiment CRESST-II*, Ph.D. thesis, Technische Universität München (2013)

[62] M. Vignati, et al., *TeO_2 bolometers with Cherenkov signal tagging: towards next-generation neutrinoless double beta decay experiments* (2014), `arXiv:1403.5528v1`

[63] K. Schäffner, et al., *Particle Discrimination in TeO2 Bolometers using Light Detectors read out by Transition Edge Sensors* (2014), `arXiv:1411.2562`

[64] D. R. Artusa, et al., *Initial performance of the CUORE-0 experiment*, Eur. Phys. J. C **74**, 2956 (2014)

[65] R. Gross, et al., *Festkörperphysik*, Oldenbourg Verlag München (2012)

[66] F. Pröbst, et al., *Model for Cryogenic Particle Detectors with Superconducting Phase Transition Thermometers*, Journal of Low Temperatur Physics **100** (1995)

[67] C. Enss (editor), *Cryogenic Particle Detection*, Springer Berlin Heidelberg (2005)

[68] J. J. Hauser, et al., *Superconductivity in Cu and Pt by Means of Superimposed Films with Lead*, Physical Review **136** (1964)

[69] N. R. Werthamer, *Theory of the Superconducting Transition Temperature and Energy Gap Function of Supperposed Metal Films*, Physical Review **132** (1963)

[70] U. Nagel, et al., *Use of Proximity Effect in Iridium-Gold Superconducting Phase Transitioin Thermometers*, Journal of Low Temperatur Physics **93** (1993)

[71] U. Nagel, et al., *Proximity effect in iridium-gold bilayers*, Journal of Applied Physics **76** (1994)

[72] D. U. Gubser, et al., *Thermodynamic Properties of Superconducting Iridium*, Journal of Low Temperatur Physics **13** (1973)

[73] S. Roth, et al., *Cryogenic composite detectors for the dark matter experiments CRESST and EURECA*, Optical Materials **31**, 1415 (2009)

[74] M. v. Sivers, *Scintillating $CaWO_4$ Crystals for the Direct Dark Matter Search Experiments CRESST and EURECA*, Ph.D. thesis, Technische Universität München (2014)

[75] N. Spooner, et al., *Investigation of voltage amplification of thermal spectra ("Luke effect") in a low temperature calorimetric detector*, Physics Letters B **278**, 382 (1992)

[76] M. Stark, et al., *Application of the Neganov-Luke effect to low-threshold light detectors*, Nuclear Instruments and Methods in Physics Research A **545**, 738 (2005)

[77] M. Stark, *Detektoren mit effizienter und schneller Phononensammlung für das CRESST-Experiment*, Ph.D. thesis, Technische Universität München (2005)

[78] R. C. Alig, *Scattering by ionization and phonon emission in semiconductors. II. Monte Carlo calculations*, Physical Review B **27**, 968 (1983)

[79] V. S. Vavilov, *On Photo-Ionization by Fast Electrons in Germanium and Silicon*, Journal of Physics and Chemistry of Solids **8**, 223 (1959)

[80] M. Kiefer, *Improving the Light Channel of the CRESST-II-Dark Matter Detectors*, Ph.D. thesis, Technische Universität München (2012)

[81] R. Strauß, *Energy-Dependent Quenching Factor Measurements of CaWO4 Crystals at mK Temperatures and Detector Prototypes for Direct Dark Matter Search with CRESST*, Ph.D. thesis, Technische Universität München (2013)

[82] J. M. Schmaler, *The CRESST Dark Matter Search – New Analysis Methods and Recent Results*, Ph.D. thesis, Technische Universität München (2010)

[83] M. v. Sivers, *Optimizing Detectors for Dark Matter Search*, Diploma thesis, Technische Universität München (2010)

[84] C. Arnaboldi, et al., *Results from a search for the $0\nu\beta\beta$-decay of 130Te*, Physical Review C **78** (2008)

[85] N. Casali, et al., *Monte Carlo simulation of the Cherenkov radiation emitted by TeO2 crystal when crossed by cosmic muons*, Nuclear Instruments and Methods in Physics Research A **732**, 338 (2013)

[86] J. Beeman, et al., *Discrimination of α and β/γ interactions in a TeO2 bolometer*, Astroparticle Physics **35**, 558 (2012)

[87] W. R. Leo, *Techniques for nuclear and particle physics experiments: a how-to approach*, Springer (1987)

[88] D. R. Lide (editor), *CRC Handbook of Chemistry and Physics*, CRC Press, 84th edition (2003)

[89] J. Liebertz, *Einkristallzüchtung von Paratellurit (TeO_2)*, Kristall und Technik **4**, 221 (1969)

[90] I. Dafinei, et al., *TeO2 scintillating crystals growth and properties*, in *SCINT2005 Proceedings of the 8th International Conference on Inorganic Scintillators and their use in Scientific and Industrial Applications*, Alushta, Crimea, Ukraine, 19–23 September 2005, pp. 106–108 (2005)

[91] F. Bellini, et al., *Measurements and optimization of the light yield of a TeO2 crystal* (2014), `arXiv:1406.0713v2`

[92] N. Uchida, *Optical Properties of Single-Crystal Paratellurite (TeO2)*, Physical Review B **4**, 3736 (1971)

[93] K. Takizawa, et al., *REFRACTIVE INDICES OF PARATELLURITE AND LITHIUM IODATE IN THE VISIBLE AND ULTRAVIOLET REGIONS*, OPTICSCOMMUNICATIONS **23**, 279 (1977)

[94] J. Seidl, *Investigation of the Reflectivity of Reflective and Scintillating Foils for Future CRESST/EURECA Low-Temperature Detector Modules*, Master thesis, Technische Universität München (2014)

[95] M. Janecek, *Reflectivity Spectra for Commonly Used Reflectors*, IEEE TRANSACTIONS ON NUCLEAR SCIENCE **49**, 490 (2012)

[96] P. Huff, *The Detector Parameters Determining the Sensitivity of the CRESST-II Experiment*, Ph.D. thesis, Technische Universität München (2010)

[97] A. Langenkämper, *In preparation*, Master thesis, Technische Universität München (2015)

[98] M. Green, *Self-consistent optical parameters of intrinsic silicon at 300 K including temperature coefficients*, Solar Energy Materials & Solar Cells **92**, 1305 (2008)

[99] D. Aspnes, et al., *Dielectric functions and optical parameters of Si, Ge, GaP, GaAs, GaSb, InP, InAs, and InSb from 1.5 to 6.0 eV*, Physical Review B **27**, 27 (1983)

[100] A. Tanzke, *Optimization of Light Detectors for the CRESST Experiment*, Diploma thesis, Technische Universität München (2011)

[101] M. J. Berger, et al., *ESTAR, PSTAR, and ASTAR: Computer Programs for Calculating Stopping-Power and Range Tables for Electrons, Protons, and Helium Ions*, National Institute of Standards and Technology, Gaithersburg, MD, URL `http://physics.nist.gov/Star` (2005)

[102] S. Agostinelli, et al., *Geant4 - a simulation toolkit*, Nuclear Instruments and Methods in Physics Research Section A **506**, 250 (2003)

[103] R. Möllenberg, *Monte Carlo Study of Solar ^8B Neutrinos and the Diffuse Supernova Neutrino Background in LENA*, Ph.D. thesis, Technische Universität München (2013)

[104] O. Ponkratenko, et al., *The event generator DECAY4 for simulation of double beta processes and decay of radioactive nuclei* (2001), `arXiv:0104018v1`

[105] E. Andreotti, et al., ^{130}Te *neutrinoless double-beta decay with CUORICINO*, Astroparticle Physics **34**, 822 (2011)

[106] C. Absmaier, *Untersuchungen zur reproduzierbaren Herstellung von Iridium-Gold-Schichten zur Verwendung als supraleitende Phasenübergangsthermometer*, Diploma thesis, Technische Universität München (1995)

[107] J. Höhne, *Strahlungsnachweis mit supraleitenden Iridium/Gold-Phasenübergangsthermometern*, Ph.D. thesis, Technische Universität München (1998)

[108] W. Westphal, *Development and Characterization of Cryogenic Detectors for the CRESST Experiment*, Ph.D. thesis, Technische Universität München (2008)

[109] G. Franz, *Low Pressure Plasmas and Microstructuring Technology*, Springer Berlin Heidelberg (2009)

[110] R. Burkhardt, *Abschätzung der Abschrimwirkung des Garchinger Untergrundlabors (UGL) durch die Messung des Myonen-Flusses inner- und ausserhalb des UGLs*, Bachlor thesis, Technische Universität München (2012)

[111] T. Lachenmaier, *Messungen mit untergrundarmen Tieftemperaturdetektoren zum hocheffizienten Nachweis des* ^{71}*Ge-Zerfalls*, Ph.D. thesis, Technische Universität München (2005)

[112] J.-C. Lanfranchi, *Development of a New Composite Cryogenic Detection Concept for a Radiochemical Solar Neutrino Experiment*, Ph.D. thesis, Technische Universität München (2005)

[113] O. Lounasmaa, *Experimental Principles and Methods below 1K*, Academic Press (1974)

[114] F. Pobell, *Matter and Methods at Low Temperatures*, Springer, 3rd edition (2007)

[115] C. Enss, et al., *Low-Temperature Physics*, Springer Berlin Heidelberg (2005)

[116] J. Clarke, et al. (editors), *The SQUID Handbook*, volume 1, WILEY-VCH (2004)

[117] Jena Superconductive Electronics Foundry, *Bedienungsanleitung SQUIDControl L1*

[118] C. Ciemniak, *Setup of a Neutron Scattering Facility for the Measurement of Scintillation Light Quenching Factors of Low-Temperature Detectors Used in the Direct Dark Matter Search Experiments CRESST and EURECA*, Ph.D. thesis, Technische Universität München (2011)

[119] A. Gütlein, *Feasibility Study for a First Observation of Coherent Neutrino Nucleus Scattering Using Low-Temperature Detectors.*, Ph.D. thesis, Technische Universität München (2013)

[120] D. Hellgartner, *In preparation*, Ph.D. thesis, Technische Universität München (2015)

[121] J. Su, et al., *Alpha decay half-life of ^{147}Sm in metal samarium and Sm_2O_3*, The European Physical Journal A **46**, 69 (2010)

[122] J. F. Ziegler, et al., *SRIM-2013 - The Stopping and Range of Ions in Matter*, `http://www.srim.org/SRIM/SRIMLEGL.htm`

[123] G. Angloher, et al., *Limits on WIMP dark matter using scintillating $CaWO_4$ cryogenic detectors with active background suppression*, Astroparticle Physics **23**, 325 (2005)

[124] G. Angloher, et al., *Commissioning run of the CRESST-II dark matter search*, Astroparticle Physics **31**, 270 (2009)

[125] P. Bauer, *In preparation*, Master thesis, Technische Universität München (2015)

[126] Dr. S. Roth, *Private communication* (2014)

[127] S. Wawoczny, *In preparation*, Ph.D. thesis, Technische Universität München (2015)

[128] R. Jacoby, *In preparation*, Master thesis, Technische Universität München (2014)

[129] F. A. Danevich, et al., *Optimization of light collection from crystal scintillators for cryogenic experiments*, Nuclear Instruments and Methods in Physics Research A **744**, 41 (2014)

[130] R. B. Firestone, *Table of Isotopes*, John Wiley & Sons, INC., 8th edition (1996)

[131] C. Cozzini, et al., *Detection of the natural α decay of tungsten*, Physical Review C **70**, 064606 (2004)

[132] F. Alessandria, et al., *Sensitivity and Discovery Potential of CUORE to Neutrinoless Double-Beta Decay* (2011), `arxiv:1109.0494v3`

[133] Prof. Dr. F. v. Feilitzsch, *Private communication* (2014)

Danksagung

Ich möchte mich an dieser Stelle bei all jenen bedanken die mich in den Jahren meiner Doktorarbeit begleitet haben. Im Besonderen möchte ich mich bei meinem Doktorvater, Prof. Dr. Lothar Oberauer, für die Betreuung meiner Arbeit und die vielen interessanten Diskussionen bedanken.

Prof. Dr. Stefan Schönert möchte ich für das angenehme Arbeitsumfeld am Institut und für sein stetes Interesse an meiner Arbeit danken.

Dr. Jean-Côme Lanfranchi möchte ich dafür danken, dass er mir die Möglichkeit gegeben hat meine Doktorarbeit in seiner Nachwuchsgruppe am Exzellenz Cluster Universe anzufertigen und für seine ständige Unterstützung in allen Belangen meiner Arbeit.

Bei Dr. Walter Potzel und Dr. Sabine Roth möchte ich mich für die vielen Diskussionen rund um das Thema Neganov-Luke und Lichtdetektoren sowie für ihren Einsatz beim Korrekturlesen meiner Arbeit bedanken. Des Weiteren möchte ich mich auch bei allen anderen Korrekturlesern für das Lesen meiner Arbeit und die zahlreichen Anregungen bedanken.

I would like to thank Prof. Dr. Andrea Giulliani for supplying the TeO_2 crystal and the interesting discussions about our common project.

Dominik Hellgartner und Dr. Achim Gütlein danke ich für ihre Hilfe bei allen Themen die mit ROOT, C++, und Datenauswertung zu tun haben.

Beim Team der E15 Werkstatt möchte ich mich für das Herstellen meiner Detektorhalter und Spezialanfertigungen für den Kroystaten bedanken und bei Harald Hess im Speziellen für seine Hilfe beim Lösen diverser technischer Probleme am Kryostaten. Dem Team des Kristalllabors danke ich für die Unterstützung beim Tempern sowohl der Siliziumsubstrate als auch meiner Detektorhalter. Herrn Dipl.-Ing. Hermann Hagn danke ich besonders für seine Hilfe

beim Entstören meines Aufbaus und seine unschätzbar wertvollen Ratschläge zum Thema Messelektronik. Außerdem danke ich allen Sekretärinnen dafür, dass sie das Leben an unserem Institut bereichert und mir in allen bürokratischen Angelegenheiten sehr geholfen haben.

Andreas Bauer danke ich für die spontane Samarium-Spende aus seinem Fundus an seltenen Erden.

Dr. Karoline Schäffner danke ich für die Diskussionen rund um die Detektion von Cherenkov Licht aus TeO_2 Kristallen und ihre Unterstützung bei meinen CRESST Schichten am Gran Sasso.

Außerdem möchte ich mich bei allen Mitgliedern der E15 Kryogruppe sowie auch allen andern Post-Docs, Doktoranden, Bachelor- und Masterstudenten am Institut für das angenehme Arbeitsklima bedanken.

Zu guter Letzt möchte ich mich noch bei meiner Familie bedanken für ihr stetes Interesse an meiner Doktorarbeit und ihre Unterstützung auf dem langen Weg bis zum Abschluss der Arbeit.